CHARTING THE STATE SPACE OF PLANE COUETTE FLOW: EQUILIBRIA, RELATIVE EQUILIBRIA, AND HETEROCLINIC CONNECTIONS

A Thesis
Presented to
The Academic Faculty

by

Jonathan J Halcrow

In Partial Fulfillment
of the Requirements for the Degree
Doctor of Philosophy in the
School of Physics

Georgia Institute of Technology
ver. 1.4, October 24 2008

TABLE OF CONTENTS

SUMMARY

The study of turbulence has been dominated historically by a "bottom-up" approach, with a much stronger emphasis on the physical structure of flows than on that of the dynamical state space. Turbulence has traditionally been described in terms of various visually recognizable physical features, such as waves and vortices. Thanks to recent theoretical as well as experimental advancements, it is now possible to take a more "top-down" approach to turbulence. Recent work has uncovered non-trivial equilibria as well as relative periodic orbits in several turbulent systems. Furthermore, it is now possible to verify theoretical results at a high degree of precision, thanks to an experimental technique known as Particle Image Velocimetry. These results squarely frame moderate Reynolds number (Re) turbulence in boundary shear flows as a tractable dynamical systems problem.

In this thesis, I intend to elucidate the finer structure of the state space of moderate Re wall-bounded turbulent flows in hope of providing a more accurate and precise description of this complex phenomenon. Determination of previously unknown equilibria, relative equilibria, and their heteroclinic connections discovered in course of this exploration provides a skeleton upon which a numerically accurate description of turbulence can be framed. The behavior of the equilibria under variation of Reynolds number and cell aspect ratios is also examined. It is hoped that this description of the state space will provide new avenues for research into nonlinear control systems for shear flows as well as quantitative predictions of transport properties of moderate Re fluid flows.

CHAPTER I

INTRODUCTION

> The ultimate goal, however, must be a rational theory of statistical hydrodynamics where [···] properties of turbulent flow can be mathematically deduced from the fundamental equations of hydromechanics.
> E. Hopf

Understanding the nature of turbulence is one of the last great problems of classical mechanics. In a 1932 address to the British Association for the Advancement of Science, Horace Lamb said:

> I am an old man now, and when I die and go to heaven there are two matters on which I hope for enlightenment. One is quantum electrodynamics, and the other is the turbulent motion of fluids. And about the former I am rather optimistic.

Early attempts at describing turbulence focused on a statistical description. Turbulence was viewed as random fluctuations around a mean flow. One of the major successes of this approach is the Kolmogorov scaling law, which gives the probability distribution of the length scale of structures seen in isotropic turbulence. Another major result is the "law of the wall" (discussed in sect. 2.4.2). It describes the mean behavior of turbulent shear flows in terms of distance from the wall as measured in 'wall units.'

While this approach has been somewhat successful in describing the mean behavior of turbulent flows, it lacks descriptive power for the dynamical behavior of turbulent flows.

1.1 Poincaré, Turbulence, and Hopf's Last Hope

There is another vision of turbulence: the dynamical systems perspective. This is rooted in the work of Poincaré, Hopf, Smale, Ruelle, Gutzwiller, and others. The story begins with Poincaré. One of the great problems of his day was the three-body problem – understanding the motion of three bodies under their mutual gravitational attraction. Kepler had long since solved the problem for two bodies. In 1885, King Oscar of Sweden announced a prize to be awarded to whomever could obtain an analytic solution to the problem [?]. Poincaré was not able to produce such a solution – instead, he showed that no such solution could be obtained. His 1889 analysis not only won the prize, but also set the foundations of the geometric approach to dynamical systems whose methods lie at the core of this work.

The vision for this research comes from E. Hopf [?], who set forth the perspective of Navier-Stokes as an infinite dimensional state space, with each point corresponding to a complete $3D$ velocity field. He conjectured that inside this infinite dimensional state space there was a finite dimensional manifold, whose properties depended on the viscosity of the fluid. For extremely large viscosities, it corresponds to a single point: the laminar state. But, as viscosity is decreased (Re is increased), the stability of this manifold changes and its dimension jumps at certain critical values, bifurcating into new manifolds. His vision

of state space is one of a jungle of recurrent manifolds. These manifolds, known today as 'inertial manifolds,' are well-studied in the mathematics of spatio-temporal PDEs. Their finite dimensionality for non-vanishing viscosity parameters has been rigorously established in certain settings by Foiaš [**?**] and collaborators.

Hopf's ideas were somewhat ahead of his time. The idea of simulating the full Navier-Stokes equations on a computer at the time was so far out of the realm of possibility as to be laughable. In [**?**], Hopf laments:

> "[t]he great mathematical difficulties of these important problems are well known and at present the way to a successful attack on them seems hopelessly barred. There is no doubt, however, that many characteristic features of the hydrodynamical phase flow occur in a much larger class of similar problems governed by non-linear space-time systems. In order to gain insight into the nature of hydrodynamical phase flows we are, at present, forced to find and to treat simplified examples within that class."

As his simplified example, Hopf considered a modification of Burgers equation. The first numerical, geometric state space analysis of a simplified model of turbulence came with Lorenz's 3 mode truncation [**?**] of the Navier-Stokes equations for Rayleigh-Bénard convection state space. This idea has since been brought closer to true hydrodynamics with the Cornell group's POD models of boundary-layer turbulence [**?**, **?**].

Hopf also notes

> ... the geometrical picture of the phase flow is, however, not the most important problem of the theory of turbulence. Of greater importance is the determination of the probability distributions associated with the phase flow.

Hopf's call for understanding of probability distributions under phase flow has indeed proven to be a key challenge, the one in which dynamical systems theory has made the greatest progress in the last half century, namely, the Sinai-Ruelle-Bowen ergodic theory of "natural" or SRB measures for far-from-equilibrium systems [**?**, **?**, **?**, **?**]. The use of cycle expansions [**?**], introduced in 1988, has proved to be an effective tools for computing long time averages of quantities measured in chaotic dynamics.

The idea that chaotic dynamics is built upon unstable periodic orbits first arose in Ruelle's work on hyperbolic systems, with ergodic averages associated with natural invariant measures expressed as weighted summations of the corresponding averages about the infinite set of unstable periodic orbits.

In 1996 Christiansen *et al.* [**?**] proposed that the periodic orbit theory be applied to infinite-dimensional flows, such as the Navier-Stokes, using the Kuramoto-Sivashinsky model [**?**, **?**] as a laboratory for exploring the dynamics close to the onset of spatiotemporal chaos. This has proved to be a fruitful model for studying turbulence, in the vein of Hopf's vision [**?**, **?**, **?**].

In the spirit of Hopf, this thesis is a demonstration that the high-dimensional dynamics of this flow could be reduced to a low dimensional series of maps $s \to f(s)$. In this case, the unstable manifold of the shortest periodic orbit acted as the inertial manifolds of Hopf turbulent state space. For the first time for any nonlinear PDE, some 1,000 unstable periodic orbits were determined numerically.

Moore's Law, combined with recent theoretical and experimental advances has now cleared the way for an attack on the full Navier-Stokes equations. The details of these advances are discussed in sect. 2.5.

1.2   The Future

The long term goal of this research is to develop a dynamical systems description of turbulence based on exact unstable invariant solutions of the Navier-Stokes equations. Given this description, one could build better control systems or obtain accurate values of their transport properties[**?**]: This thesis focuses on wall-bounded shear flows at moderate Reynolds number. The 'unstable invariant solutions' computed are equilibria, relative equilibria, and heteroclinic connections between them. These are exact solutions. Equilibria are states in which the flow itself is constant in time, while relative equilibria are states which remain invariant up to translation. An heteroclinic connection is a particular course that the system takes starting at one equilibrium and ending at another.

Our goal here is to elucidate the state space topology and the symbolic dynamics of low-dimensional attractors/repellers embedded in the high-dimensional state spaces of turbulent wall-bounded Navier-Stokes flows.

As more of these states are obtained, the skeleton of observed turbulent dynamics is filled out from the stable and unstable manifolds of these invariant solutions. The hope is that this will lead to predictive models of the long-time dynamics, based on how the turbulent attractor visits the neighborhoods of these different states, jumping from state to state. And, using periodic orbit expansions, the long time behavior of physically interesting quantities such as bulk flow rates and the mean wall drag can be estimated.

1.3   What is New in This Thesis

A key new tool, developed in ref. [**?**], is a method of visualizing the state-space dynamics of the Navier-Stokes equations. For moderate-Re flows, our projections from 10^4-10^5 dimensional state spaces to dynamically intrinsic 2- or 3-dimensional coordinate frames offer an informative view of state-space dynamics, complementary to visualizations of velocity and vorticity as time-varying fields in $3D$ physical space

This approach has enabled the discovery of several new equilibria and relative equilibria. As demonstrated in chapter 5 and chapter 6, these new states play important roles in the long term behavior of plane Couette flow. Particularly surprising was the discovery of several heteroclinic connections, connecting these states together into a web. Schmiegel's excellent PhD thesis [**?**] covers some of the same ground, however the comparison is difficult since that work was done at significantly lower resolution, and for cell sizes different from those studied here.

CHAPTER II

NAVIER-STOKES EQUATIONS AND PLANE COUETTE FLOW

2.1 In the Beginning...

To discuss the equations of motion which govern a fluid, we must first begin at the beginning, Newton's second law [**?**] –

> Lex II: Mutationem motus proportionalem esse vi motrici impressae, et fieri secundum lineam rectam qua vis illa imprimitur.

Or, in more modern language

$$\frac{\partial p}{\partial t} = F \,. \tag{1}$$

To apply this to a fluid, consider the point of view of a small parcel of fluid. If the momentum density is given by $\mathbf{p}(\mathbf{x}, t)$, then the change over a period δt is

$$\delta \mathbf{p} = \mathbf{p}(\mathbf{x} + \mathbf{v}\delta t, t + \delta t) - \mathbf{p}(\mathbf{x}, t) \tag{2}$$

Expanding this to first order in δt gives:

$$\delta \mathbf{p} = v_x \delta t \frac{\partial \mathbf{p}}{\partial x} + v_y \delta t \frac{\partial \mathbf{p}}{\partial y} + v_z \delta t \frac{\partial \mathbf{p}}{\partial z} + \delta t \frac{\partial \mathbf{p}}{\partial t} \,. \tag{3}$$

So the rate of change in momentum density from the reference frame moving with the fluid is

$$\frac{D\mathbf{p}}{Dt} = \frac{\partial \mathbf{p}}{\partial t} + (\mathbf{v} \cdot \nabla) \, \mathbf{p} \,. \tag{4}$$

If the fluid has density $\rho(\mathbf{x}, t)$, then the momentum density is $\mathbf{p} = \rho \mathbf{v}$, and:

$$\mathbf{v}\partial_t \rho + \rho \partial_t \mathbf{v} + (\mathbf{v} \cdot \nabla) \, (\rho \mathbf{v}) = \mathbf{f} \,, \tag{5}$$

where $\mathbf{f}(\mathbf{x}, t)$ is the force density.

Barring nuclear reactions, we also have mass conservation. Suppose that a fluid with density $\rho(\mathbf{x}, t)$ is contained in a volume V, bounded by surface S. Any increase or decrease in mass inside this volume must by due to flux through the boundaries, due to mass conservation so:

$$\partial_t \int_V \rho dV + \oint_S \rho \mathbf{v} \cdot d\mathbf{S} = 0 \,. \tag{6}$$

Applying Gauss' law to this gives that

$$\int_V \partial_t \rho + \nabla \cdot (\rho \mathbf{v}) = 0 \,. \tag{7}$$

Since this is true for any arbitrary volume V, the integrand itself must be 0. That is

$$\partial_t \rho + \nabla \cdot (\rho \mathbf{v}) = 0 \,. \tag{8}$$

We shall restrict our attention to incompressible fluids, which is to say that the density of the fluid is everywhere equal and constant. Restricting (8) to these conditions gives us that

$$\nabla \cdot \mathbf{v} = 0 \,. \tag{9}$$

Furthermore, attention is restricted to Newtonian fluids which have a restoring force density (skipping some steps) given by:

$$\mathbf{f} = -\nabla p + \mu \nabla^2 \mathbf{v} \,. \tag{10}$$

where μ is the viscosity, the resistance of the fluid to shear, and p is the pressure of the fluid.

Putting this together with (5):

$$\rho \left(\frac{\partial \mathbf{v}}{\partial t} + \mathbf{v} \cdot \nabla \mathbf{v} \right) = -\nabla p + \mu \nabla^2 \mathbf{v} \,. \tag{11}$$

2.2 Scale Invariance and the Reynolds number

Nondimensionalizing (11) yields a new differential equation with one dimensionless parameter, the Reynolds number Re. It is named for Osbourne Reynolds who noted the sudden breakdown of laminar flow in a pipe by way of a sinusoidal instability at a certain critical value of the eponymous number.

In Reynolds' words [**?**]:

> If the motion be supposed to depend on a single velocity parameter U, say the mean velocity along a tube, and on a single linear parameter c, say the radius of the tube [...] It seemed, however, to be certain if the eddies were owing to one particular cause, that integration would show the birth of eddies to depend on some definite value of

$$\frac{c\rho U}{\mu} \tag{12}$$

The Reynolds number is defined as $Re = UL/\nu$, where $\nu = \mu/\rho$ is the kinematic viscosity of the fluid, U is the typical velocity, and L is the length scale.

2.3 Plane Couette Flow

Plane Couette flow named in honor of M.M.A. Couette, is the flow of an incompressible viscous fluid confined between two infinite parallel plates moving in opposite directions at constant and equal velocities. In this thesis, no-slip boundary conditions are used. This means that the velocity of the fluid is constrained to match that of the walls at the interface, driving the motion of the fluid in the bulk. At low values of Re, the fluid is laminar – matching the velocity at the walls and changing linearly in between. The phenomenon we wish to describe are the turbulent (or "sinuous", in the words of Reynolds [**?**]) motions observed in boundary shear flows at moderate Reynolds numbers, see figure 3.

We refer to the direction that the walls are moving along as the streamwise, or x direction, the direction perpendicular to the walls as the wall-normal, or y direction, and the
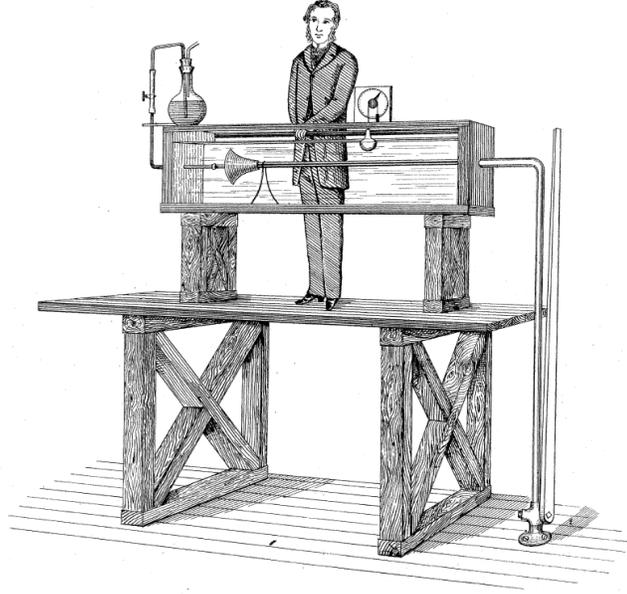
Figure 1: A sketch of Osbourne Reynolds' experiment [**?**].
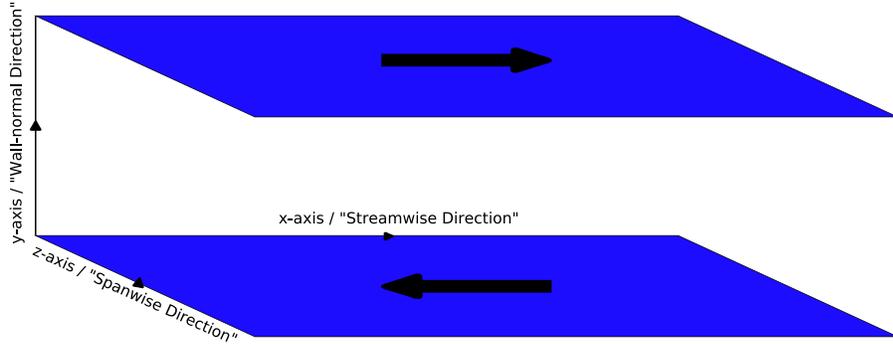
Figure 2: A schematic diagram of Plane Couette flow.

direction perpendicular to these two as the spanwise, or z direction. The corresponding components of the fluid's velocity are $\mathbf{u}(\mathbf{x}) = [u, v, w](x, y, z)$. The walls are located at $y = \pm L$ and move with velocity $\pm U$, and the fluid has viscosity ν. Nondimensionalizing the Navier-Stokes equations, so that the velocity is normalized by U, the lengths are normalized by L, and the time is normalized by L/U, we get that the Reynolds number is $Re = UL/\nu$.

Then, we write the velocity of the fluid in terms of its deviation from laminar flow, $\mathbf{u} = y\,\hat{\mathbf{x}}$. With $\mathbf{u}$ replaced by $\mathbf{u} + y\,\hat{\mathbf{x}}$ the Navier-Stokes equations takes form:

$$\frac{\partial \mathbf{u}}{\partial t} + y\frac{\partial \mathbf{u}}{\partial x} + v\,\hat{\mathbf{x}} + \mathbf{u} \cdot \nabla \mathbf{u} = -\nabla \mathbf{p} + \frac{\mathbf{1}}{Re}\nabla^{\mathbf{2}}\mathbf{u}, \quad \nabla \cdot \mathbf{u} = \mathbf{0}. \tag{13}$$

The deviation of the velocity from laminar flow satisfies Dirichlet conditions at the walls, $\mathbf{u}(x, \pm 1, z) = 0$. Henceforth, we refer to the difference $\mathbf{u}$ as 'velocity' and $\mathbf{u} + y\,\hat{\mathbf{x}}$ as 'total velocity.'

The spatial mean of the pressure gradient is set to zero, i.e., there is no pressure drop

across the cell in x or z directions. Alternatively the bulk flow rate could be set to zero. The choice of this is a subtle issue and different authors use slightly different conventions; for instance, Kawahara [**?**] sets the streamwise bulk flow rate and the spanwise pressure gradient to zero. However, it does not significantly impact the qualitative nature of the results.

In computations, the infinite x and z extent is replaced with a periodic cell of lengths L_x and L_z. We denote the periodic domain of the cell by $\Omega = [0, L_x] \times [-1, 1] \times [0, L_z]$, and refer to it in the text either by

$$
\begin{aligned}
\text{cell size:} \quad & \Omega = [L_x, 2, L_z], \quad \text{or} \\
\text{cell wave numbers:} \quad & (\alpha, \gamma) = (2\pi/L_x, 2\pi/L_z).
\end{aligned}
\tag{14}
$$

L_x and L_z are not parameters; rather, they select from the continuous spectrum of solutions admissible for the infinite aspect ratio $[L_x, 2, L_z] = [\infty, 2, \infty]$ plane Couette flow the discrete subset whose streamwise, spanwise wavelengths or their multiples equal L_x, L_z, respectively. A given cell thus admits spatially periodic velocity fields with wavenumbers $(\alpha, \gamma) = (2\pi m/L_x, 2\pi n/L_z)$, where m, n are integers.

Empirically, Kim, Kline and Reynolds [**?**] observed that streamwise instabilities lead to dynamically determined, pairwise counter-rotating rolls whose diameter is approximately 100 wall units (see sect. 2.4.2). Such rolls fit approximately into the wall-wall separation $L_y = 2$ when Re is in the range of $300 - 500$. The rolls, in turn, exhibit downstream varicose instabilities of roughly twice the roll diameter. These unstable coherent structures are very prominent in numerical and experimental observations (see figure 3 and the animations on Gibson's website [**?**]), and motivate our investigation of how the known exact coherent structures behave with changes in Re and wavelength projection $[L_x, 2, L_z]$. In what follows, most of our calculations are carried out in one of the two small-aspect cells:

$$
\begin{aligned}
\Omega_{\text{W03}} &= [2\pi/1.14, 2, 4\pi/5] & &\approx [5.51, 2, 2.51] \\
\Omega_{\text{HKW}} &= [2\pi/1.14, 2, 2\pi/1.67] & &\approx [5.51, 2, 3.76] \\
\Omega_{\text{Sch}} &= [2\pi, 2, 4\pi] & &\approx [6.28, 2, 12.57].
\end{aligned}
\tag{15}
$$

The Hamilton *et al.* [**?**] Ω_{HKW} cell is empirically the smallest aspect ratio cell exhibiting sustained turbulence, while the Waleffe [**?**] Ω_{W03} cell appears to exhibit only transient turbulence. Schmiegel [**?**] study of equilibria was carried out for the Ω_{Sch} cell not studied here.

Although the cell aspect ratios studied here are small, the $3D$ states explored by equilibria and their unstable manifolds explored here are strikingly reminiscent of typical states in larger aspect cells, such as figure 3. It should be kept in mind that for small aspect ratios the dynamics is very sensitive to the precise choice of $[L_x, 2, L_z]$, and the dynamics within the Ω_{HKW} cell differs significantly from the Ω_{W03} cell dynamics.

2.3.1 Energy

For nondimensionalized plane Couette flow, the kinetic energy, in terms of the total velocity $\mathbf{u}$ (as opposed to the deviation from laminar flow $\mathbf{u} + y\hat{\mathbf{x}}$) is given by:

$$
E(t) = \frac{1}{2} \int_V (\mathbf{u} \cdot \mathbf{u}) \, dx \, dy \, dz \qquad V = 2L_x L_z.
\tag{16}
$$

Since energy is being dissipated through viscosity and input through the walls, this is not a conserved quantity. Indeed, we can compute its rate of change and break it up into two parts: the rate of input from the walls and the rate of loss through viscosity.

$$\frac{dE}{dt} = \int_V (\partial_t \mathbf{u} \cdot \mathbf{u}) d^3 V = -\int_V \mathbf{u} \cdot (\mathbf{u} \cdot \nabla)\mathbf{u} + \nu \mathbf{u} \cdot \nabla^2 \mathbf{u} - \mathbf{u} \cdot \nabla p \, d^3 V \qquad (17)$$

This can be decomposed into rate of energy lost to do viscous dissipation, D, and rate of energy input from the walls I, such that $\frac{dE}{dt} = I - D$. Rewriting the velocity as the deviation from laminar flow, $\mathbf{u} + y\hat{\mathbf{x}}$, and skipping some steps we get:

$$D(t) = \frac{1}{V} \int_\Omega d\mathbf{x} \, |\nabla \times (\mathbf{u} + \mathbf{y}\,\hat{\mathbf{x}})|^{\mathbf{2}} \qquad (18)$$

$$I(t) = 1 + \frac{1}{2A} \int_A dx \, dz \, \left(\frac{\partial u}{\partial y}\Big|_{y=1} + \frac{\partial u}{\partial y}\Big|_{y=-1} \right), \qquad (19)$$

where $V = 2L_x L_z$ and $A = L_x L_z$. The normalizations are chosen so that $D = I = 1$ for laminar flow and $\dot{E} = I - D$.

2.3.2 On 2D Disturbances

Squire's Theorem [?] states that $2D$ disturbances of the laminar flow are always more unstable than $3D$ ones. Indeed, if we force the Navier-Stokes equations to be streamwise independent (i.e. set $\partial_x = 0$) there can be no equilibria other than the laminar state, which is absolutely stable in that case. The spanwise and wall-normal velocities act independently of the streamwise velocity [?]:

$$\partial_t v + v\partial_y v + w\partial_z v \;=\; -\partial_y p + \nu \nabla^2 v \qquad (20)$$
$$\partial_t w + v\partial_y w + w\partial_z w \;=\; -\partial_z p + \nu \nabla^2 w \qquad (21)$$
$$\partial_y v + \partial_z w \;=\; 0 \qquad (22)$$

The streamwise velocity is now governed by a linear equation, forced by v and w:

$$\partial_t u + v\partial_y u + w\partial_z u = \nu \nabla^2 u. \qquad (23)$$

Without the streamwise velocity, there is no energy input in the (v, w) system. So, the viscosity will eventually damp out any disturbances. More rigorously, the rate of change of the disturbance kinetic energy $E = \frac{1}{2}\int u_i'^2 dx$, is given by the Reynolds-Orr energy equation [?],

$$\frac{dE}{dt} = -\int u_j' u_i' D_{ij} + R^{-1}(\partial_j u_i')^2 dx, \qquad (24)$$

where D_{ij} is called the "rate of strain tensor" of the base flow

$$D_{ij} = \frac{1}{2}(\partial_j U_i + \partial_i U_j) \qquad (25)$$

In the case of streamwise independent flow, since (v, w) is decoupled from u, we can drop the streamwise parts. Since $V = W = 0$, $D_{ij} = 0$. Therefore the integrand in equation 24 is strictly non-negative. So we can rule out any time-periodic solutions. An equilibrium would have to satisfy $\partial_j u_i = 0$. Since we have no-slip boundary conditions, this clearly implies that the only 2D steady state is $v = w = 0$.

8
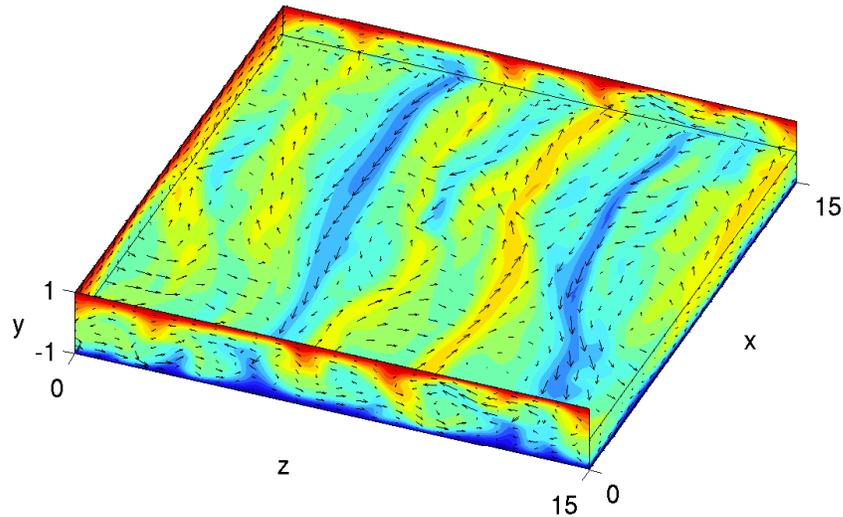
Figure 3: A snapshot of a typical turbulent state in a large aspect cell $[L_x, 2, L_z] = [15, 2, 15]$, $Re = 400$. The top wall moves towards the viewer, and the bottom wall moves away with equal and opposite velocity. The velocity field is coded by color and $2D$ vectors: Red - fluid moving streamwise, in the x direction; blue - fluid moving in the $-x$ direction. $[y, z]$ section vectors: fluid velocity $[0, v, w]$ transverse to the streamwise velocity u. The top half of the fluid is cut away to show the midplane velocity field $[u, 0, z]$ represented by $2D$ in-plane vectors, with streamwise velocity u also color-coded. See Gibson website [**?**] for movies of the time evolution of such states.

2.4 Turbulent plane Couette flow

Through the course of many experimental and numerical studies of wall-bounded shear flows a general picture of how turbulence arises and what sort of structures it produces has emerged. It is hoped that this work will serve as a guide for partition of state space which captures the dynamics of plane Couette flow.

2.4.1 Reynolds Decomposition

Turbulence is a phenomenon which does not have a simple definition. However, one typical way of looking at it is by decomposing into a mean flow and irregular fluctuations on top of that mean flow. This is the approach used by Reynolds [**?**]. If we write the velocity, $\tilde{u}_i$, in terms of its mean, U_i and fluctuations on top of the mean, u_i:

$$\tilde{u}_i(x_i, t) = U_i(x_i) + u_i(x_i, t) \tag{26}$$

$$\tilde{p}_i(x_i, t) = P_i(x_i) + p_i(x_i, t) \,. \tag{27}$$

Define the mean values explicitly by:

$$U_i(x_i) = \lim_{T \to \infty} \frac{1}{T} \int_0^T \tilde{u}_i(x_i, t) dt \,. \tag{28}$$

If the flow is incompressible, then the mean must be incompressible:

$$\langle \nabla \cdot \tilde{\mathbf{u}} \rangle = 0 \tag{29}$$

$$\nabla \cdot \mathbf{U} = 0 \tag{30}$$

Then, since the total and the mean are incompressible, the fluctuations clearly must be as well. Assuming that the time averages commutes with differentiation, the time-averaged Navier-Stokes equations, (11), is

$$\rho \partial_j (U_j U_i) + \rho \partial_j (\overline{u_j u_i}) = -\partial_i P + \mu \nabla^2 U_i \tag{31}$$

The time-averaged nonlinear interaction of the fluctuations, $\rho(\overline{u_j u_i})$, is referred to as the "Reynolds stress." Note that adding the incompressibility constraint to this does not produce a closed system. This is referred to as the *closure problem* [?]. In order to close the system, an assumption must be made about the Reynolds stress. These models of Reynolds stress can become quite complicated [?]. Rather than trying to model plane Couette flow in this way, the Navier-Stokes equations are integrated directly, as described in chapter 4. However, Reynolds stress still plays an important role in understanding the nature of turbulence in wall-bound shear flows as described in the next section.

2.4.2 Wall Units and The "Law of the Wall"

Turbulent wall-bounded flows have been observed to have a three layer structure, which can be categorized by the relative strengths of viscosity and Reynolds stress. In the innermost layer, viscosity dominates and the velocity profile changes linearly with the distance to the wall. In the outermost layer, Reynolds stress dominates and the fluid behaves inviscidly. The middle layer, referred to as the *buffer layer*, is a zone where the Reynolds and viscous stresses are roughly equal in magnitude. The scale of the Reynolds stress, $\overline{uv}$, defined to be u_*^2, where u_* is called the friction velocity. Customarily [?], it is defined numerically, by the slope of the velocity profile at the wall

$$u_* = \sqrt{\nu \frac{dU}{dy}|_\Gamma} \,. \tag{32}$$

A "wall unit" is defined by the scale of the size of the inner layer and is taken to be

$$l^+ = \frac{\nu}{u_*} \,. \tag{33}$$

This scale can also be used to define a new Reynolds number, called the frictional Reynolds number:

$$Re_* = \frac{u_* h}{\nu} = \frac{h}{l^+} \,. \tag{34}$$

Alternatively, this can be thought of as the height of the channel in wall units.

The length of a wall unit sets the scale for a host of dynamical structures in wall-bounded shear flows, beyond the Reynolds stress. The inner-most layer measures 5^+, while the buffer layer extends to $y^+ = 25 - 35$. In the outermost layer, the mean velocity is roughly given by

$$u^+ = \frac{1}{\kappa} \ln(y^+) + C \,, \tag{35}$$
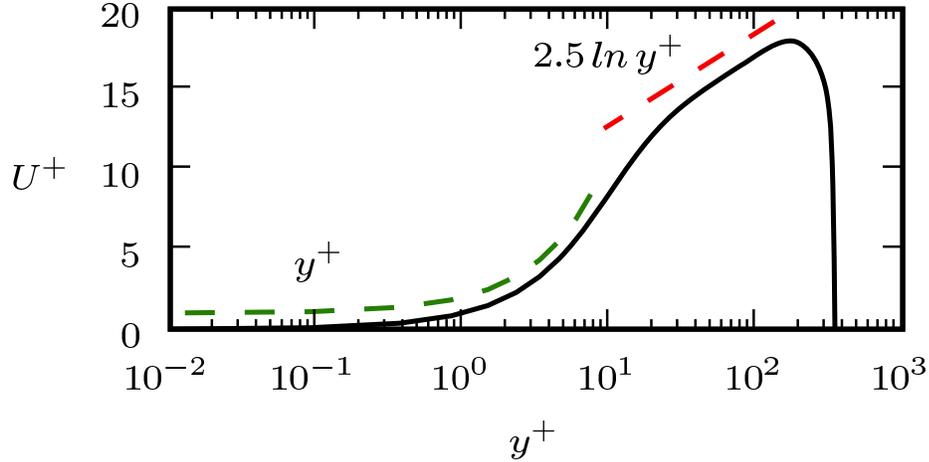
Figure 4: The Law of the Wall: The spatial averaged, streamwise velocity exhibits a characteristic scaling in terms of the distance from the wall, when measured in wall units.

where κ, also known as the Von Karman's constant, is approximately 0.41. This is referred to as the *law of the wall*. The mean velocity of a typical turbulent plane Couette state is plotted as a function from the distance from the wall in wall units in figure 4, demonstrating the law of the wall.

Following refs. [?, ?], in this thesis we mostly work at $Re = 400$, which, in wall units, amounts to a wall-to-wall distance of $\approx 100^+$.

2.5 A Brief History of Turbulent Shear Flows

The history of rigorous study of plane Couette flow and other wall bound shear flows goes back at least half a century. Kline *et al.* [?] studied pressure-driven boundary layer flow and observed streaks of high speed fluid with a characteristic spacing of $\lambda^+ = 100$, in wall units. These hypothesize an intermittency or "bursting"route to turbulence in boundary flows. This is described in three phases. To start, the flow is organized into "streaks." These are streamwise oriented structure of relatively high speed or low speed fluid. These streaks are lifted from the wall into the bulk of the flow, by a weak streamwise vorticity. As the streak is lifted and travels downstream, an inflection point in the streamwise profile is created. This inflection point creates an oscillatory instability. This instability grows quickly creating a more chaotic motion, referred to as "breakup" in ref. [?]. The "breakup" phase is primarily characterized by the growth of streamwise vortices, but also involves regrowth of the oscillatory motion as well as spanwise vortices to a less frequent degree. Smith and Metzler [?] experimentally established that the spanwise spacing of these streaks independent of Re.

There were several attempts to try to explain the origin of the streamwise vortices. The laminar state of plane Couette flow is linearly stable at all values of Re [?], so this ruled out bifurcations from laminar flow. One such attempt was 'direct resonance theory' [?] which involved growth of the vortices out of resonance in the eigenmodes of the laminar state. However, this approach was problematic in that it does not appear to be able to overcome viscous decay [?].

A ground breaking paper in the numerical study of channel flows, Kim, Moin and

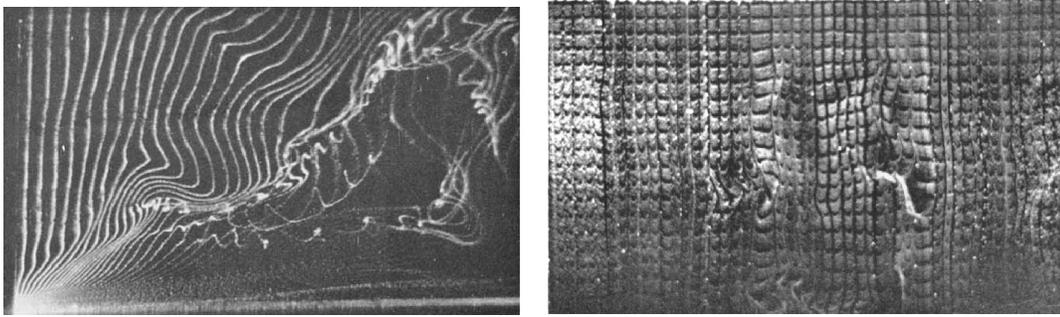**Figure 5:** Hydrogen bubble lines in a boundary layer flow: (Left) growth of a streamwise rolls with the flow moving left to right and the wall normal direction being vertical [?] (Right)the characteristic streak size streamwise motion is top to bottom and the spanwise direction is left to right [?]

Moser [?] performed full direct numerical simulations of wall bounded shear flows. This opened the door for other numerical studies, such as refs. [?, ?]. Jiminez and Moin [?], studied plane Poiseuille flow, a pressure driven flow in a channel with fixed walls, to establish a minimal size cell for which turbulence is sustained. Hamilton, Kim, and Waleffe [?], took a similar approach to plane Couette flow at minimal Re. In this minimal cell, a quasi-cyclic, three phase process was observed: streamwise vortices produce streaks which then break down until reformation of the vortices. They put forth this process as key in understanding the source of the 100 wall unit streak spacing that is observed. As they shrank the cell in the spanwise direction, forcing the streaks closer together, turbulence was no longer sustained. So, it is hypothesized that the time scales of the processes involved in sustaining turbulence become mismatched at different spacings.

These numerical results informed a more mathematically precise model [?, ?], termed the Self-Sustaining Process (SSP). SSP explains the cyclic behavior in terms of a weakly nonlinear model, in which rolls create streaks. Waleffe [?, ?] further developed these ideas into a 'self-sustaining process theory' that explains the quasi-cyclic roll-streak behavior in terms of the forced response of streaks to rolls, growth of streak instabilities, and nonlinear feedback from streak instabilities to rolls.

There have been many attempts to try to model this apparent low dimensional behavior with a low dimensional dynamical system. One type of approach is 'Proper Orthogonal Decomposition' [?, ?]. This approach attempts to determine the important directions in state space experimentally, and then models turbulence as a truncated Gälerkin projection of the Navier-Stokes equations on to these modes. These models reproduce some qualitative features of the boundary layer, but the quantitative accuracy and the validity of simplifying assumptions in their derivation are uncertain (see refs. [?, ?, ?]). POD models for plane Couette were developed in ref. [?].

Another class of low-order models of plane Couette flow derives from the self-sustaining process discussed above (seerefs. [?, ?, ?, ?, ?]). These models use analytic basis functions explicitly designed to represent the streaks, rolls, and instabilities of the self-sustaining process, compared to the numerical basis functions of the POD, which represent statistical features of the flow. They improve on the POD models by capturing the linear stability of the laminar flow and saddle-node bifurcations of non-trivial 3D equilibria consisting of

rolls, streaks, and streak undulations. The work of ref. [?], based on a 9-variable model [?], offers an elegant dynamical systems picture, with the stable manifold of a periodic orbit defining the basin boundary that separates the turbulent and laminar attractors at $Re <$ 402 and the stable set of a higher-dimensional chaotic object defining the boundary at higher Re. However, these models share with POD models a sensitive dependence on modeling assumptions and uncertain quantitative relations to fully-resolved simulations. A systematic study of the convergence of POD/Galërkin models of plane Couette flow to fully-resolved simulations indicates that dimensions typical in the literature (10-10^2) are orders of magnitude too low for either short-term quantitative prediction or reproduction of long-term statistics [?].

The lack of quantitative success in low-dimensional modeling motivates yet another approach: the calculation of *exact invariant solutions* of the fully-resolved Navier-Stokes equations. The idea here is to bypass low-dimensional modeling and to treat fully-resolved CFD algorithms directly as very high-dimensional dynamical systems. Nagata [?] computed a 'lower-branch' and 'upper-branch' pair of nontrivial equilibrium solutions to plane Couette flow by continuation and bifurcation from a wavy vortex solution of Taylor-Couette flow. Starting with physical insights from the self-sustaining process, Waleffe [?, ?, ?] generated, *ab initio*, families of exact $3D$ equilibria and traveling waves of plane Couette and Poiseuille flows for a variety of boundary conditions and Re numbers, using a 10^4-dimensional Newton search and continuation from non-equilibrium states that approximately balanced the mechanisms highlighted by the self-sustained process. As noted by Waleffe [?], these solutions, and Clever-Busse [?]'s equilibria of plane Couette flow with Rayleigh-Bernard convection, are homotopic to the Nagata equilibria under smooth transformations in the flow conditions.

Refs. [?, ?] carried the idea of a self-sustaining process over to pipe flow and applied Waleffe's continuation strategy to derive families of traveling-wave solutions for pipes. Traveling waves for plane Couette flow were computed by Nagata [?] using a continuation method. Later, traveling waves for pressure-driven channel flow were obtained in ref. [?] with a shooting method. The first short-period unstable periodic solutions of Navier-Stokes were computed by Kawahara and Kida [?]. Recently, Viswanath [?] has computed *relative* periodic orbits (orbits which repeat themselves with a translation) and further periodic orbits of plane Couette flow that exhibit break-up and reformation of roll-streak structures.

The exact solutions described above turn out to be remarkably similar in appearance to coherent structures observed in DNS and experiment. Waleffe [?] coined the term 'exact coherent structures' to emphasize this connection. The upper-branch solution, for example, captures many statistical features of turbulent plane Couette flow and appears remarkably similar to the roll-streak structures observed in direct numerical simulations.

Waleffe [?] showed that the upper and lower branch equilibria appear at lowest Reynolds number with streak spacing of 100^+ wall units, an excellent match to that observed in ref. [?]. The periodic and relative orbits of refs. [?, ?] appear to be embedded in plane Couette flow's natural measure, and most of them capture basic statistics more closely than the equilibria.

The relevance of steady solutions to sustained turbulence and transition to turbulence is discussed in refs. [?, ?, ?]. The stable manifold of the lower-branch solution appears form an important portion of the basin boundary between the turbulent and laminar attractors (see refs. [?, ?, ?]). Kerswell's numerical simulations in [?] suggest that the unstable manifolds of lower-branch traveling waves act as similar boundaries in pipe flow, and that turbulent fields make occasional visits to the neighborhoods of traveling waves.

Another important dynamical structure is the heteroclinic connection, an orbit which originates infinitesimally close to one equilibrium, and terminates at another. Such orbits

were found in Taylor-Couette flow in ref. [**?**]. Kerswell [**?**] discusses their possible role in transition to turbulence. The Lorenz system [**?**] is also suggestive of the role of heteroclinic bifurcations in turbulence. Schmiegel [**?**] found many equilibria, and heteroclinic connections between them in plane Couette flow, however such solutions were too under-resolved to be reliable.

Together, these results form a new way of thinking about coherent structures and turbulence: (a) that coherent structures are the physical images of the flow's least unstable invariant solutions, (b) that turbulent dynamics consists of a series of transitions between these states, and (c) that intrinsic low-dimensionality in turbulence results from the low number of unstable modes for each state [**?**].

CHAPTER III

SYMMETRY AND PLANE COUETTE FLOW

Often times, a dynamical system may be symmetric in some sense. For example, the motion of a planet around the sun is rotationally symmetric. By taking care to understand the symmetry of a particular dynamical system, great simplifications are often possible which lead to a larger understanding of the system. In this context, 'symmetry' means any linear transformation, γ, of the state of a dynamical system which commutes with forward time evolution. That is to say if we transformed any state of the system, let the system run for any period of time, then undid the transformation, it would be as if we had never made the transformation at all. More compactly, we say that the dynamical system $\dot{a} = f(a)$ is symmetric with respect to γ if

$$\gamma \dot{a} = \gamma f(a) = f(\gamma a) \,.$$

3.1 Mathematical Background

3.1.1 Group Theory

Before we delve into a discussion of the impact of symmetry on the behavior of dynamical systems, we must first make a detour to discuss some elements of Group Theory.

It is natural to consider the set of symmetries of a dynamical system taken with the operation of composition as a mathematical group. To see this, first consider the formal definition of a group:

Definition 1. A group $(G, \diamond)$ consists of a set of elements, G, taken together with a binary operation, $\diamond : G \times G \to G$ with the following properties:

1. **Closure:** For any two elements $g, h \in G$, $g \diamond h \in G$.

2. **Associativity:** For any three elements $a, b, c \in G$, $a \diamond (b \diamond c) = (a \diamond b) \diamond c$.

3. **Identity:** There exists some $e \in G$ such that for all $g \in G$, $e \diamond g = g$.

4. **Inverse:** Every $g \in G$ has a corresponding inverse $g^{-1} \in G$ such that $g \diamond g^{-1} = g^{-1} \diamond g = e$.

If we extend the notion of a group to one containing an infinite number of elements, we can arrive at the notion of a *Lie group* – a group whose elements also have the structure of a differentiable manifold. A group which is a subset of another (but still satisfies the axioms of Def. 1) is called a *subgroup*.

Def. 1 defines the internal structure of a group but it says nothing about how it *acts* on a particular space. To any one group, we could ascribe a myriad of ways by which it may act on a particular space. What is required of a *group action* is that its definition must mesh with the group's structure. In particular,

Definition 2. [?] A *group action* of a group $(G, \diamond)$ on a set A is a map from $G \times A$ to A, written $g \cdot a$ for $g \in G$, $a \in A$, which satisfies the following two properties:

1. $g_1 \cdot (g_2 \cdot a) = (g_1 \diamond g_2) \cdot a$, $\forall g_1, g_2 \in G, a \in A$,

2. $e \cdot a = a$, $\forall a \in A$

A map $\phi : G \to H$, where G and H are groups which commutes with the group operation of G is called a homomorphism. More precisely:

Definition 3. [?] Let $(G, \star)$ and $(H, \diamond)$ be two groups. A *homomorphism* is map $\phi : G \to H$ such that

$$\phi(g_1 \star g_2) = \phi(g_1) \diamond \phi(g_2), \qquad \forall g_1, g_2 \in G \tag{36}$$

A homomorphism which is also a bijection is called an *isomorphism*. A *representation* homomorphism from a group G onto a set of concrete mathematical entitites[?].

3.1.2 Representation Theory

Symmetries of dynamical systems tend to be linear transformations of state space, so we are interested in the group $GL(V)$ – the group of linear transformations acting on a vector space V. A homomorphism, Γ, from a group G onto $GL(V)$ is known as a *linear representation*. The dimension of V will be called the dimension of the representation. From this point forward linear representation and representation will be used interchangeably and shortened to 'rep.'

We can always produce a new, equivalent representation from an old one by way of a similarity transformation. It can be shown that any representation by nonsingular matrices can be transformed to an equivalent representation by unitary matrices [?]. So, all representations from here on will also be assumed unitary.

Given two reps, it is possible to construct another larger rep, by combining them:

$$\Gamma^{(3)}(g) := \Gamma^{(1)}(g) \oplus \Gamma^{(2)}(g) = \begin{pmatrix} \Gamma^{(1)}(g) & 0 \\ 0 & \Gamma(2)(g) \end{pmatrix}. \tag{37}$$

Any rep which can be brought to such a block diagonal form by similarity transformation is called reducible. A rep which is not reducible is called an irreducible representation or irrep for short [?] .

3.1.3 Equivariance

We now can return to the notion of symmetry. The set of symmetries of a dynamical system (V, f), as defined above, is a subset of $GL(V)$. The set of symmetries must be closed, since any combination of symmetric transformations of a dynamical system is itself a symmetry. Thus, the set of symmetries forms a group, which is itself a subgroup of $GL(V)$, or they can be thought of as the representation of a group Γ. Furthermore, if the set of symmetries forms a compact Lie group, then it can be show that it is a subgroup of $\mathbf{O}(n)$, the group of orthogonal $n \times n$ matrices [?]. If a dynamical system is invariant under symmetry group Γ, that system is said to be Γ-*equivariant*. For any point in state space x in a Γ-equivariant dynamical system we refer to the subgroup of Γ that leaves x unchanged as Σ_x, the *isotropy*
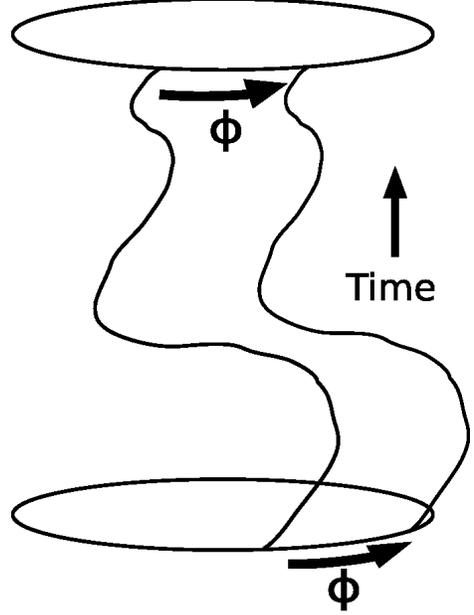
Figure 6: In equivariant dynamical systems, a symmetry operation commutes with time evolution.

subgroup of x. The set of all points $x \in V$, which are Σ-invariant is referred to as the *fixed point subspace of* Σ or Fix Σ. If the dimension of that space is 1, then Σ is called *axial*.

This notion of equivariance provides some powerful tools for understanding a dynamical system. Since symmetries commute with time evolution of dynamical systems, the isotropy subgroup of any orbit remains fixed. Or equivalently, Fix Σ is flow invariant. If $x \notin$ Fix Γ, then Γ maps it to other points with the same dynamical behavior. That is to say, symmetry operations map equilibria to equilibria, periodic orbits to periodic orbits, etc..

Another striking implication of equivariance is the one that it has for the structure of the stability matrix, $D\mathbf{F}$. Suppose $\mathbf{u}$ is an equilibrium, such that $\gamma\mathbf{u} = \mathbf{u}$, and $\gamma^2 = 1$. Then all eigenfunctions of the stability matrix of $\mathbf{u}$, $D\mathbf{F_u}$, must be either symmetric or antisymmetric with respect to γ. To see this, first note that the stability matrix commutes with all elements of the symmetry group thanks to the chain rule. Therefore we have

$$D\mathbf{F_u}\gamma\mathbf{v} = \gamma D\mathbf{F_u}\mathbf{v} = \lambda\gamma\mathbf{v} \tag{38}$$

Since λ has multiplicity 1, then $\gamma\mathbf{v} = c\mathbf{v}$ for some $c \in \mathbb{C}$. Applying γ a second time gives $= \mathbf{c^2v}$. This implies that $c = \pm 1$ and therefore $\gamma\mathbf{v} = \pm\mathbf{v}$. As we will see later this situation is quite common for plane Couette flow.

As a representation, a symmetry group may be reducible or irreducible. If it is irreducible, then there are no subspaces of V which are Γ invariant other than V itself and 0. If the action on a subspace of V is irreducible, then Γ is said to act *irreducibly* on that subspace. In general, if V is not Γ-irreducible, then it can be decomposed[**?**] into a series of subspaces $V_1, \ldots, V_s$, such that $V = V_1 \oplus \cdots \oplus V_s$. Schur's Lemma states that if a linear operator commutes with all elements of an irrep, then it must by proportional to the identity. If that proportionality constant is real, then Γ acts *absolutely irreducibly*.

This has important implications for bifurcations:

Theorem 1 (The Equivariant Branching Lemma [**?**]). *Let $\Gamma \subseteq \mathbf{O(n)}$ be a compact Lie group.*

    1. Assume Γ acts absolutely irreducibly on $\mathbb{R}^N$

<center>17</center>

2. Let $f(x, \lambda)$: $\mathbb{R}^N \times \mathbb{R} \to \mathbb{R}^N$ be Γ-equivariant. Where λ is treated as a bifurcation parameter. Γ equivariance implies that

$$f(0, \lambda) \equiv 0.$$

This means that $df_{0,\lambda}$ commutes with Γ, so by absolute irreducibility:

$$(df)_{0,\lambda} = c(\lambda)\mathbf{1}$$

3. Assume $c(0) = 0$ (this is the condition for a bifurcation to occur).

4. Assume $\Sigma \subseteq \Gamma$ is an axial subgroup

Then there exists a unique branch of solutions to $f(x, \lambda) = 0$ emanating from $(0,0)$ where the symmetry of the solutions is Σ.

The direct application of Theorem 1 may not be particularly obvious for systems such as plane Couette flow, where the symmetries do not act absolutely irreducibly and the isotropy groups of interest are not axial. But there are techniques to produce reduced systems where the conditions of Theorem 1 do hold. One approach is known as Lyapunov-Schmidt Reduction. This reduces a dynamical system to just the motion in a bifurcating tangent space, with the same symmetries as the full space [**?**]. For steady state bifurcations, (bifurcations involving single eigenvalue crossings), this is often enough to apply Theorem 1.

In a Hopf bifurcation, complex pair of eigenvalues of the stability matrix of an equilibrium crosses the imaginary axis. The subspace spanned by the corresponding eigenvectors is referred to as the center subspace. There is a theorem analogous to Theorem 1 for Hopf bifurcations, but we must extend the notion of a space being Γ-absolutely irreducible to being Γ-simple.

Definition 4. A space W is Γ-simple if either:

1. $W = V \oplus V$, and V is absolutely irreducible, or

2. Γ acts irreducibly, but not absolutely on W

Generically, the center subspace of an equilibrium at Hopf Bifurcation is Γ-simple [**?**]. Finally, the notion of an isotropy group being axial is extended to that of being $\mathbb{C}$-axial. In that case, the dimension of Fix Σ is two. In such a case, there is another temporary symmetry of the system at bifurcation, given by the action of $\mathbf{S}^1$, rotation in the center subspace, around the equilibrium. With that in mind, we state the Equivariant Hopf Theorem:

Theorem 2. (Equivariant Hopf Theorem) [**?**] Let a compact Lie group Γ act simply, orthogonally, and nontrivially on $\mathbb{R}^{2m}$. Assume that

1. $f : \mathbb{R}^{2m} \times \mathbb{R} \to \mathbb{R}^{2m}$ is Γ-equivariant. Then $f(0, \lambda) = 0$ and $(df)_{0,\lambda}$ has eigenvalues $\sigma(\lambda) \pm \iota\rho(\lambda)$ each of multiplicity m.

2. $\sigma(0) = 0$ and $\rho(0) = 1$.

3. $\sigma'(0) \neq 0$ - the eigenvalue crossing condition.

4. $\Sigma \subseteq \Gamma \times S^1$ is a $\mathbb{C}$-axial subgroup.

Then there exists a unique branch of periodic solutions with period $\approx 2\pi$ emanating from the origin, with spatio-temporal symmetries Σ.

So, like in the case of steady state bifurcations, the symmetry of the Hopf bifurcating solutions carry the isotropy subgroup of the tangent space at bifurcation.

3.1.4 Irreducible Representations and Equivariance

Now, if we know that fixed point subspaces are flow invariant, what can we say about how the rest of state space mixes? Many interesting dynamical systems such as Navier-Stokes equations, Kuramoto-Sivashinsky equation, and the Lorenz equation, can be brought to the form of bilinear ODE:

$$\dot{a}_i = v_i(\mathbf{a}) = L_{ij}a_j + \frac{1}{2}B_{ijk}a_ja_k \,, \qquad a_j \in \mathbb{U} \in \mathbb{R}^d \,. \tag{39}$$

If Γ is a finite discrete group or compact Lie group, state space $\mathbf{U}$, can be decomposed into its projections on to the irreps of Γ. Let $P^{(\alpha)}$, be the projection operator onto the irrep of Γ $\mathbf{U}^{(\alpha)}$. Then,

$$1 = \sum_\alpha P^{(\alpha)} \,. \tag{40}$$

Denote the component of a vector, $\mathbf{a}$ projected onto $\mathbf{U}^{(\alpha)}$ as $\mathbf{a}^{(\alpha)}$

$P^{(\alpha)}$ applied to (39) yields:

$$\dot{a}_i^{(\alpha)} = L_{ij}a_j^{(\alpha)} + \frac{1}{2}B_{ijk}P^{(\alpha)}\sum_{\beta,\gamma} a_j^{(\beta)}a_k^{(\gamma)} \,. \tag{41}$$

Denote by $C^\alpha{}_{\beta\gamma}$ the Clebsch-Gordan coefficients that project subspace α of the reducible Kronecker product $\mathbb{U}^\beta \otimes \mathbb{U}^\gamma$,

$$P^{(\alpha)}\mathbf{a}^{(\beta)}\mathbf{a}^{(\gamma)} = C^\alpha{}_{\beta\gamma}\mathbf{a}^{(\beta)}\mathbf{a}^{(\gamma)} \,. \tag{42}$$

So (41) becomes,

$$\dot{a}_i^{(\alpha)} = L_{ij}a_j^{(\alpha)} + \frac{1}{2}B_{ijk}\sum_{\beta,\gamma} C^\alpha{}_{\beta\gamma}a_j^{(\beta)}a_k^{(\gamma)} \,. \tag{43}$$

As time evolves, the bilinear term of (39) the different subspaces, so the space $\mathbf{U}^\alpha$ is flow invariant if and only if $\mathbf{a}^{(\beta)} = 0$ and $C^\beta{}_{\alpha\alpha}$ is zero for all $\beta \neq \alpha$. In this case, the system reduces to:

$$\begin{aligned}
\dot{a}_i^{(\alpha)} &= L_{ij}a_j^{(\alpha)} + \frac{1}{2}B_{ijk}C^\alpha{}_{\alpha\alpha}a_j^{(\alpha)}a_k^{(\alpha)} \\
\dot{a}^{(\beta)} &= a^{(\beta)} = 0 \,, \qquad \forall \beta \neq \alpha \,.
\end{aligned} \tag{44}$$

Thus, a flow-invariant subspace does not need to be an irrep of Γ - a sub-collection of irreps $\bigotimes_\alpha \mathbf{U}^\alpha$ can be mixed by the flow, without reaching the full space $\mathbf{U}$.

3.2 Discrete Symmetry: The Lorenz Attractor

Before examining the symmetry of plane Couette flow, we will first consider a simpler system with symmetry. The Lorenz system [?] is a $3D$ system derived by Edward Lorenz as a three mode truncation of Rayleigh-Benard flow, the flow induced in a fluid by a temperature gradient.

$$
\begin{aligned}
\dot{x} &= \sigma(y - x) \\
\dot{y} &= \rho x - y - xz \\
\dot{z} &= xy - bz
\end{aligned}
\tag{45}
$$

σ, ρ, and b are taken as adjustable parameters to the system. It possesses one discrete symmetry, rotation by π about the z-axis:

$$
\gamma(x, y, z) = (-x, -y, z)
\tag{46}
$$

Customarily, σ and b are fixed to be 10 and 8/3 respectively, while ρ is varied. For small values of ρ, the system has one stable equilibrium, $EQ0 = (0, 0, 0)$. This equilibrium is the center of the symmetric subspace for this system, the z-axis. EQ0 is always stable inside this subspace. But in the full space there is a pitchfork bifurcation in which EQ0 becomes unstable and two new equilibria are created as ρ is increased:

$$
EQ_{\pm} = \left(\pm\sqrt{b(\rho - 1)}, \pm\sqrt{b(\rho - 1)}, \rho - 1 \right).
\tag{47}
$$

These two equilibria are related by γ, as the must according to 1.

The eigenvalues of the three equilibria given by:

$$
\begin{aligned}
EQ_0 \quad &: \quad (\lambda_+, \lambda_-, \lambda_s) = (-\sigma - 1 \pm \sqrt{(\sigma - 1)^2 + 4r\sigma}, -b) \\
EQ_{1,2} \quad &: \quad \text{roots of } \lambda^3 + \lambda^2(\sigma + b + 1) + \lambda b(\sigma + r) + 2\sigma b(r - 1) = 0.
\end{aligned}
\tag{48}
$$

The EQ_0 $1d$ unstable manifold closes into a homoclinic orbit at $r \approx 13.56$. Beyond that, an infinity of associated periodic orbits are generated, until $r \approx 24.74$, where EQ_1, EQ_2 undergo a Hopf bifurcation. For $r > 24.74$ $EQ_{1,2}$ have one stable real eigenvalue, and one unstable complex conjugate pair as solutions to (48), leading to a spiral-out instability.

As ρ is increased further the system undergoes a series of global bifurcations [?], and chaos sets in. For $\rho = 28$, which is in this regime, the system has a strange attractor [?].

The symmetry of the system is apparent when looking at the attractor. It consists of two flat spirals joined at right angles. The two nonzero equilibria, $EQ_\pm$, sit at the center of these spirals. The attractor is invariant under the action $\gamma(x, y, z) = (-x, -y, z)$, as it must be, since the system is γ-equivariant.

γ-equivariance decomposes the space into two irreducible subspaces $\mathbb{U} = \mathbb{U}^+ \oplus \mathbb{U}^-$, the z-axis $\mathbb{U}^+$ and the $[x, y]$ plane $\mathbb{U}^-$. The projection operators onto these two subspaces are given by:

$$
P^+ = \frac{1}{2}(1 + R) = \begin{pmatrix} 0 & 0 & 0 \\ 0 & 0 & 0 \\ 0 & 0 & 1 \end{pmatrix}, \qquad P^- = \frac{1}{2}(1 - R) = \begin{pmatrix} 1 & 0 & 0 \\ 0 & 1 & 0 \\ 0 & 0 & 0 \end{pmatrix}.
\tag{49}
$$

The $1d$ $\mathbb{U}^+$ subspace is the fixed-point subspace $\text{Fix}\,\gamma$, with the full state space Lorenz equation (45) reduced to the linear contraction to the EQ_0 equilibrium:

$$
\dot{z} = -bz,
$$
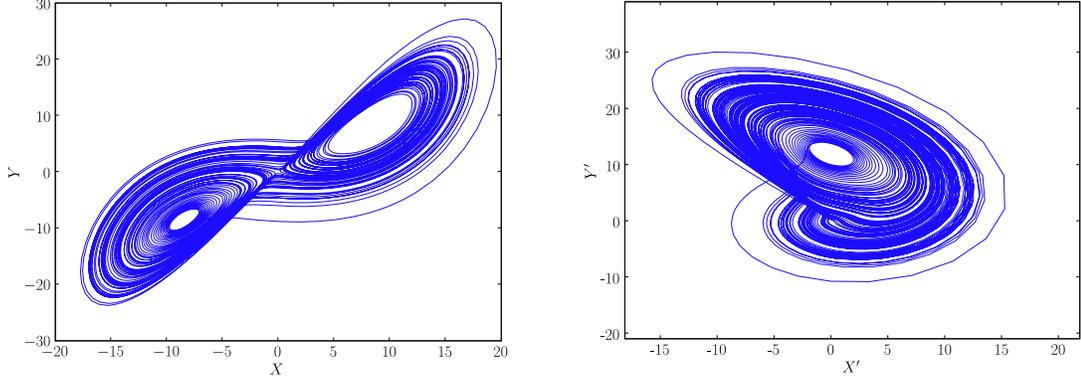
Figure 7: Left: XY projection of the two-eared Lorenz attractor. Right: $X'Y'$ projection of desymmetrized Lorenz attractor – The one-eared "Van Gogh" attractor.

The dynamics in $\mathbb{U}^+$ are rather trivial in this case, but in higher-dimensional state spaces the flow-invariant $\mathbb{U}^+$ subspace can be itself high-dimensional, with interesting dynamics.

The $\mathbb{U}^-$ subspace is *not* flow-invariant - the nonlinear terms in the Lorenz equation (45) send initial conditions within $\mathbb{U}^-$ into the whole $\mathbb{U}$ - but γ symmetry is nevertheless very useful. By defining a Poincaré section $\mathcal{P}$ to be any plane containing the z axis, the state space is divided into a half-space fundamental domain $\tilde{\mathbb{U}}$ and its 180° rotation $\gamma\tilde{\mathbb{U}}$. Then the dynamics can be reduced to fundamental domain, with any trajectory that pierces $\mathcal{P}$ reinjected through a 180° rotation. Full space pairs p, γp map into a single cycles $\tilde{p}$ in the fundamental domain, and any self-dual cycle $p = Rp = \tilde{p}\gamma\tilde{p}$ is a repeat of a relative periodic orbit $\tilde{p}$.

This system is twice as complicated as it needs to be. We are viewing it through the kaleidoscope of symmetry. The situation is simplified by looking at the quotient space, were each pair of points which are equivalent under γ are mapped to the same point.

We do this explicitly by means of a double cover – converting to cylindrical coordinates and doubling the polar angle. That is, we apply the map

$$\pi(r\cos\theta, r\sin\theta, z) = (r\cos 2\theta, r\sin 2\theta, z) \tag{50}$$

The result is plotted in figure 7.

3.3 Symmetries of Plane Couette Flow

The simplest invariant solutions are equilibria (steady states) or fixed profile time-invariant solutions,

$$\mathbf{u}(\mathbf{x}, t) = \mathbf{u}_{\text{EQ}}(\mathbf{x}), \tag{51}$$

and relative equilibria (traveling waves, rotating waves), characterized by a fixed profile $\mathbf{u}_{\text{TW}}$ moving in the $[x, z]$ plane with constant velocity $\mathbf{c}$,

$$\mathbf{u}(\mathbf{x}, t) = \mathbf{u}_{\text{TW}}(\mathbf{x} - \mathbf{c}t), \qquad \mathbf{c} = (c_x, 0, c_z). \tag{52}$$

Here the suffix EQ or TW labels a particular invariant solution.

The Navier-Stokes equations for plane Couette flow (13) are invariant under a reflection in z (referred to as σ_1), rotation by π about z (referred to as σ_2), and continuous translations

21

in x and z, referred to as $\tau(\ell_x, \ell_z)$. Flows invariant under discrete and continuous symmetries allow for both equilibrium and relative equilibrium solutions. Equilibria can also be symmetric under discrete translations, corresponding to the number of streamwise streak periods and spanwise rolls that can be accommodated within a fixed periodic $[L_x, 2, L_z]$ cell. Most of the equilibria discussed here are symmetric with respect to the 'shift-reflect' symmetry $s_1 = \tau(L_x/2, 0)\,\sigma_1$ and the 'shift-rotate' symmetry $s_2 = \tau(L_x/2, L_z/2)\,\sigma_2$. These symmetry operations form a group $S = \{1, s_1, s_2, s_3\}$, $s_3 = s_1 s_2$ (dihedral group D_2) which acts on velocity fields $\mathbf{u}$ as

$$
\begin{aligned}
s_1\,[u, v, w](x, y, z) &= [u, v, -w](x + L_x/2, y, -z) \\
s_2\,[u, v, w](x, y, z) &= [-u, -v, w](-x + L_x/2, -y, z + L_z/2) \\
s_3\,[u, v, w](x, y, z) &= [-u, -v, -w](-x, -y, -z + L_z/2)\,.
\end{aligned}
\tag{53}
$$

As σ_1 reverses the spanwise velocity w, and σ_2 reverses the streamwise velocity u, relative equilibria invariant under σ_1 have vanishing spanwise velocity $c_z = 0$, and those invariant under σ_2 have vanishing streamwise velocity $c_x = 0$. Schmiegel [?] credits Nagata [?] and Busse and Clever [?, ?] with introducing the S-symmetry, and refers to it as the 'NBC-symmetry.'

Implicit in the σ_1, σ_2 definitions (and consequently the definition of S) is the choice of the origin $(x, y, z) = (0, 0, 0)$: σ_1 is a reflection across $z = 0$, and σ_2 is a π-rotation round origin $(0, 0)$ in the (x, y)-plane. If a velocity field $\mathbf{u}$ is invariant under s_1, s_2, then any translation of it, $\tau(\ell_x, \ell_z)\,\mathbf{u}$, is invariant under $\tau(0, 2\ell_z)\,s_1$, $\tau(2\ell_x, 0)\,s_2$ respectively. The asymmetry of a velocity field $\mathbf{u}$ with respect to s_1 or s_2 can thus be minimized (and possibly zeroed) by shifting the (x, z) origin of (53) by (ℓ_x, ℓ_z)

$$
\begin{aligned}
\tau(0, 2\ell_z)s_1\,[u, v, w](x, y, z) &= [u, v, -w](x + L_x/2, y, -z + 2\ell_z) \\
\tau(2\ell_x, 0)s_2\,[u, v, w](x, y, z) &= [-u, -v, w](-x + L_x/2 + 2\ell_x, -y, z + L_z/2) \\
\tau(2\ell_x, 2\ell_z)s_3\,[u, v, w](x, y, z) &= [-u, -v, -w](-x + 2\ell_x, -y, -z + L_z/2 + 2\ell_z)\,,
\end{aligned}
\tag{54}
$$

and monitoring the magnitude of the symmetric/antisymmetric norms $||(1 \pm s_j')||$.

Typical states for the small aspect cells we study here tend to exhibit two large, counter-rotating streamwise rolls, with a streamwise wobble of wavelength L_x. Our choice of z origin centers the rolls, and x origin mirrors them across half cell length.

Consider next the subgroup $S_3 = \{1, s_3\} \subset S$ (isomorphic to dihedral group D_1). The s_3 operation flips both the streamwise x and the spanwise z, thus eliminating invariance under both x and z continuous translations.

Let $\mathbb{U}$ be the space of square-integrable, real-valued velocity fields that satisfy the kinematic conditions of plane Couette flow:

$$
\begin{aligned}
\mathbb{U} = \{\mathbf{u} \in L^2(\Omega) \mid &\boldsymbol{\nabla} \cdot \mathbf{u} = 0,\ \mathbf{u}(x, \pm 1, z) = 0, \\
&\mathbf{u}(x, y, z) = \mathbf{u}(x + L_x, y, z) = \mathbf{u}(x, y, z + L_z)\}\,.
\end{aligned}
\tag{55}
$$

We denote the S-invariant subspace of states invariant under symmetries (53) by

$$
\mathbb{U}_S = \{\mathbf{u} \in \mathbb{U} \mid s_j \mathbf{u} = \mathbf{u},\ \ s_j \in S\}\,,
\tag{56}
$$

and the S_3-invariant subspace by

$$
\mathbb{U}_{S3} = \{\mathbf{u} \in \mathbb{U} \mid s_3 \mathbf{u} = \mathbf{u},\ \ s_1 \mathbf{u} \neq \mathbf{u},\ \ s_2 \mathbf{u} \neq \mathbf{u}\}\,,
\tag{57}
$$

22

where $\mathbb{U}_S \subset \mathbb{U}_{S3} \subset \mathbb{U}$. $\mathbb{U}_S$ and $\mathbb{U}_{S3}$ are flow-invariant subspaces: states initiated in either remain within it under the Navier-Stokes dynamics.

Translations of half the cell length in the spanwise and/or streamwise directions commute with S. These operators generate a discrete subgroup of the continuous translational symmetry group $SO(2) \times SO(2)$:

$$T = \{e, \tau_x, \tau_z, \tau_{xz}\}, \qquad \tau_x = \tau(L_x/2, 0)\,, \ \tau_z = \tau(0, L_z/2)\,, \ \tau_{xz} = \tau_x \tau_z\,. \tag{58}$$

Since the action of T commutes with that of S, the three half-cell translations $\tau_x \mathbf{u}$, $\tau_z \mathbf{u}$, and $\tau_{xz} \mathbf{u}$ of $\mathbf{u} \in \mathbb{U}_S$ are also in $\mathbb{U}_S$.

CHAPTER IV

METHODOLOGY

One impediment to the study of the Navier-Stokes equations as a dynamical system is the complexity of the numerical machinery that one must use to study it. There are two major families of approaches to computing solutions of the Navier-Stokes equations: modeling and direct numerical simulation (DNS). In modeling approaches one makes some ansatz about the nature of the flow and then proceeds to solve a truncated system. DNS, by contrast makes no assumptions beyond first principles and basic mathematical assumptions like smoothness. It is more computationally expensive, but recent advancements in computing power make it a more reasonable approach than it once was. Modeled approaches suffer from questions about their accuracy, and their physical relevance in some circumstances [?].

Development of direct numerical simulation (DNS) algorithms for the Navier-Stokes equations is an active topic of research in its own right. A major difficulty in integrating the Navier-Stokes equations is choosing the right method for enforcement of the incompressibility constraint. This problem can also be restated in terms of computing the pressure at each time step. Since the Navier-Stokes equations do not have an explicit evolution equation for the pressure, it must either be eliminated or solved for in such a way that incompressibility is maintained by the DNS algorithm.

Due to the size and complexity of the discretized system, one loses an analytic handle on the system. Instead, the DNS is treated more or less as a black box. Computing equilibria requires the use of Newton's method, but computation of the fundamental matrix is impractical due to its size. Instead we must rely on iterative Krylov subspace methods, which can compute an approximate solution to the Newton equation through repeated integrations of the CFD algorithm on trial solutions.

4.1 Discretization and the Method of Lines

All numerical integrations of the Navier-Stokes equations in this thesis have been performed using `Channelflow` [?], an open source library for performing direct spectral simulation of the Navier-Stokes equations in channel geometries written by John F. Gibson. Without this software package, the difficulty of completing this thesis would have been increased by an order of magnitude.

4.1.1 Spatial Discretization

When solving partial differential equations such as the Navier-Stokes equations, one represents the solutions by some spatial discretization or truncated function basis. In the case of plane Couette flow, the velocity fields are commonly represented by expansion in a series which is the product of two Fourier series and Chebyshev polynomials.

$$\mathbf{u}(x,y,z) = \sum_{j,k,l} a_{jkl} e^{-\imath j 2\pi x/L_x} e^{-\imath k 2\pi z/L_z} T_l(y)$$

Fourier series are the natural choice to use for expansion in the periodic streamwise and spanwise directions. For infinitely smooth functions with periodic derivatives, Fourier expansion obtains 'spectral accuracy.' That is, the magnitude of the coefficients drops off faster than any power of $\dfrac{1}{N}$ [**?**]. This allows us to accurately represent a velocity field with truncated Fourier series.

Fourier series are also nice for efficiency reasons. Algorithms exist to compute a discrete Fourier transform (DFT) in $O(N \log N)$ operations. There are many efficient, freely available codes for doing this. For this thesis, FFTW was used for this purpose extensively [**?**] Another advantage to the use of Fourier series is that, differentiation of a function expanded in a Fourier series is computationally cheap:

$$\partial_x f(x) = \sum_j \partial_x a_j e^{ijx} = \sum_j ij a_j e^{ijx} \tag{59}$$

For plane Couette flow, the boundary conditions in the wall-normal direction are a combination of Dirichlet and Neumann conditions. Chebyshev polynomials are used as a basis in this direction rather than a Fourier series. The velocity fields are evaluated on a Gauss-Lobatto grid defined by:

$$y_j = \cos \frac{\pi j}{N_y} \qquad j = 0, 1, \ldots, N_y \,, \tag{60}$$

The reason for this lies in the identity:

$$T_k(\cos \theta) = \cos k\theta \tag{61}$$

Because of this, the transformation from grid point values to a Chebyshev polynomial can be done be a discrete cosine transform, a special case of a DFT. Another benefit of using this grid is that it is finer at the boundaries, which is where the smaller scale features in plane Couette flow appear.

4.1.2 Temporal Discretization

While a spectral method is used for spatial discretization, time discretization is done using finite differences. In doing so, the spatial discretization is fixed and the partial differential equation:

$$\frac{\partial u}{\partial t} = f(u) \,, \tag{62}$$

is replaced by the ordinary differential equation

$$\frac{dU}{dt} = F(U) \,. \tag{63}$$

Here U and $F(U)$ are the spectral projections of u and $f(u)$, done in such a way that the boundary conditions are satisfied. This is called the 'method-of-lines' approach [**?**].

Methods for temporal discretization roughly separate into two types: explicit and implicit methods. In explicit methods, U^n, the value of U at time step n, only depends on the values of F, and U at previous time steps: F^{n-1}, U^{n-1}, etc.. One class of such methods are

25

the Adams-Bashforth Methods. They are numbered by their order, the number of previous steps which they depend on. The first few [?] are:

$$\text{AB1: } U^{n+1} = U^n + \delta t F^n$$

$$\text{AB2: } U^{n+1} = U^n + \delta t \left(\frac{3}{2} F^n - \frac{1}{2} F^{n-1} \right) \tag{64}$$

$$\text{AB3: } U^{n+1} = U^n + \delta t \left(\frac{23}{12} F^n - \frac{16}{12} F^{n-1} + \frac{5}{12} F^{n-2} \right) .$$

The first order method AB1 is equivalent to the forward Euler method, the simplest explict scheme.

Another class of commonly used explicit methods are the Runge-Kutta methods. These methods use a linear combination of F for various values of U. This can be thought of as taking each time step in various stages. The fourth-order version of this (RK4) is [?]:

$$
\begin{aligned}
K_1 &= F(U^n) \\
K_2 &= F(U^n + \frac{1}{2} \delta t K_1) \\
K_3 &= F(U^n + \frac{1}{2} \delta t K_2) \\
K_4 &= F(U^n + \delta t K_3) \\
U^{n+1} &= U^n + \frac{1}{6} \delta t \left(K_1 + 2K_2 + 2K_3 + K_4 \right)
\end{aligned}
\tag{65}
$$

In contrast to explicit methods, in implicit methods, the value of U^{n+1} is made to depend on the value of $F(U^{n+1})$. One such method is the Crank-Nicholson scheme (CN):

$$U^{n+1} = U^n + \frac{1}{2} \delta t \left(F^{n+1} + F^n \right) \tag{66}$$

This scheme is commonly used to handle time-stepping for diffusion terms. [?] It has the advantage of being absolutely stable, however like other implicit methods, it requires the inversion of F. For solving Navier-Stokes equations, it is common to use CN for stepping the viscous term and Adams-Bashforth for the nonlinear terms.

4.2   A Survey of Methods for Integrating the Navier-Stokes Equations

The incompressiblity constraint of the Navier-Stokes equations presents a challenge, making their integration less straightforward. The pressure does not have an explicit evolution equation, so often it is chosen in such a way that the incompressibility constraint is satisfied. There is a large body of work going back to the 1960s discussing techniques for dealing with this difficulty associated with direct numerical simulation of the Navier-Stokes equations.

4.2.1   Primitive Variables

The approach used by Channelflow [?], which is what is used for most of this work is referred to as the method of Primitive Variables. In this approach, the velocity field itself is integrated rather than some quantity derived from it, and the pressure is chosen in such a way that it corrects the forcing from the Navier-Stokes equations in such a way that incompressibility is maintained.

To demonstrate this approach, we first start with the Navier-Stokes equations for the deviation from laminar flow (13), with the incompressibility constraint and boundary conditions:

$$\frac{\partial \mathbf{u}}{\partial t} + y\frac{\partial \mathbf{u}}{\partial x} + v\,\hat{\mathbf{x}} + \mathbf{u}\cdot\nabla\mathbf{u} = -\nabla p + \frac{1}{Re}\nabla^2\mathbf{u} \tag{67}$$

$$\nabla \cdot \mathbf{u} = 0 \tag{68}$$

$$\mathbf{u}|_{y=\pm1} = 0 \tag{69}$$

The streamwise and spanwise directions are interpolated on a rectangular grid, and represented by a Fourier expansion. This expansion is written as

$$\mathbf{u}(x,y,z,t) = \sum_{kx,kz} \hat{\mathbf{u}}_{kx,kz}(y,t)e^{i2\pi k_x x/L_x}e^{i2\pi k_z z/L_z}\,, \tag{70}$$

where kx and kz index the x and z Fourier coefficients respectively.

A staggered grid is used in the wall normal direction, with the velocity evaluated at the points:

$$y_j = \cos\frac{\pi j}{N_y} \qquad j = 0,1,\ldots,N_y\,, \tag{71}$$

and the pressure evaluated at the points halfway between the velocity points:

$$y_{j+1/2} = \cos\frac{\pi\,(j+1/2)}{N_y} \qquad j = 0,1,\ldots,N_y - 1\,. \tag{72}$$

A discrete cosine transform of u in y direction, gives us the velocity field expressed as a sum of Chebyshev polynomials, $T_m(y)$. So, the velocity field is represented as

$$\hat{\mathbf{u}}_{kx,kz}(y,t) = \sum_{m=0}^{N_y} \tilde{\mathbf{u}}_{k_x,k_z,m}(t)T_m(y)\,, \tag{73}$$

Similarly, the pressure is represented as

$$\hat{P}_{kx,kz}(y,t) = \sum_{m=0}^{N_y-1} \tilde{P}_{kx,kz,m}(t)T_m(y)\,. \tag{74}$$

For the purposes of this section, (13) Crank-Nicholson discretization is used for the pressure and viscous terms, and Adams-Bashforth is used for the nonlinear term. Applying this discretization and Fourier transforming (13), we end up with

$$\frac{1}{Re}\partial_y^2\hat{\mathbf{u}} - \lambda\hat{\mathbf{u}} - \hat{\boldsymbol{\nabla}}\hat{P} = -\hat{\mathbf{R}} \tag{75}$$

$$\hat{\boldsymbol{\nabla}} \cdot \hat{\mathbf{u}} = 0 \tag{76}$$

$$\hat{\mathbf{u}}(\pm1) = 0\,, \tag{77}$$

where

$$\hat{\mathbf{R}}^n = \frac{2}{\delta t}\left(\hat{\mathbf{u}}^n - \hat{k}^2\hat{\mathbf{u}}^n\right) + 3\hat{\mathbf{H}}^n - \hat{\mathbf{H}}^{n-1} - \hat{\boldsymbol{\nabla}}\hat{P}^n + \partial_y^2\hat{\mathbf{u}}^n \tag{78}$$

$$\hat{\mathbf{H}} = (\mathbf{u}\cdot\nabla)\mathbf{u} + y\frac{\partial\mathbf{u}}{\partial x} + v\,\hat{\mathbf{x}} \tag{79}$$

$$\lambda = \frac{2}{\delta t} + \frac{1}{Re}\hat{k}^2 \tag{80}$$

$$\tag{81}$$

27

Taking the divergence of (75) gives us a Helmholtz equation for the pressure:

$$\hat{P}'' - \hat{k}^2\hat{P} = \hat{\boldsymbol{\nabla}} \cdot \hat{\mathbf{R}} \,. \tag{82}$$

The boundary condition for this is taken from the incompressibility condition, evaluated at the walls,

$$\hat{\boldsymbol{\nabla}} \cdot \hat{\mathbf{u}}(\pm 1) = \partial_y v(\pm 1) = 0 \tag{83}$$

So, the pressure equation must be solved simultaneously with the wall-normal component of (75),

$$\frac{1}{Re}\hat{v}'' - \lambda\hat{v} - \hat{P}' = -\hat{\mathbf{R}}_y \,, \hat{v}(\pm 1) = 0 \,. \tag{84}$$

This is done be means of the 'influence-matrix' method [**?**]. The boundary conditions on the pressure - wall normal velocity system are in terms of v only: $v(\pm 1) = 0$ from the no slip boundary condition and $v'(\pm 1) = 0$ from the incompressibility condition. Once these are solved for, the streamwise and spanwise components can be updated.

The 'influence-matrix' method is used to solve for $\hat{P},\hat{v}$. Call (82–84) the "A-problem." Consider another system, the "B-problem", where the condition $\partial_y v(\pm 1) = 0$ is replaced with inhomogeneous Dirichlet conditions on $\hat{P}$, $\hat{P}(\pm 1) = \hat{P}_{\pm}$. Now we solve the B problem for three different set of values of $\hat{P}_{\pm}$: $(0,0)$, $(1,0)$,$(0,1)$. Let $(\hat{P}_p, \hat{v}_p),(\hat{P}_+, \hat{v}_+)$, and $(\hat{P}_-, \hat{v}_-)$, be the solutions for the three set of boundary conditions respectively. The solution to the A-problem is a linear combination of the three:

$$\hat{P} = \hat{P}_p + \delta_+\hat{P}_+ + \delta_-\hat{P}_- \tag{85}$$
$$\hat{v} = \hat{v}_p + \delta_+\hat{v}_+ + \delta_-\hat{v}_- \,, \tag{86}$$

where $\delta_{\pm}$ are computed so that the original boundary conditions are satisfied.

4.3 Krylov Subspace Methods

Let $\mathbf{F}_{\text{NS}}(\mathbf{u})$ represent the Navier-Stokes equations (13) and $\mathbf{f}_{\text{NS}}^t$ its time-t forward map

$$\frac{\partial\mathbf{u}}{\partial t} = \mathbf{F}_{\text{NS}}(\mathbf{u})\,, \qquad \mathbf{f}_{\text{NS}}^t(\mathbf{u}) = \mathbf{u} + \int_0^t d\tau\,\mathbf{F}_{\text{NS}}(\mathbf{u})\,. \tag{87}$$

In terms of the Navier-Stokes equations (87) equilibria and relative equilibria satisfy:

$$\mathbf{F}_{\text{NS}}(\mathbf{u}_{\text{EQ}}) = 0 \qquad\qquad \text{equilibrium } \mathbf{u}_{\text{EQ}} \tag{88}$$
$$\mathbf{F}_{\text{NS}}(\mathbf{u}_{\text{TW}}) = -(\mathbf{c}\cdot\boldsymbol{\nabla})\,\mathbf{u}_{\text{TW}} \qquad\qquad \text{traveling wave } \mathbf{u}_{\text{TW}}\text{, velocity } \mathbf{c}\,.$$

In order to compute the stability eigenvalues of equilibria and periodic orbits, we must linearize (87). Due to the shear size of the state space, direct evaluation is impractical. What makes these calculations tractable is that at moderate Re the dynamics in state space are effectively low dimensional. Without this property, the problem would be quite intractable, and the dynamics would most likely lack in any sort of identifiable form. Due to this, we may consider operators such as the stability matrix to be sparse. This is exactly the sort of problem that a class of algorithms known as Krylov Subspace methods are well suited for.

An important feature of Krylov subspace methods is that only matrix-vector products need to be computed. Therefore, the explicit form of a matrix is not needed. For a given matrix $\mathbf{A}$ and n dimensional vector $\mathbf{b}$, the nth Krylov subspace is defined as the subspace spanned by the vectors, $\{\mathbf{b}, \mathbf{Ab}, \dots \mathbf{A^{n-1}b}\}$. Krylov subspace methods are a class of iterative algorithms that essentially work to solve a given problem by using the solution restricted to the $(n-1)$st Krylov subspace to compute the solution in the nth.

4.3.1 Arnoldi Iteration

Arnoldi iteration is a Krylov subspace method used for computed the eigenvalues and eigenvectors of a matrix $\mathbf{A}$. Essentially, the algorithm uses stabilized Gram-Schmidt iteration to produce an orthogonal basis for the Krylov subspace. The eigenvectors of the matrix $\mathbf{A}$ are then estimated from $\mathbf{A}$'s projection onto this orthonormal basis. To do this we form the Hessenberg matrix $\mathbf{H} := \mathbf{Q}^\dagger \mathbf{A} \mathbf{Q}$, where the columns of $\mathbf{Q}$ are formed from the basis of the Krylov subspace. The eigenvectors of $\mathbf{A}$ are the same as $\mathbf{H}$. But, since H is Hessenberg, its eigenvectors may be computed quickly by means of QR decompostion. This can be done iteratively, along side the computation of

Arnoldi iteration tends to find the most dominant eigenvalues of a matrix first, so it may be stopped before finding all eigenvectors of a matrix. For the purposes of computing the stability of an equilibrium, this is desirable since it is the least stable eigenvectors of a state determine the dominant behavior in its neighborhood.

4.3.2 GMRES

The Generalized Minimal Residual method, or GMRES [**?**], is another iterative Krylov subspace method which uses Arnoldi iteration to solve the nonsymmetric linear system, $Ax = b$. GMRES finds $\mathbf{x}$ in the Krylov subspace generated by A and $\mathbf{b}$ which minimizes $\|A\mathbf{x} - \mathbf{b}\|$. This is done by expanding $\mathbf{x}$ in the basis of the Krylov subspace $\mathbf{q}_j = A\mathbf{q}_{j-1}$, so that $\mathbf{x} = \sum a_j \mathbf{q}_j$. At each step, a_j is chosen to minimizes the least squares residual. A good implementation of GMRES is a nontrivial undertaking, and so I use PETSc's GMRES [**?**] routines when the need arises.

4.4 Newton Solvers

In order to locate a flow-invariant structure such as an equilibrium or a periodic orbit, it is necessary to solve an equation of the form $F(x) = 0$, where $F(x) : \mathbb{R}^N \to \mathbb{R}^N$ is a differentiable function. There is a class of algorithms based on Newton's method that we use to do this.

In essence Newton's method works as follows: first one makes a linear approximation of the $F(x)$ around an initial guess, then the guess is refined by moving toward the zero of the linear model, and then the procedure is repeated until the value of $F(x)$ is sufficiently small. More explicitly, at each step of the iteration one creates a local linear model [**?**]

$$M_n(x) = F(x_n) + DF(x_n)(x - x_n), \tag{89}$$

where DF is the matrix of partial derivatives of F. In the simplest case, the next point in the iteration is taken to be the root of (89). This means we must solve

$$F(x_n) + DF(x_n)(x_{n+1} - x_n) = 0 \tag{90}$$

or

$$x_{n+1} = x_n - DF^{-1}(x)F(x). \tag{91}$$

Since we typically work with Navier-Stokes discretizations on the order of 10^5 - 10^6, accurately evaluating (91) is numerically difficult. So, we relax the condition for choosing the step, $s := x_{n+1} - x_n$, to be

$$\|DF(x_n)s + F(x_n)\| \leq \eta \|F(x_n)\| \tag{92}$$

η is a free parameter which can be adjusted to control the exactness of the Newton step. Adjusting it trades off between time solving for each Newton step and the total number of Newton iterations. Algorithms which use this condition are called Inexact Newton Methods [?].

Here, we use a type of Inexact Newton methods called Newton-Krylov methods. 'Krylov' refers to our use of Krylov subspace methods such as GMRES to solve (92). This is advantageous not only from the standpoint that it saves us from obtaining an exact solution to (91), but also it does not require explicit computation of the stability matrix. Instead, we only need to explicitly evaluate products of it with a vector. These products are easily computed as finite differences. That is,

$$J\delta x \approx \frac{F(x + h\delta x) - F(x)}{h} \, , \tag{93}$$

where h is an appropriately small step size. One approach to computing h that was used is that of [?]:

$$h = \frac{e_{rel}\sqrt{1 + \|x\|}}{\|\delta x\|} \, , \tag{94}$$

where e_{rel} the specified relative error tolerance of the algorithm.

It has the advantage of being relatively simple in that it has no tunable parameters and also is cheap to compute.

It is not necessarily desirable to jump all the way to the root of (89), since this may be quite far away, and far beyond where the local linear model is valid. So instead we take $s = \lambda d$, where $d = -DF(x_n)^{-1}F(x_n)$. λ is chosen to guarantee that the next step produces a sufficient decrease in $\|F\|$. However, through experience [?], it has been shown that it is important to take λ as close to 1 as possible for faster convergence. So the choice of λ must balance these two competing interests.

4.4.1 Termination of Newton Algorithms

There are several methods for determining when to terminate Newton iteration. One approach [?] would be to terminate when the residual is less than a combination of the absolute and relative error.

$$\|F(x)\| \leq e_{rel}\|F(x_0)\| + e_{abs} \, . \tag{95}$$

Here e_{rel} specifies the tolerance relative to the initial residual and e_{abs} specifies the absolute tolerance. Other tests may include algorithm-specific parameters, such as trust-region size for trust region solvers (see sect. 4.4.3) [?].

4.4.2 Line Search Algorithms

The most obvious condition for sufficient decrease is that $\|F(x_{n+1})\| < \|F(x_n)\|$, however this can lead to convergence to a point which is not necessarily a minimum [?]. So instead, a condition, known as the Armijo rule [?], is often used [?, ?]. For the case of a function $F : \mathbb{R}^N \to \mathbb{R}^N$, the Armijo rule is

$$\|F(x_n + \lambda d)\| < (1 - \alpha\lambda)\|F(x_n)\| \, . \tag{96}$$

α is a tunable parameter which is usually chosen to be quite small (typically $\alpha = 10^{-4}$ [?]). One class of Newton type algorithms, known as line search methods seeks to find the largest

value of $0 < \lambda \leq 1$ which satisfies (96). The general approach is as follows: First, compute the full Newton step, s. Then, check to see if $\lambda = 1$ satisfies (96). If it does not, then we must backtrack along d. This is done by checking for satisfaction of (96) for some λ between some specified limits, $0 < \lambda_l < \lambda_u < 1$. Typically, $\lambda_l = 0.1$ and $\lambda_u = 0.5$ [?]. The algorithm used for most of this work picks this λ by modeling $\|F(x_n + \lambda d)\|$ as quadratic polynomial in λ, and using the minimum of that polynomial [?] [?]. If this still fails to satisfy (96), then we must continue to backtrack. Subsequent backtracks are done with cubic polynomial fits instead of quadratic, since we now have more information about $\|F(x_n + \lambda d)\|$.

4.4.3   Model Trust Region Algorithms

While line search methods attempt to shorten the size of the Newton step until sufficient descent is achieved, trust-region methods shorten the step then try to find a better direction for the step to achieve sufficient descent. In model trust-region schemes, we try to find a step within a given *region* around our starting point where we can *trust* a local quadratic *model* used. Model trust-region algorithms are presented in terms of minimizing a function $f(x) : \mathbb{R}^N \to \mathbb{R}$, so we take $f(x) = \|F(x)\|$. The size of the trust region, δ, is determined by a local quadratic model of the f [?]. Then the size is typically reused on successive steps, until it is decided to be recomputed based on some heuristic.

Once the size of the trust region is computed, we must compute the best step to take inside this region. This is determined using a quadratic model of $f(x)$:

$$m(x + s) = f(x) + \nabla f(x)^T s + \frac{1}{2} s^T H s \tag{97}$$

where H is the Hessian of f, that is the matrix of second order partial derivatives of f, evaluated at x. The two most common methods for solving this are the 'hook step' and the 'double dogleg step.' In the 'hook step', s is found which minimizes (97) while obeying the constraint that it has to stay inside the trust region. The double dogleg [?] is modification of the 'hook-step' [?], with the curve of solutions of (97) approximated by a piecewise linear curve. The first piece follows the direction of steepest descent to the point on it which minimizes (97), then jumps off it to the edge of the trust region, along the direction towards the absolute minimizer of (97).

Most of the work in this thesis was done using cubic line searches as implemented by PETSc [?]. Other parts were done using PETSc's trust region codes, as well as a hook step code implemented by JF Gibson [?].

4.5   Finding Equilibria, Relative Equilibria, Periodic Orbits and Relative Periodic Orbits

The continuous translational symmetries of plane Couette flow present several complications. First, any specific equilibrium or periodic orbit solution is an instance of a two-parameter family of equivalent solutions obtained by translation in the periodic directions x and z. Consequently, in the Newton-descent algorithms described above, the matrix $DF^T(a)$ is rank-deficient and must be supplemented by two algebraic constraints that restrict the Newton steps to be orthogonal to the tangent plane of the symmetry. Second, the presence of continuous symmetries allows two new classes of invariant solutions: relative equilibria, and relative periodic orbits, characterized by the equation $\mathbf{u}(x + \ell_x, y, z + \ell_z, t + T) = \mathbf{f}^T(u(x, y, z, t))$. Such solutions can be found by including the ℓ_x and ℓ_z parameters as free variables in the search space [?].

Figure 8: The difficulties of visualization.

To find flow invariants, we first define the forward time map $F^T(u)$ as the function which maps state u to another state u' under the evolution of the Navier-Stokes equations for time T. Equilibria, relative equilibria, periodic orbits, and relative periodic orbits are all zeros of

$$G(u, \tau_x, \tau_z, T) = \tau_x \tau_z F^T(u) - u \qquad (98)$$

The situation is most trivial for equilibria. We set $\tau_x = \tau_z = 0$, and T is arbitrary, taken relatively large in practice. This provides some separation in the eigenspectrum of G', which greatly improves the rate of convergence of the Krylov methods used by Newton solvers. There is a trade-off in that larger values of T require longer to compute and cause F^T to become more and more nonlinear. In our calculations $T = 10$ seems to balance these two aspects well.

The two translational symmetries of plane Couette flow present some challenge here. Solutions of (98) are not isolated. And, furthermore the stability matrix is singular since it has two eigenvalues $\lambda_k = 0$, associated with the directions of translation. Restriction to a discrete symmetry invariant subspace removes this singularity. The equilibria and relative equilibria presented here are all invariant under at least one discrete symmetry.

Relative equilibria and (relative) periodic orbits present their own challenges. We can no longer fix τ_x, τ_z, or T in the case of (relative) periodic orbits. This leaves us with an under-constrained system, that is to say G is a function from $\mathbb{R}^{N+3} \to \mathbb{R}$. To fix this, we follow the approach laid out by Viswanath [**?**] . Three additional constraints are added to linear system for the Newton step, s, (91):

$$s^\dagger \partial_x u = 0, \qquad s^\dagger \partial_z u = 0, \qquad s^\dagger \partial_t u = 0 \qquad (99)$$

These 3 constraints ensure that the descent direction is normal to the directions of translations as well the direction of time evolution.

4.6 State Space Visualization

As a system with many degrees of freedom, plane Couette flow state space is difficult to visualize. In what will be referred to as the 'physical' perspective, a single snapshot in time is represented by a $3D$ plot of the velocity field or a $2D$ slice of it. Then, in order to understand the evolution of the flow, one must construct a movie or look at several plots from different perspectives. While this approach is certainly useful and has helped elucidate some of the basic physical processes involved in the flow, it has its faults as well.
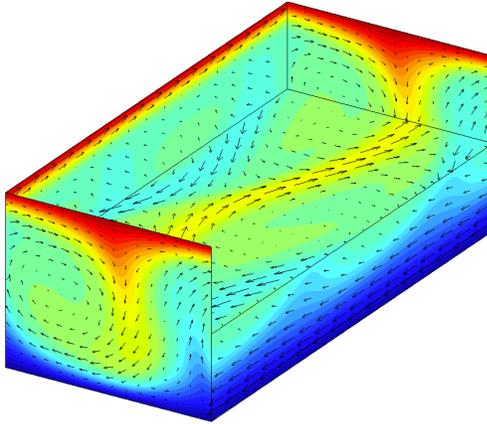
Figure 9: A typical physical visualization of plane Couette flow. In this view, the top wall moves towards the viewer, and the bottom wall moves away with equal and opposite velocity. The velocity field is coded by color and $2D$ vectors: Red - fluid moving streamwise, in the x direction; blue - fluid moving in the $-x$ direction. $[y, z]$ section vectors: fluid velocity $[0, v, w]$ transverse to the streamwise velocity u. The top half of the fluid is cut away to show the midplane velocity field $[u, 0, z]$ represented by $2D$ in-plane vectors, with streamwise velocity u also color-coded.

The two major difficulties associated with the physical perspective are: (1) it is difficult to distinguish states which can be very different from a dynamical perspective and (2) it is difficult to see how two different states might relate to each other.

In order to deal with these difficulties, a second, complementary vision is employed: state space visualization. In this perspective, a coordinate system for state space is constructed using some dynamically import states or directions. Then, each $3D$ velocity field corresponding to a instant in time is reduced to a single point by projection onto this coordinate system. In this representation, a fluid state exists as a point in an infinite-dimensional *state space*. The Navier-Stokes equations are a *state-space flow*, time-varying velocity fields as *trajectories*, steady states of the flow as *equilibria*.

This is motivated in equal parts by Hopf's vision as well as the low-dimensional modeling efforts of refs. [**?**, **?**, **?**, **?**], and others cited above, which brought dynamical systems notions such as state-space geometry and continuous symmetries to the study of turbulence. But in contrast to low-order models, the calculations are 'exact': fluid states and dynamics are represented with fully-resolved spectral CFD algorithms, with truncation errors on the order of 10^{-6}. The goals, however, are similar, and our work can be seen as an effort to link the dynamical insights of low-order modeling directly to the Navier-Stokes equations.

For example, one basis for such coordinate system could be the unstable eigenfunctions of an equilibrium. Then the coordinates for a single point in time are computed using the L^2 inner product:

$$\langle \mathbf{u}, \mathbf{v} \rangle = \frac{1}{2L_x L_z} \int_\Omega \mathbf{u} \cdot \mathbf{v} d\Omega \qquad (100)$$

This particular coordinate system can be useful for visualizing the dynamics of a neighborhood of an equilibrium.

Another class of basis is the "translation symmetric" basis. This is done by constructing sums and differences of half-cell translations of a particular dynamically important state, such as an equilibrium. This gives a set of basis elements each uniquely symmetric or antisymmetric with respect to each half-cell translation.

$$
\begin{array}{cccc}
 & \tau_x & \tau_z & \tau_{xz} \\
\mathbf{e}_1 = c_1(1 + \tau_x + \tau_z + \tau_{xz})\,\mathbf{u}_{\mathrm{EQ}} & S & S & S \\
\mathbf{e}_2 = c_2(1 + \tau_x - \tau_z - \tau_{xz})\,\mathbf{u}_{\mathrm{EQ}} & S & A & A \\
\mathbf{e}_3 = c_3(1 - \tau_x + \tau_z - \tau_{xz})\,\mathbf{u}_{\mathrm{EQ}} & A & S & A \\
\mathbf{e}_4 = c_4(1 - \tau_x - \tau_z + \tau_{xz})\,\mathbf{u}_{\mathrm{EQ}} & A & A & S \,,
\end{array}
\tag{101}
$$

As discussed in sect. C.1, the elements of T, the group of half box translations, commute with S, and S-equivariance does not imply T-equivariance. So this particular projection has the effect of 'spreading out' the 4 T related parts of $\mathbb{U}_S$ in a clean way. This projection can also be helpful in analyzing states which are not S invariant. Streamwise and spanwise motion of orbits tends to be reflected by motion in the directions which are antisymmetric under the corresponding half-cell translation.

Finally, the third type of visualization used here: the I-D plot (figure 11). This can be thought of as bridging the gap between a physical view of the Navier-Stokes equations and the state space view. I stands for the rate of energy input from the walls and D stands for the rate of energy dissipation in the bulk. These are defined in (19) and (18) respectively. A plot of I versus D can be thought of as a particular projection of state space. These two quantities must be in balance for flow invariant structures, since they must have constant total kinetic energy on average. In particular, equilibria and relative equilibria must lie on the line $I = D$, and the turbulent attractor must be centered on it.
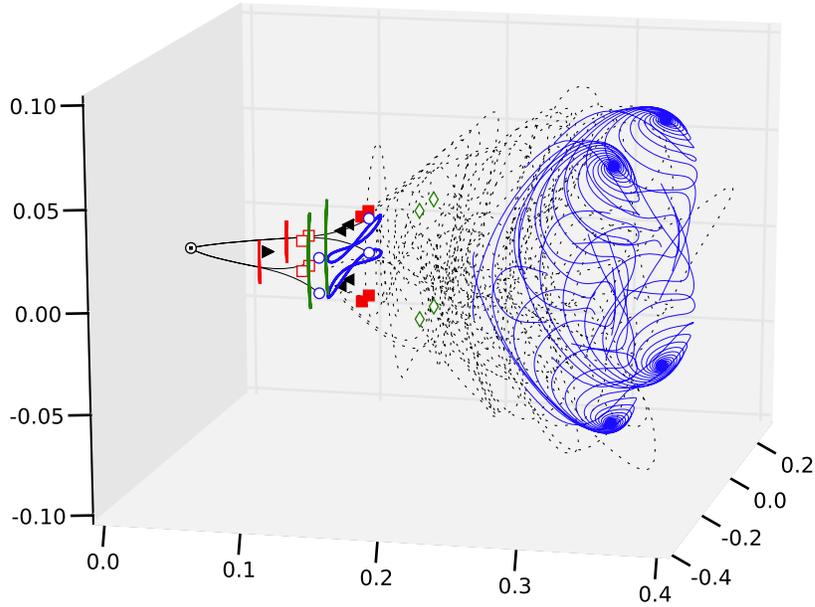
Figure 10: All equilibria and relative equilibria discussed in this paper, and the natural measure built up by long turbulent transients (cloud of green dots). Equilibria, marked ($\circ$) EQ_1 together with (black lines) $EQ_1 \to EQ_0$ heteroclinic connections, ($\bullet$) EQ_2 together with the $\mathbb{U}_S$ part of its unstable manifolds, ($\square$) EQ_3, ($\blacksquare$) EQ_4, ($\diamond$) EQ_5, ($\triangleleft$) EQ_7, ($\blacktriangleright$) EQ_9, ($\triangledown$) EQ_{10}, ($\blacktriangledown$) EQ_{11} are discussed in chapter 5. Relative equilibria trace out "bow-ties," blue for spanwise TW_1, red for streamwise TW_2, and green for streamwise TW_3, and discussed in chapter 5. A 3-dimensional projection from the ∞-dimensional state space onto the translational basis, Equation 101, constructed from equilibrium EQ_2. Narrow aspect ratio cell Ω_{w03}, $Re = 400$.
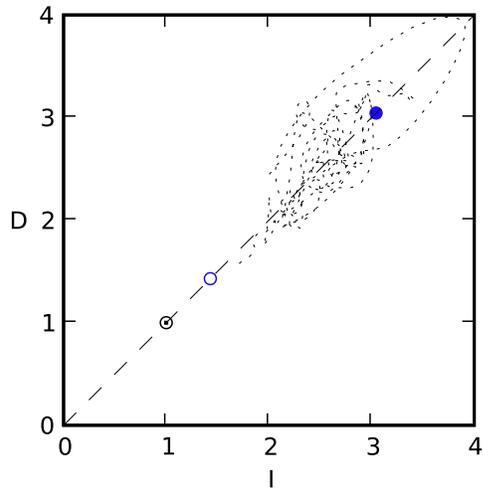
Figure 11: Wall-shear power input I versus viscous dissipation D for an exceptionally long lived, 'turbulent' trajectory in the Ω_{W03} cell (dotted line), as well as the equilibria: $\text{EQ}_1(\circ)$, $\text{EQ}_2(\bullet)$, and $\text{EQ}_0(\odot)$

CHAPTER V

EQUILIBRIA

A key goal of this work is the description of plane Couette flow in terms of invariant solutions. As discussed in sect. C.1, the simplest invariant solutions are equilibria (steady states) or fixed profile time-invariant solutions,

$$\mathbf{u}(\mathbf{x}, t) = \mathbf{u}_{\mathrm{EQ}}(\mathbf{x}), \tag{102}$$

and relative equilibria (traveling waves, rotating waves), characterized by a fixed profile $\mathbf{u}_{\mathrm{TW}}$ moving in the $[x, z]$ plane with constant velocity $\mathbf{c}$,

$$\mathbf{u}(\mathbf{x}, t) = \mathbf{u}_{\mathrm{TW}}(\mathbf{x} - \mathbf{c}t), \qquad \mathbf{c} = (c_x, 0, c_z). \tag{103}$$

Here the suffix EQ or TW labels a particular invariant solution.

One invariant alone does not describe the general behavior of plane Couette flow, but, a description of how equilibria and relative equilibria fit together for various parameter values provides valuable information about the flow. As we have found, the state space of plane Couette flow is a seemingly endless menagerie of such states.

Relative equilibria are not periodic orbits, they are stationary in the velocity $\mathbf{c}$ co-moving frame. Hence we do not describe them by "period T" in which they traverse the cell; instead of saying $\mathrm{TW}_{\pm q}$ is "x traveling with a period of T_q," we characterize it instead by $\mathbf{c}_q = L_x/T_q$.

5.1 Equilibria and Relative Equilibria

In this section we describe all currently known equilibrium and relative equilibrium solutions of plane Couette flow for a range of moderate Re numbers and small aspect-ratio periodic cells Ω. In sects. 5.2 and 5.3 we explore some of their interrelations by tracking them as functions of Re and Ω aspect ratios.

As is clear from Schmiegel's [?] impressive Ph.D. thesis, what follows is almost certainly an incomplete inventory of equilibria; while for any finite Re, finite-aspect ratio cell the number of distinct equilibrium and relative equilibrium solutions may be finite, we know of no way of determining or bounding this number. Schmiegel's [?] catalogue of some 40 equilibrium solutions cannot be compared directly with our results, as Schmiegel's numerical simulations are under-resolved (2,212 dimensions as opposed to 61,506 dimensions typical of numerical work presented here) and for a different size cell (15), but we expect that many of his equilibria can be continued to the fully resolved cell sizes.

However, not all of invariant solutions are of equal importance for understanding turbulent dynamics. As explained in sect. ??, we determine them by initiating searches within the state-space concentrations of natural measure of the 'turbulent' flow, thus favoring discovery of the dynamically important equilibria.

With exception of Nagata [?] 'lower' EQ_1 (or $\mathbf{u}_{\mathrm{LB}}$) and 'upper branch' EQ_2 (or $\mathbf{u}_{\mathrm{UB}}$) equilibria, the Gibson *et al.* [?] 'newbie' EQ_4 (or $\mathbf{u}_{\mathrm{NB}}$) solution, and the Viswanath [?] TW_2 (or $\mathbf{u}_{\mathrm{D1}}$) relative equilibrium, all solutions reported here appear to be new.

We enumerate the solutions EQn in the order we discovered them, with consecutive n indicating lower/upper branch solutions when appropriate. Unless stated otherwise, all calculations are carried out for Re = 400, Ω_{W03} cell. Tables of stability eigenvalues and other properties of these solutions are given in [?], while the images are viewable and full data sets available online at `http://channelflow.org`.

EQ$_1$, EQ$_2$ equilibria. State-space portraits (see figure 10) and bifurcation plots (see figure 17) suggest that the equilibria studied by Nagata [?] and Waleffe [?, ?] form the backbone of the skeleton formed by the invariant state space solutions explored by turbulent dynamics. This pair of solutions, the lower branch EQ$_1$ and the upper branch EQ$_2$, is born together in a low Re saddle-node bifurcation. 'Lower/ upper' refers to their dissipation rates,

$$ D(t) = \frac{1}{V} \int_\Omega d\mathbf{x} \ (\nabla \times \mathbf{u}_{\mathrm{tot}})^2 \ , \tag{104} $$

the idea being that states that dissipate more are somehow 'more turbulent.' (For the laminar flow $D = 1$). For Ω_{W03} cell, this bifurcation occurs at Re $\approx$ 218.5. Close to this value of Re, the two equilibria are connected by a simple EQ$_1 \rightarrow$ EQ$_2$ heteroclinic connection. However, at higher values of Re there appears to be no such simple connection.

The lower branch EQ$_1$ equilibrium, is discussed in detail in ref. [?]. What makes this particular equilibrium so intriguing is that it has a 1-dimensional unstable manifold for a wide range of parameters. Its stable manifold appears to provide a barrier between the basin of attraction of the laminar state and turbulent states [?].

The 'upper branch' EQ$_2$ has an 8-dimensional unstable manifold and a higher dissipation rate than a typical turbulent state. However, within the S-invariant subspace $\mathbb{U}_S$, EQ$_2$ has only one complex unstable eigenvalue pair. The two-dimensional $\mathbb{U}_S$ section of its unstable manifold was explored in some detail in ref. [?]. It appears to bracket the upper end of turbulence in state space, as illustrated by figure 10.

EQ$_3$, EQ$_4$ equilibria. The 'newbie' EQ$_4$ (or $\mathbf{u}_{\mathrm{NB}}$) equilibrium of ref. [?] is the 'upper branch' of this pair (see figure 17). Within $\mathbb{U}_S$, the leading unstable complex eigenvalue pair section of the unstable manifold connects EQ$_4 \rightarrow$ EQ$_1$ heteroclinically. As shown in ref. [?], depending on where a trajectory is on this 2-dimensional EQ$_4$ unstable manifold, it is either chaperoned by the 1-dimensional unstable manifold of EQ$_1$ down to the laminar state, or shoots up into the 'turbulent' region of state space. Statistically (see sect. ??) EQ$_4$ plays a prominent role, and can be seen as a gatekeeper between laminar basin of attraction and the turbulent state space region.

EQ$_5$, EQ$_6$ equilibria. The EQ$_5$ equilibrium was found by searching along a particularly long lived turbulent trajectory, initiated from EQ$_4$. So, naturally it appears to lie close to the transiently turbulent region of state space for Ω_{W03} cell (see figure 14 (a) and table 13).

Its partner EQ$_6$, was found by following EQ$_5$ backwards in Re (see sect. 5.2). We were only able to continue up to $Re = 330$, at this value it is highly unstable (with a 19 dimensional unstable manifold), and it is far more dissipative than typical turbulent trajectories.

EQ$_7$, EQ$_8$ equilibria. EQ$_7$ and EQ$_8$ are S symmetric, and appear together in a saddle node bifurcation in Re (see sect. 5.2). They appear to be equivalent to the σ and ρ solutions
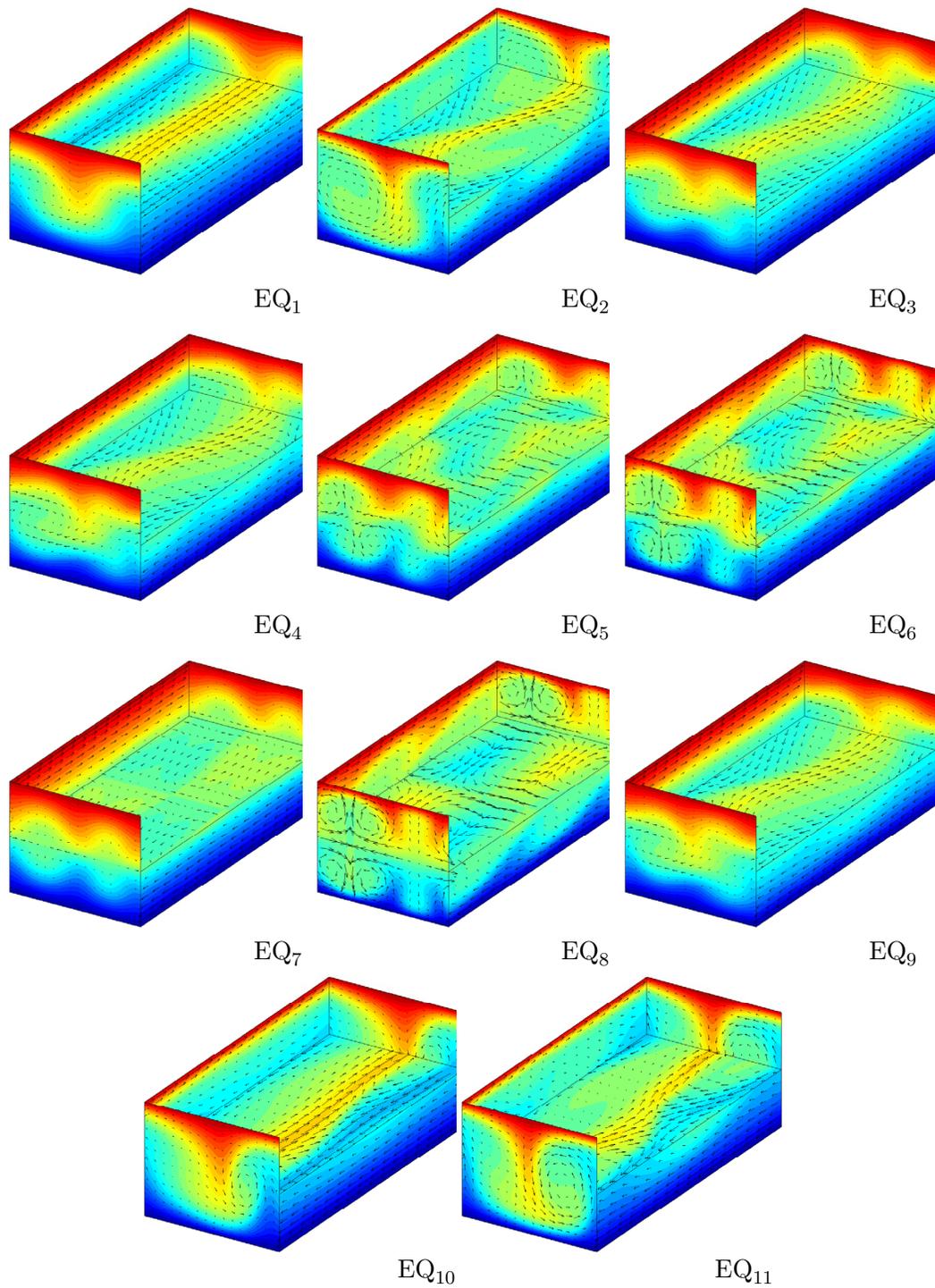
Figure 12: (a)-(i) Equilibria EQ_1 – EQ_{11} in Ω_{W03} cell. $Re = 400$ except for (f) EQ_6, $Re = 330$, and (i) EQ_8, $Re = 270$.
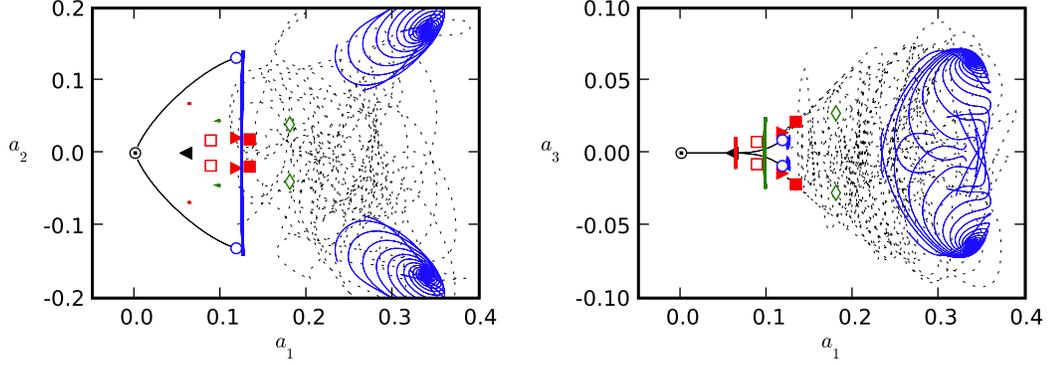
Figure 13: 2-dimensional $[a_1, a_2]$, $[a_1, a_3]$ projections of the 3-dimensional state space portrait of figure 10 illustrate the symmetries of equilibria (○) EQ_1, (●) EQ_2, (□) EQ_3, (■) EQ_4, (◇) EQ_5, (◁) EQ_7, (▶) EQ_9 and relative equilibria TW_2, TW_2, TW_3. Thin black lines are the $EQ_1 \to EQ_0$ heteroclinic connection ('descent side' of the EQ_1 unstable manifold) and its half-cell translations. Streamwise relative equilibria TW_2, TW_3 and their counter-traveling partners are plotted as red/green dots (left panel), and traced in red/green (right panel). Similarly, the spanwise relative equilibrium TW_2 and its counter-traveling partner are traced in blue (left), and plotted as blue dots (right). The cloud of green dots is generated by equal time steps along a long lived turbulent transient, giving an indication of the approximate invariant manifold of chaotic/turbulent fluid states. Finally, the outermost blue spirals are the S-invariant portion of EQ_2's unstable manifold.
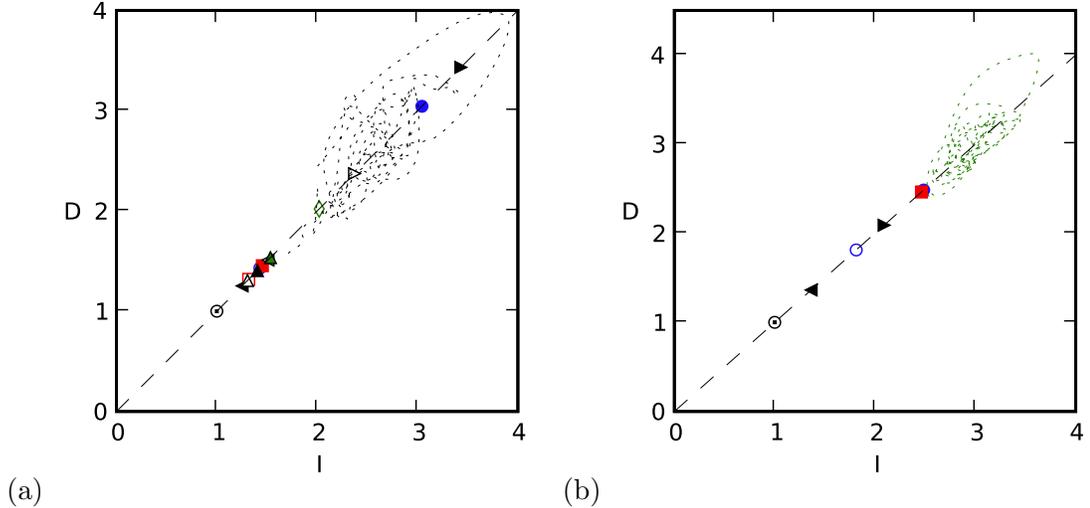
Figure 14: Rate of energy input at the walls, I, versus dissipation D, for the known equilibria and relative equilibria in (a) Ω_{W03} (b) Ω_{HKW} cell at $Re = 400$. The symbols are the same as in figure 10.
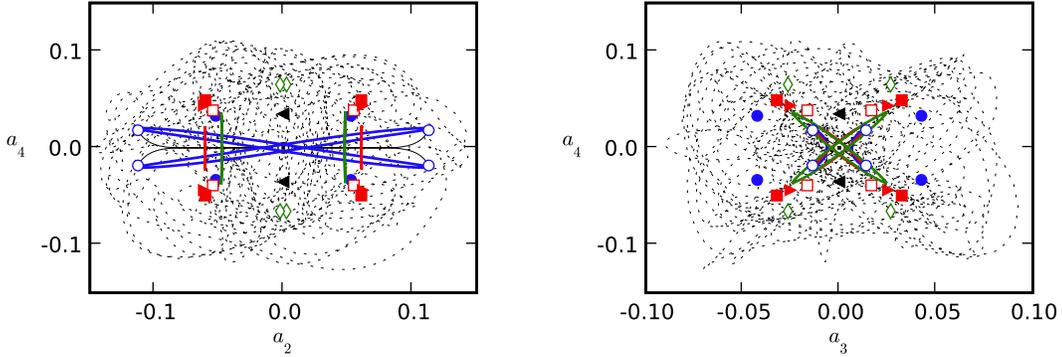
Figure 15: EQ_4-translational basis (101) state spaceportraits, chosen to display the relative equilibria. Symbols are the same as in figure 13. The axes are labeled a_1-a_4, to correspond to the projections onto the vectors defined by (101), as applied to EQ_4.

from [**?**], where they appear to be the outer envelope of the other equilibria discovered there. They are unique among the other equilibria discussed here in that they are also symmetric under τ_{xz}, as well as σ_2, This generates a symmetry group twice as large as S.

EQ_8 does not exist for $Re = 400$, but EQ_7 does. EQ_7 is both the closest state to laminar in terms of disturbance energy and the lowest in terms of drag. Also it has an unstable manifold which is nearly $1D$ in the full space, and is $1D$ in the S-symmetric subspace. In that case, it could possibly play a role equally import to $\mathbf{u}_{EQ1}$. Visually it appears quite similar to EQ_3.

EQ_9 equilibrium. EQ_9 is a single lopsided roll-streak pair with s_3 symmetry (but neither s_1 nor s_2). It is produced by a pitchfork bifurcation off of EQ_4 at $Re \approx 370$ as an $\{s_1, s_2\}$-antisymmetric eigenfunction goes through marginal stability. Thus, it belongs to the S_3-invariant subspace $\mathbb{U}_{S3}$, see (57). So far, it is the only equilibrium, that we have produced as a pitchfork, but from the changes in stability of the other equilibria, it appears that there are many more like it.

EQ_{10}, EQ_{11} equilibria. The EQ_{10}/ EQ_{11} pair belongs to the S_3-invariant subspace. They are produced in a saddle-node bifurcation together with EQ_{10} being the lower branch. They both sit very close to the center of mass of the turbulent regime in this regime (see figure 14 (a)). By eye, they also look very similar to what a typical "turbulent" state looks like for this cell size. However, they are both highly unstable, so are unlikely to be visited too closely by a random orbit.

Relative Equilibria:

The first two relative equilibria solutions reported in the literature were found by Nagata [**?**] by continuing EQ_1 equilibrium to a combined Couette / Poiseuille channel flow, and then continuing back to plane Couette flow. The result was a pair of streamwise relative equilibria arising from a saddle-node bifurcation. As we had no access to data sets for these solutions, we were not able to continue them to Ω_{W03} cell and do not know whether they are related to any of the three relative equilibrium solutions reported below.

<div align="center">TW$_1$ TW$_2$ TW$_3$</div>
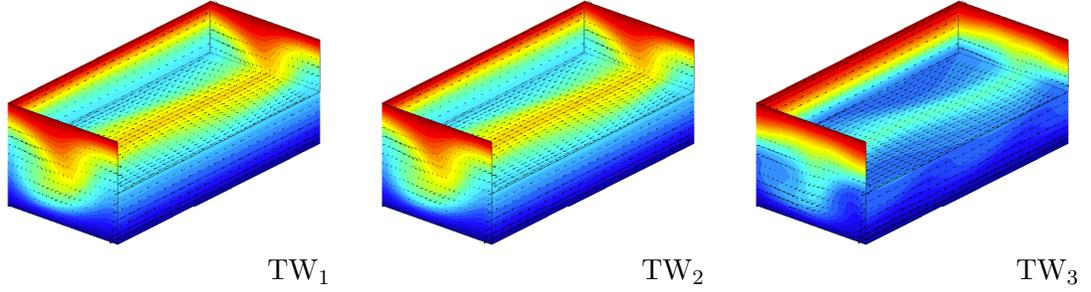
Figure 16: Spanwise TW$_1$, streamwise TW$_2$ and TW$_3$ relative equilibria in Ω_{W03} cell, $Re = 400$.

TW$_1$ relative equilibrium. TW$_1$ is s_2-invariant and hence *spanwise*-traveling, (no streamwise traveling component). At $Re = 400$ its velocity is extremely small, $(c_x, c_z) = (0, 0.00655)$. It was found as a pitchfork bifurcation from EQ$_1$, and thus sits very close to it in state space. It is quite stable, nearly as stable as EQ$_1$, with a $3D$ unstable manifold which is nearly $1D$ thanks to two of its eigenvalues being extremely close to marginal.

TW$_2$ relative equilibrium. Viswanath [**?**] TW$_2$ (or $\mathbf{u}_{\text{D1}}$) is a streamwise traveling, low dissipation rate solution. We verified Viswanath's data set and continued the solution to Ω_{W03} cell for comparison with the other relative equilibria. In this cell it is fairly stable, with an eigenspectrum analogous to that of TW$_1$, with the major difference being that it has a different symmetry.

TW$_3$ relative equilibrium. Also an s_1-symmetric, streamwise relative equilibrium with a relatively high wave velocity $(c_x, c_z) = (0.465, 0)$. Its dissipation rate and energy norm are close to those of TW$_1$.

The relative equilibria are plotted in physical space in figure 5.1 and in state space in figure 15. Their kinetic energies and dissipation rates are tabulated in sect. A.3.

5.2 *Bifurcations under Variation of Re*

As is clear from the global state space portraits such as figure 15, various equilibria and relative equilibria are grouped into interrelated families. Tracking how these solutions behave under of Re and cell size variations provides valuable information about these interrelations and the origins of turbulence in such moderate Re flows.

Figure 17 shows a bifurcation diagram for equilibria and relative equilibria in the Ω_{W03} cell, with dissipation rate $D(Re)$ from (104) plotted against Re as the bifurcation parameter. The normalization of D is chosen so that $D = 1$ for the laminar flow at any Re. The figures shows a superposition of number of different solutions. Unless noted otherwise, the intersections of the solution curves *do not* represent bifurcations.

The first saddle-node bifurcation gives birth to the Nagata [**?**] lower branch EQ$_1$ and upper branch EQ$_2$ equilibria, at Re ≈ 218.5. Both EQ$_1$ and EQ$_2$ lie within $\mathbb{U}_S$; that is, they are symmetric with respect to the s_1, s_2, s_3 symmetries defined in (54). EQ$_1$ has a single unstable eigenvalue with the same symmetries. Shortly after bifurcation, EQ$_2$ has an unstable complex pair within $\mathbb{U}_S$ and two unstable real eigenvalues, with s_3 symmetry, s_1, s_2 antisymmetry, and s_2 symmetry, s_1, s_3 antisymmetry respectively. As indicated by

<div align="center">42</div>
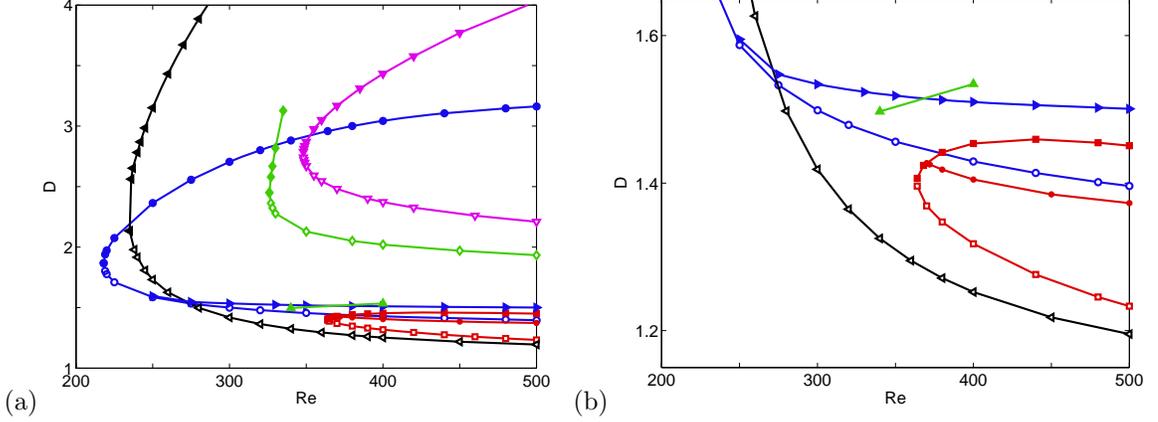
Figure 17: (a) Dissipation rate (104) as a function of Reynolds number for all equilibria and relative equilibria discussed here, Ω_{w03} cell. $\circ$ EQ$_1$, $\bullet$ EQ$_2$, $\square$ EQ$_3$, $\blacksquare$ EQ$_4$, $\diamond$ EQ$_5$, $\blacklozenge$ EQ$_6$, $\triangleleft$ EQ$_7$, $\blacktriangleleft$ EQ$_8$, $\blacktriangleright$ EQ$_9$, $\triangledown$ EQ$_{10}$, and $\blacktriangledown$ EQ$_{11}$, (b) Detail of (a).

the gentle slopes of their bifurcation curves, the [**?**] solutions are very robust with respect to Reynolds number. The lower branch solution has been continued to $Re = 10,000$; it has a single unstable eigenvalue in all this range [**?**].

Further saddle-node bifurcations occur for EQ$_7$, EQ$_8$ at $Re \approx 235$; EQ$_5$, EQ$_6$ at $Re \approx 326$; EQ$_{10}$, EQ$_{11}$ at $Re \approx 348$; and EQ$_3$, EQ$_4$ at $Re \approx 364$. All of these equilibria lie within $\mathbb{U}_S$, except for EQ$_{10}$, EQ$_{11}$ which lie within $\mathbb{U}_{S3}$.

By continuing EQ$_3$ and EQ$_4$ to lower Re, we determined that the two equilibria are born together in a saddle-node bifurcation, with EQ$_3$ playing the role of the 'lower branch.' Its leading unstable complex eigeinvalue pair lies within $\mathbb{U}_S$. The remaining two unstable eigen-directions are nearly marginal, and not within $\mathbb{U}_S$.

EQ$_6$ was discovered by continuing EQ$_5$ backwards in Re. We were not able to continue it back up to 400. At $Re = 330$, it has a nearly marginal stable pair of eigenvalues which are fully symmetric under all discrete and continuous symmetries of plane Couette flow, ruling out a bifurcation to traveling waves along these modes. In a neighborhood of what was EQ$_6$ for lower Re, the dynamics for $Re > 330$ appear to be roughly periodic, suggesting that EQ$_6$ undergoes a supercritical Hopf bifurcation here. At $Re \approx 348$, EQ$_{10}$ and EQ$_{11}$ are born in a saddle node bifurcation, similar in character to the EQ$_1$ / EQ$_2$ bifurcation.

Figure 17(b) shows several symmetry-breaking bifurcations. At $Re \approx 250$, TW$_1$ bifurcates from EQ$_1$ in a subcritical pitchfork as a s_2 symmetric, s_1, s_3 antisymmetric eigenfunction of EQ$_1$ becomes unstable, resulting in a spanwise-moving relative equilibrium. At $Re \approx 370$, the EQ$_9 \in \mathbb{U}_{S3}$ equilibrium bifurcates off EQ$_4$ along an s_3 symmetric, s_1, s_2 antisymmetric eigenfunction of EQ$_4$. As explained in sect. C.1, s_3 changes the sign of all components of $\mathbf{u}$ and $\mathbf{x}$, and thus fixes the phase of s_3 symmetric fields in both x and z. Thus the EQ$_9$ that bifurcates off EQ$_4$ along this S_3-symmetric eigenfunction is an equilibrium rather than a relative equilibrium.

5.3 Bifurcations under Variation of Spanwise Width

Up until this point, we have discussed invariant solutions for the Ω_{w03} cell. Now we turn our attention to how things change as the spanwise cell width L_z is varied. The dissipation as a function of L_z is plotted in figure 18.

43
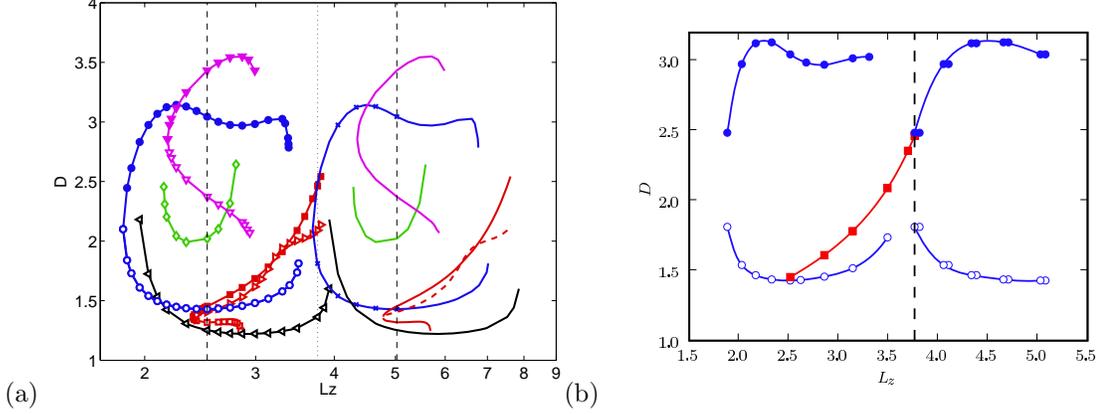
Figure 18: Dissipation rate D of most equilibria and relative equilibria discussed here for family of cells $\Omega(L_z) = [2\pi/1.14, 2, L_z]$ as function of the spanwise cell width L_z. The Ω_{W03} cell is at $L_z = 2.51$, and the vertical dashed line marks the Ω_{HKW} cell at $L_z = 3.76$. ($\circ$) EQ_1, ($\bullet$) EQ_2, ($\square$) EQ_3, ($\blacksquare$) EQ_4, ($\diamond$) EQ_5, ($\blacklozenge$) EQ_6, ($\triangleleft$) EQ_7, ($\blacktriangleleft$) EQ_8, ($\blacktriangleright$) EQ_9, ($\triangledown$) EQ_{10}, ($\blacktriangledown$) EQ_{11}, ($\triangleleft$) TW_1, ($\triangle$) TW_2, and ($\blacktriangle$) TW_3. Spanwise doubled states $2 \times \mathrm{EQ}_1$, $2 \times \mathrm{EQ}_2$ (see figure 19) are indicated by doubled markers. Equilibria which we could not continue appreciably far from Ω_{W03} cell width are omitted. The apparent proximity of EQ_4 to $2 \times \mathrm{EQ}_2$ at $L_z = 3.76$ is an artifact of the projection onto D axis - the $\mathbf{u}_{\mathrm{EQ4}}$ and $2 \times \mathbf{u}_{\mathrm{EQ2}}$ $3D$ profiles are distinct.

In particular, we are interested in connecting the Hamilton *et al.* [?] Ω_{HKW} cell, empirically determined to be the smallest cell $\Omega(Re)$ which appears to exhibit sustained turbulence, Ω_{W03} cell studied up to this point, which is shorter in the spanwise direction and exhibit transient turbulence for $Re = 400$.

Of the equilibria discussed above, EQ_4 EQ_7, and EQ_9 are the only ones that we could continue from Ω_{W03} cell to the Ω_{HKW} cell at $Re = 400$. The others equilibria terminate in saddle-node bifurcations, or bifurcate into pairs of relative equilibria in pitchfork bifurcations.

In the Ω_{HKW} cell EQ_4 is *extremely* unstable, with a 39 dimensional unstable manifold. In physical space it has 4 distinct streaks, see figure 19. Many of its eigenvectors appear not just as complex pairs, but as pairs of complex pairs (see [?]) – that is to say, they have algebraic multiplicity 2.

The cell is periodic in z, so a solution EQ which exists for cell of width L_z' is also a solution $m \times \mathrm{EQ}$ m-times repeated for a a cell of width $L_z = mL_z'$, but with more unstable eigen-directions. In particular, some of the equilibria for the cell with double spanwise width of Ω_{W03} cell are the equilibria of the Ω_{W03} cell repeated twice. We find that the $2 \times \mathrm{EQ}_1$ and $2 \times \mathrm{EQ}_2$ can be continued to the Ω_{HKW} cell. As s_i operations (53) include half-cell translations, the doubled solutions are s_1 but not s_2 or s_3 invariant. Instead their symmetries are generated by $[s_1, \sigma_3\tau_{z/4}]$, where $\tau_{z/4}$ is a quarter-cell translation in L_z. These equilibria are plotted in physical space in figure 19.

From a plot of I versus D (figure 14 (b)), the equilibria that we have in Ω_{HKW}, do not seem to be very closely related to the turbulent attractor for these parameters. At best, they seem to set a lower bound for it. However, this should not be taken to mean that there are no equilibria in the attractor – only that the few that have been continued there are outside it. A more exhaustive search would probably turn up more.

EQ$_4$ 2 × EQ$_1$ 2 × EQ$_2$

EQ$_7$ EQ9

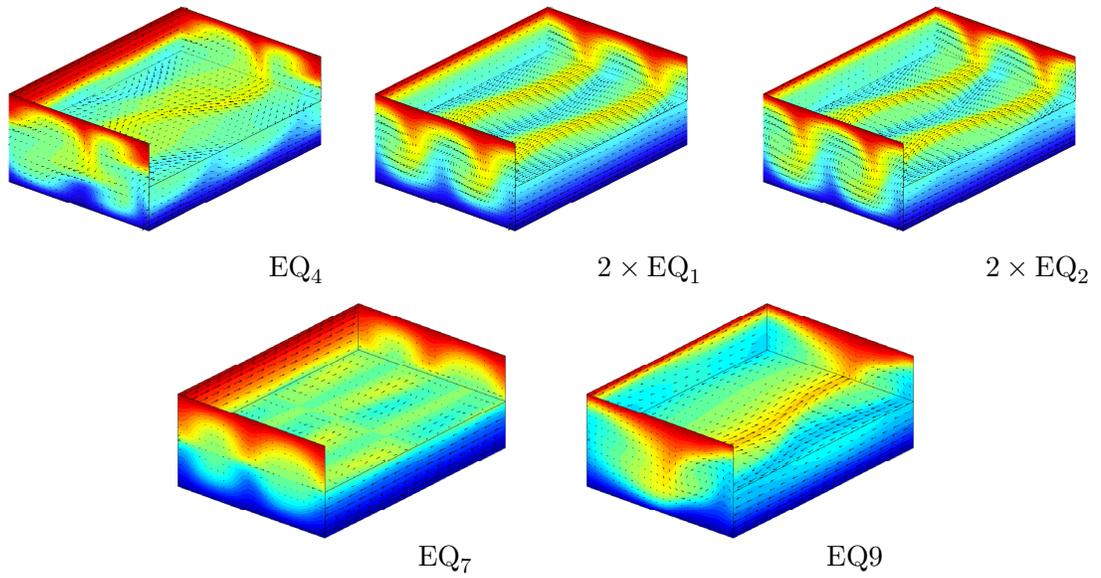**Figure 19:** EQ$_4$, EQ$_7$, EQ$_9$ equilibrium and the spanwise doubled equilibrium solutions $2 \times EQ_1$, $2 \times EQ_2$ for the Ω_{HKW} cell, $Re = 400$.

CHAPTER VI

HETEROCLINIC CONNECTIONS

A heteroclinic connection is an orbit in a dynamical system which starts infinitesimally close to one equilibrium (the source) and terminates at a different equilibrium(the sink). In general high dimensional dynamical systems, they are quite uncommon. So, it is quite surprising that we have uncovered 4 of them in plane Couette flow.

One mechanism by which robust cycles of heteroclinic connections can be created is through symmetry [**?**, **?**]. If two equilibria have axial isotropy groups which share a common subgroup which is $\mathbb{C}$-axial, then they can have a robust connection. Given a sequence of such isotropy groups, one can have robust heteroclinic connections. In fact, the connection can be robust as long as one is a sink and the other is a saddle in the common fixed point subspace of the common isotropy group. This may be the case for Taylor-Couette flow, where heteroclinic connections are suspected to exist [**?**]. However, it is not entirely clear whether or not this is the case for these equilibria.

Symmetry does come into play by significantly restricting the search space for equilibrium. By only considering instabilities of equilibria which are in $\mathbb{U}_S$, we limit the dimension of the search space around the source equilibria to a number which is typically less than 3. It also restricts the sink equilibrium. Normally, we would have to seek any connection to the whole torus of states which are equivalent to the sink equilibrium up to translation. The symmetry restriction reduces this continuous infinity to just 4 isolated points.

A necessary condition for the robustness of heteroclinic connections is that the sum of the dimension of the unstable manifold of the source and the codimension of the unstable manifold of the sink is greater than or equal to the full dimension of the space [**?**]. This is the case for all but one of the heteroclinic connections.

Everything that follows pertains to Ω_{W03} unless otherwise specified.

6.1 Three Heteroclinic Connections for Re=400

As discussed in chapter 5, EQ_1 has an unstable manifold which is codimension 1, thus its center and stable manifolds form a locally impassible barrier between the laminar state and turbulence. Remarkably, we found that 3 of the previously discussed equilibria have heteroclinic connections to it: EQ_4, EQ_3, and EQ_5. Then these equilibria live on this barrier which is the stable manifold of EQ_1. This allows us to start to chart the extent of the barrier.

6.1.1 A Heteroclinic Connection from EQ_4 to EQ_1

As it approaches EQ_1, the unstable manifold of EQ_4 separates along the two branches of that of EQ_1. A single trajectory, the heteroclinic connection, straddles that split. This is plotted in a state space portrait in figure 20.

The dimension set of heteroclinic connection candidate trajectories emerging from the neighborhood of $\mathbf{u}_{\mathrm{EQ4}}$ is two, due to its by the complex instability (or three if $\lambda_{\mathrm{NB}}^{(3)}$ is considered as well). The dimensionality of state space near the target EQ_1 is effectively reduced to one by its codimension-1 set of stable eigenvalues.
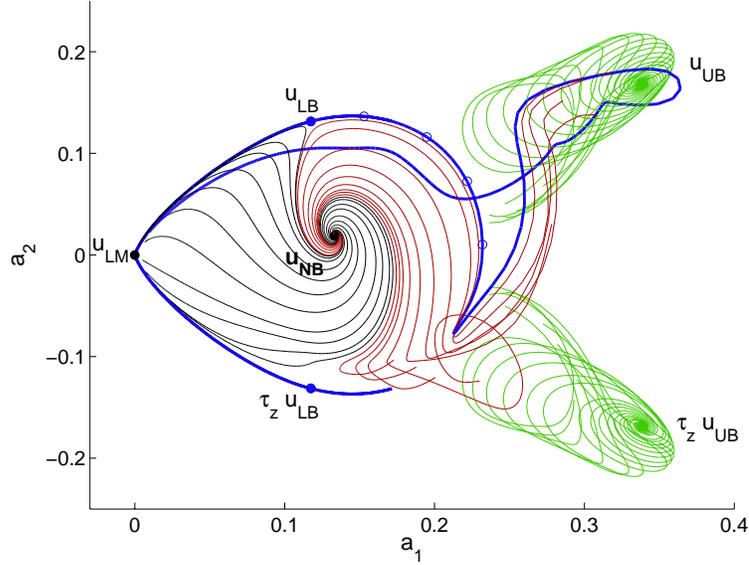
Figure 20: EQ$_2$ translational state space portrait of the EQ$_4 \to$ EQ$_1$ connection, with their unstable manifolds plotted as well. EQ$_2$ is also plotted to give a reference for the region which corresponds to turbulence. a_1, a_2 are the projections onto the $\mathbf{e}_1, \mathbf{e}_2$ vectors as defined by (101) for EQ$_2$.

Note also that most weakly stable eigenvalues of EQ$_1$, $\lambda_{\text{LB}}^{(4)}$ through $\lambda_{\text{LB}}^{(8)}$, are outside the $\mathbb{U}_S$ subspace, so trajectories in EQ$_4$'s unstable manifold are forced to approach EQ$_1$ along the more strongly contracting eigendirections of $\lambda_{\text{LB}}^{(9)}$ and $\lambda_{\text{LB}}^{(10)}$ (table 2).

The heteroclinic connection from EQ$_4$ to EQ$_1$ forms a boundary between trajectories that decay immediately to laminar flow and those that grow towards transient turbulence. Those that pass near EQ$_1$ and grow to turbulence follow the unstable manifold of EQ$_1$ into a region near the EQ$_2$ equilibrium. Given that EQ$_1$'s stable manifold forms the basin boundary for the laminar state, this heteroclinic connection indicates that we can extend it to include the stable manifold of EQ$_4$ as well.

6.1.2 Heteroclinic Connections from EQ$_3$ and EQ$_5$ to EQ$_1$

The situation with EQ$_3$(the lower branch bifurcation partner of EQ$_4$) and EQ$_5$ is quite similar to that of EQ$_4$. The S-symmetric subspace of the unstable manifold of EQ$_3$ is 3 dimensional rather than 2, however, it is dominated by a complex instability. Focusing only on that mode, we were able to locate another heteroclinic connection, EQ$_3$ to EQ$_1$.

EQ$_5$ is interesting because it sits nearly in the center of the region of state space identified with "turbulence." However, it too is connected to EQ$_1$, meaning that it is also part of the laminar-turbulent boundary. Like some of the other equilibria, its linear stability is dominated by a symmetric, complex instability. It also possesses a second symmetric instability which was ignored in the search for a heteroclinic connection. Applying the same methods as before, we obtained a heteroclinic connection to EQ$_1$ associated with this leading instability.

Figure 21 is a state space portrait of equilibria and heteroclinic connections in the projection of ∞-dimensional state space onto 3 basis vectors in the S-invariant subspace

47
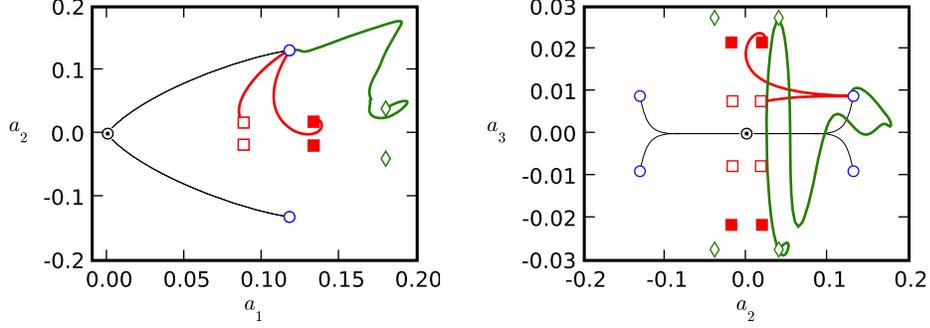
Figure 21: State space portrait of heteroclinic connections going from several known equilibria to $EQ_1(\circ)$. The thin black lines are the half of unstable manifold of EQ_1 which immediately decays to laminar $(\odot)$ and its half-cell translations. The other lines are the connections: $EQ_4 \rightarrow EQ_1(\blacksquare \rightarrow \circ)$, $EQ_3 \rightarrow EQ_1(\square \rightarrow \circ)$, and $EQ_5 \rightarrow EQ_1(\diamond \rightarrow \circ)$. The streamwise and spanwise translations of the equilibria are also plotted, but for clarity, the heteroclinic connections from those states are not. The a_1 coordinate is symmetric under τ_x and τ_z, while a_2 is antisymmetric under τ_z and symmetric under τ_x, and a_3 is antisymmetric under τ_x and symmetric under τ_z. Ω_{W03} at $Re = 400$.

introduced in ref. [**?**].

As before with EQ_4, these new heteroclinic connections allow us to identify even more structure of the stable manifold of EQ_1, and thus the basin boundary for laminar flow. Their existence implies that there is a complex web formed by the stable and unstable manifolds of equilibria that paritions the laminar attracted basin from turbulence.

6.2 Heteroclinic Connection from EQ_1 to EQ_2 at $Re = 225$

Tracking the bifurcation of EQ_1 and EQ_2, we discovered another heteroclinic connection $EQ_1 \rightarrow EQ_2$. It exists from the bifurcation EQ_1 - EQ_2 bifurcation at $Re \approx 218$ and is not broken until around $Re = 250$. In this range of Re, EQ_2 and EQ_1 each have three-dimensional unstable manifolds. Restricting our attention to the symmetric subspace, $\mathbb{U}_S$, EQ_1 has a $1D$ unstable manifold which corresponds to its most unstable direction, and EQ_2's is $2D$. This is particularly surprising since it does not meet the criterion for robustness based on dimension.

Another consequence of this is that there is no need to 'search' for an heteroclinic connection. Since the unstable manifold of EQ_1 is effectively $1D$, the 'search' in this case simply involves checking whether or not EQ_1's $1D$ unstable manifold ended at EQ_2 or not.

For the values of Re considered here, EQ_1's stable manifold splits its neighborhood in state space into two halves. One side monotonically decays to the laminar state, which is typical for EQ_1. But we find that for $Re < 250$, the other half, W_{LB}^{u+}, is a heteroclinic connection to EQ_2.

Understanding exactly what happens to the heteroclinic connection as Re is increased requires further study. It appears that there is a global bifurcation in the $Re \in [225, 250]$ range. This could help point the way to a the route to chaos in plane Couette flow, much as similar heteroclinic bifurcations herald the onset of chaos in Lorenz [**?**].

CHAPTER VII

SPECULATION AND FUTURE WORK

As shown in Chapters 5 and 6, the state space of plane Couette flow is rife with dynamical invariants. Here we speculate about what this says about the structure of plane Couette flow state space. In the course of this discussion, several new avenues of research are suggested.

7.1 Turbulence as a walk about exact coherent states

The turbulent attractor is filled with a myriad of equilibria and relative equilibria. These states are roughly split into two groups, the lower drag, 'lower branch' states and their higher drag counterparts, the 'upper branch' states. The lower branch states seem to cluster around EQ_1, and provide a barrier to laminarization.

The backbone of this barrier is formed by the stable manifold of EQ_1. Being codimension 1, it partitions the neighborhood of EQ_1 into two parts: the laminar side and the turbulent side. The two sides are identified by the time it takes each half the EQ_1's unstable manifold to approach the laminar state. One side takes a rather direct route, monotonically approaching EQ_0. The one side stands in stark contrast to this. At low values of Re, it never laminarizes – being heteroclinically connected to EQ_2. As Re is increased, the system undergoes a global bifurcation, breaking the heteroclinic connection. For higher Re, this orbit spends longer and longer time exploring the turbulent region of state space – the inertial manifold envisioned by Hopf [**?**].

As we widen our pinhole view of state space to include more equilibria, the picture becomes richer. There are several equilibria which are connected to EQ_1. This allows us to see how the stable manifold of EQ_1 extends further out into state space. The heteroclinic connections show exactly where the stable manifold of EQ_1 intersects the unstable manifold of these equilibria. For example, EQ_4 has a single complex instability. This plane is split by a heteroclinic connection to EQ_1. Orbits near the heteroclinic connection approach EQ_1, then laminarize or become more turbulent depending on which side of the stable manifold of EQ_1 that they approach. Figure 22 depicts this splitting.

Based on this figure, roughly half of the orbits which visit the neighborhood of EQ_4 laminarize immediately, while the other half are kicked back towards turbulence. The heteroclinic connection here straddles one of these tipping points. The fulcrum of the other is not so clear. Orbits in that neighborhood appear to make a relatively close pass to $\tau_x EQ_1$, but attempts to nail down an heteroclinic connection have been unsuccessful so far.

It is possible that a relatively stable periodic orbit straddles this splitting. After some time, we see from figure 23 that these orbits are nearly periodic, making repeated visits to the neighborhood of $\tau_x EQ_1$ and $\tau_{xz} EQ_1$.

This view suggests that state space could be partitioned by the stable and unstable manifolds of the equilibria. Evolution in time could be replaced by a walk on a Markov graph, where each node corresponds to an equilibrium. The heteroclinic connections indicate how to allocate edges on this graph. How such Markov graph might look like is illustrated by figure 24.

This sketch is meant to imply that turbulence in plane Couette flow is transient. This
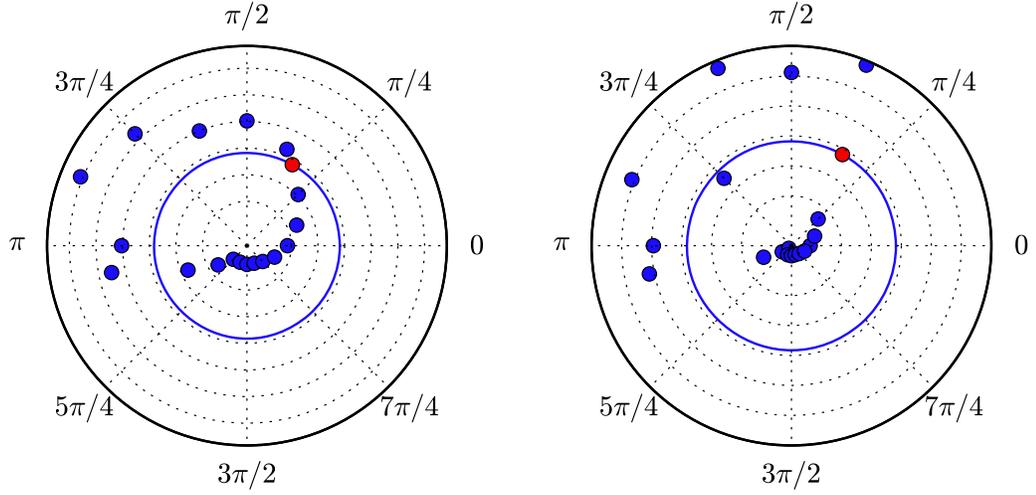
Figure 22: Several trajectories were seeded at a distance of 0.0003 around EQ_4 in the plane corresponding to its leading complex instability. In this plot the polar angle corresponds to the initial phase, and the radius is the distance to the laminar state, after 275 time units (left) and after 340 time units (right). The red point corresponds to the EQ_4 to EQ_1 connection, and the blue circle corresponds to the distance of EQ_1 from laminar.
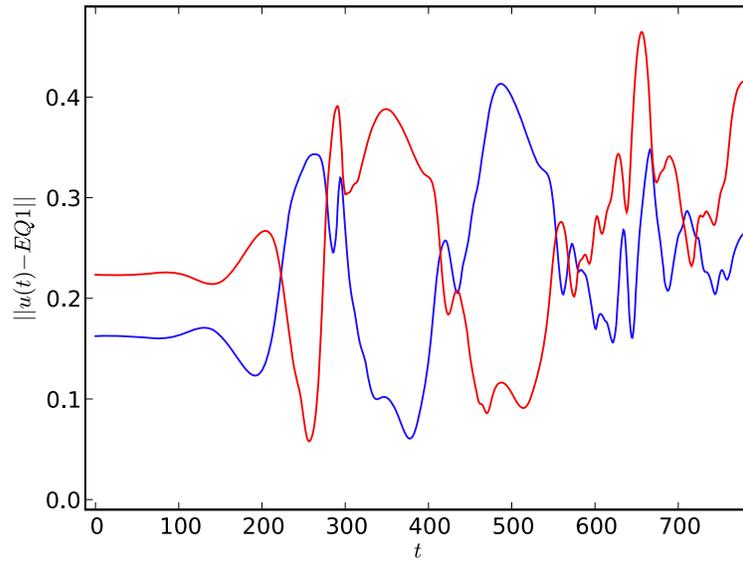
Figure 23: The distance to $\tau_x EQ_1$ (blue) and $\tau_{xz} EQ_1$ (red), as a function of time, on an orbit initiated near the laminar-turbulence split in the unstable manifold of EQ_4.
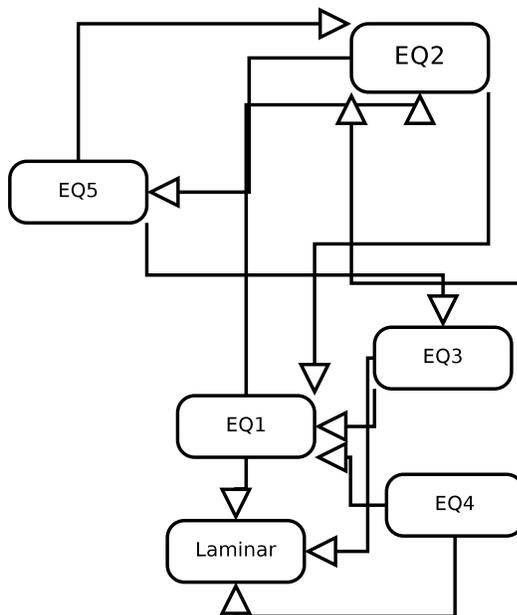
Figure 24: A sketch of what a coarse partitioning Markov graph based on unstable-stable manifolds connections might look like for plane Couette flow.

view is supported by both experimental and numerical studies [**?**]. EQ_1 has been continued to $Re = 10000$ [**?**], and likely could be continued to even higher values Re. Even in this regime, EQ_1, still has a $1d$ unstable manifold, and thus could still possibly be considered to act as laminar-turbulent fulcrum.

The heteroclinic connections computed here highlight a path to linearization. They sit at on the edge of a 'hole' in the unstable manifolds of the source equilibria. If a turbulent trajectory falls inside this hole it laminarizes. Supporting evidence of the transience of turbulence in plane Couette flow could be found by tracking these heteroclinic connections to higher Re, to see if they are persistent as well as to see if the size of this hole decreases. If this view is correct, the decrease in the size of this hole should correlate with the rate of laminarization.

These new equilibria and heteroclinic connections are useful for describing the skeleton of state space, but the major piece missing from this picture is the periodic orbit musculature to go around it. Initial guesses for periodic orbits are hard to come by. But, construction of a Markov partition of state space would give us the joints of state space, around which we can thread periodic orbits. Once we obtain a number of these, the trace formula [**?**] can be used to compute long time averages of the flow, or in the case that it is a repeller, it gives us a means to compute its escape rate – the rate of laminarization.

7.2   Refinement of Heteroclinic Connections

One way of improving a Markov partition of state space would be to find more heteroclinic connections. The method used in this thesis to compute heteroclinic connections is rather naive, making their computations unnecessarily expensive. There are several ways in which this situation can be improved. One major inefficiency of the algorithm presented here is

that it does not make use of linearization around the target equilibrium. In the algorithm presented here, this is done for the source equilibrium, but it is more complicated to do for the target. A heteroclinic connection is an infinite time object, so computing its entire extent as it approaches an unstable equilibrium is impossible. However, if we make use of the linear stability of the target equilibrium, we can eliminate the calculation of all but a finite segment of the heteroclinic connection.

The idea is that rather then running a time-consuming integration through the neighborhood of the target equilibrium, we can predict how close an approximate heteroclinic connection will get just by its decomposition into a linear combination of the eigenvectors of the equilibrium. In the case of EQ_1, all we would really need to know is the the approximate connection's projection onto EQ_1's $1d$ unstable manifold. Then, rather then seeking the distance of closest approach, we only need to find out how big of a cross section it has in the unstable directions, when it enters the neighborhood of EQ_1.

To do this, we need to make use of a projection onto the leading eigenvectors of the stability matrix A, for the target equilibrium. The eigenvectors are generally not mutually orthogonal. This makes the expression of a particular point in phase space in terms of an eigenvector basis somewhat more difficult. Using more eigenvectors in the expansion will change the magnitude of the projection onto the other more unstable eigenvectors. However, our hopes are somewhat buoyed by the fact that all but a few of the eigenvectors will have no contribution, since they are so stable.

Let $\mathbf{x}$ be the location of a point in state space which we want to express in terms of the eigenvectors $\mathbf{e}_i$ of an equilibrium located at the origin. We would like to find c_i which minimize the residual,

$$r = \left\| \mathbf{x} - \sum_{i=0}^{N} c_i \mathbf{e}_i \right\|, \tag{105}$$

or, equivalently, we wish to approximately solve for $\mathbf{c}$ in

$$\mathbf{Mc} = \mathbf{x}, \tag{106}$$

where the columns of $\mathbf{M}$ are formed by the eigenvectors $\mathbf{e}_i$.

One approach is to compute the Moore-Penrose pseudoinverse, $\mathbf{M}^+$. Pseudoinverse is a matrix which satisfies $\mathbf{M}^+\mathbf{M} = \mathbf{1}$, and solves (106) in a least-squares sense. If compute the singular value decomposition of $\mathbf{M}$, $\mathbf{M} = \mathbf{U\Sigma V}^*$, then $\mathbf{M}^+ = \mathbf{V\Sigma}^+\mathbf{U}^*$, where the elements of $\mathbf{\Sigma}^+$ are the reciprocal elements of the nonzero entries of $\mathbf{\Sigma}$ (or zero otherwise).

Hopefully, by implementing this idea, the accuracy of the heteroclinic connections already computed here can be improved and new heteroclinic connections can be found. If Schmiegel's thesis [**?**] is any indication, there's plenty where those came from.

7.3 For the Experimentalist

Results of this thesis suggest a few avenues of exploration for experimentalists as well. Stereoscopic Particle Image Velocimetry (PIV) allows the reconstruction of a slice of a velocity field. These experiments fall into two categories: turbulence suppression and observation of turbulence.

Lower branch type states such as EQ_3 and EQ_7 seem particularly important in terms of turbulence suppression. Their relative proximity to laminar in state space (see sect. A.3) could make them excellent targets as gateways between turbulence and laminar flow. By

inputting the relative small amount of energy needed to reach EQ_7, one could induce turbulence relatively cheaply. Conversely, it also indicates the type of perturbations that would need to be suppressed in order to prevent loss of laminar flow.

To test these ideas, it would be useful to set up an experiment in which states analogous to EQ_7 would be induced. There should be a rather sharp change in turbulent lifetimes as the magnitude of the perturbation is increased. Furthermore, the magnitude of the perturbation needed should prove to be minimal as compared to other types which have been tried in the past.

The idea of turbulence as a walk among coherent states, guided by heteroclinic connections could also be tested experimentally. Experimental observation of the heteroclinic connections may be somewhat impractical due to their extreme sensitivity to small changes in the system. However, it may be possible to examine the results of experiment in light of the Markov partition that they suggest.

In particular, one should observe close passes to EQ_1-type states, with a corresponding slowing in the rate of change of the flow field, followed by eruptions towards EQ_2-type states. If a repertoire of equilibria and their heteroclinic connections were to be computed for the geometry being studied, one could proceed to partition state space, and compare the expected Markov graph, to the experimentally exhibited behavior.

CHAPTER VIII

CONCLUSION

As a turbulent flow evolves, every so often we catch a glimpse of a familiar pattern. For any finite spatial resolution, the flow approximately follows for a finite time a pattern belonging to a finite alphabet of admissible fluid states, represented here by a set of exact coherent states. Turbulent dynamics visualized in state space appears pieced together from close visitations of exact coherent states connected by transient interludes. This is plainly illustrated by figure 3. The larger cell is clearly tesselated by states not dissimilar from those presented here.

For plane Couette flow equilibria, relative equilibria and periodic solutions embody the vision of turbulence [**?**]: a repertoire of recurrent spatio-temporal patterns explored by turbulent dynamics. The new equilibria and relative equilibria that we present here expand and refine this repertoire.

These orbits lend credence to our view of turbulence as a walk through this set of patterns. The heteroclinic connections that we present here are the initial steps in drawing an atlas of plane Couette flow state space; close passages to equilibria form a coarse symbolic dynamics (nodes of a Markov graph), and their heteroclinic connections are the directed links connecting these nodes. The EQ_1 equilibrium, along with the equilibria which connect back to it, appear to form a part of the state space boundary dividing two regions: one laminar the other turbulent. The heteroclinic connections from this edge into turbulence trap the dynamics in the space between lower and upper branch states. These objects provide sign posts in state space which could be used for guiding a turbulent orbit to or away from relaminarization.

The emergence and disappearance of these heteroclinic connections can also be diagnostic. The disappearance of the $EQ_1 \rightarrow EQ_2$ is reminiscent of other global bifurcations occurring in simpler dynamical systems. For instance, in the Lorenz system a series of such bifurcations occur as the Rayleigh number is increased [**?**]. They mark changes in the topology of state space. For plane Couette flow, such bifurcations could be used to mark the onset of turbulence.

Future work in this direction could serve to clarify such points. It is still not entirely clear what happens at the global bifurcations involved in the creation and annihilation of these heteroclinic connections. Furthermore, the list of equilibria and their heteroclinic connections we have found so far should by no means be considered to be exhaustive. Further investigation of plane Couette flow for these as well as other geometries will most likely turn up more equilibria and their heteroclinic connections.

Currently, a taxonomy for all of these myriad states eludes us. To organize these states in a useful way requires a deeper understanding of the connections between them. From this work, we only see how the various states are related for a fixed geometry. It may be that under continuation to other cell aspect ratios we see that EQ_3 bifurcates from EQ_1 for instance, or that their roles switch.

This connects to the outstanding issue of all studies undertaken so far, which must be addressed in future work: the small aspect cell periodicities imposed for computational convenience. So far, all numerical work has focused on spanwise-streamwise periodic cells

barely large enough to allow for sustained turbulence. Such small cells introduce dynamical artifacts such as lack of structural stability, cell-size dependence of the sustained turbulence states, and boundary-condition dependent coherent states unlike those observed in large aspect ratio experiments.

APPENDIX A

EQUILIBRIA DATA

In this chapter, the eigenspectra as well as some important dynamical measures of the equilibria and relative equilibria discussed in here are tabulated. The focus is on the two different cell sizes discussed, $\Omega_{\mathrm{W03}} = [2\pi/1.14, 2, 2\pi/2.5]$, and $\Omega_{\mathrm{HKW}} = [2\pi/1.14, 2, 2\pi/1.67]$, for $Re = 400$. The spectra of the states Ω_{W03} are listed in sect. A.1, and those of the Ω_{HKW} states are in sect. A.2. Some dynamic measures of these states are discussed in sect. A.3.

It is important to note here that the choice of an external pressure or mean-velocity constraint that governs the evolution of the mean flow. We hold the spatial mean of the pressure gradient fixed at zero and let the mean velocity vary independently. Different boundary conditions can produce significantly different results.

A.1 W03 Cell Equilibria Stability

In this appendix we tabulate the leading eigenvalues of stability matrix of the known equilibria and relative equilibria for Ω_{W03}. If the state exists for $Re = 400$, then that is the Re used. If not, then the table is made use the highest Re for which the state does exist. The symmetry of the eigenfunctions is also noted. S indicates symmetry under the given the given operation, A indicates antisymmetry, and $-$ indicates asymmetry.

As discussed in chapter 3, eigenfunctions of symmetric symmetric equilibria with multiplicity 1 are always either S or A. If an equilibrium is not symmetric with respect to a given symmetry operation, then the symmetry of the eigenfunctions with respect to that operation is omitted.

Table 1: Least stable eigenvalues of the laminar equilibrium $\mathbf{u}_{\mathrm{EQ0}}$ for Ω_{W03} at $Re = 400$, computed by Arnoldi iteration, compared to Stokes (S) and heat-equation (H) eigenvalues from analytic formulas. The eigenvalues are ordered in the table by decreasing real part. All laminar eigenvalues are real.

n	mode	k_y	k_z	Arnoldi $\lambda_{\mathrm{LM}}^{(n)}$	Analytic $\lambda_{\mathrm{LM}}^{(n)}$
1,2	H	1	0	-0.00616850	-0.00616850
3,4	H	1	1	-0.02179322	-0.02179350
5,6	H	2	0	-0.02467398	-0.02467401
7,8	S	-	1	-0.02916371	-0.02916371
9,10	H	2	1	-0.04029896	-0.04029901
11,12	H	3	0	-0.05551652	-0.05551653

Table 2: EQ$_1$ (left) and EQ$_2$ (right) equilibrium stability eigenvalues $\lambda = \mu \pm i\omega$ and symmetries of corresponding eigenvectors at same parameter values. The zero eigenvalues result from the continuous translation symmetry of the flow.

n	$\mu_{\mathrm{EQ}_1}^{(n)}$	$\omega_{\mathrm{EQ}_1}^{(n)}$	$s_1s_2s_3$	n	$\mu_{\mathrm{EQ}_2}^{(n)}$	$\omega_{\mathrm{EQ}_2}^{(n)}$	$s_1s_2s_3$
1	0.0501205		S S S	1	0.0555837		A A S
2	1.878e-06		- - -	2,3	0.0325292	0.107043	S S S
3	-1.625e-06		- - -	4,5	0.0160591	0.039238	S A A
4	-0.0020054		A S A	6,7	0.0152926	0.284177	S A A
5	-0.0065977		A A S	8	0.0106036		A S A
6	-0.0069308		S A A	9	1.032e-06		- - -
7	-0.0097953		S A A	10	1.599e-07		- - -
8	-0.0135925		A S A	11,12	-0.0141215	0.057748	S S S

Table 3: EQ$_3$ (left) and EQ$_4$ (right) equilibrium stability eigenvalues $\lambda = \mu \pm i\omega$ and symmetries of corresponding eigenvectors at same parameter values. The zero eigenvalues result from the continuous translation symmetry of the flow.

n	$\mu_{\mathrm{EQ}_3}^{(n)}$	$\omega_{\mathrm{EQ}_3}^{(n)}$	$s_1s_2s_3$	n	$\mu_{\mathrm{EQ}_4}^{(n)}$	$\omega_{\mathrm{EQ}_4}^{(n)}$	$s_1s_2s_3$
1,2	0.03397837	0.01796294	S S S	1	0.0306497		A S A
3	0.009182156	0	S A A	2,3	0.0261952	0.056377	S S S
4	0.00885971	0	A S A	4	0.0183668		S S S
5	1.392395e-07	0	- - A	5	0.0174064		S A A
6	1.141266e-07	0	- - A	6	0.0158648		A A S
7	-0.003877414	0	A S A	7	-1.047e-07		- - -
8	-0.006542565	0	S A A	8	-4.709e-07		- - -
9	-0.01931146	0	S S S	9	-0.0045203		A S A
10	-0.0224269	0	A A S	10	-0.0048642		S A A

Table 4: Linear stability eigenvalues, $\lambda = \mu \pm \omega$, of EQ$_5$ for $\Omega_{\mathrm{W}03}$ cell, $Re = 400$ (left), and that of EQ$_6$ for $\Omega_{\mathrm{W}03}$ cell, $Re = 330$ (right).

n	$\mu_{\mathrm{EQ}_5}^{(n)}$	$\omega_{\mathrm{EQ}_5}^{(n)}$	$s_1s_2s_3$	n	$\mu_{\mathrm{EQ}_6}^{(n)}$	$\omega_{\mathrm{EQ}_6}^{(n)}$	$s_1s_2s_3$
1,2	0.07212161	0.04074989	S S S	1	0.1272186	0	S S S
3	0.06209526	0	S A A	2	0.08461658	0	S A A
4	0.06162059	0	A S A	3	0.08336982	0	A S A
5,6	0.02073075	0.07355143	S S S	4,5	0.06341647	0.2552465	S A A
7	0.009925378	0	S A A	6	0.04789139	0	A A S
8,9	0.009654012	0.04551274	A A S	7	0.04419344	0	A S A
10,11	0.009600794	0.2302166	S A A	8,9	0.04339547	0.2254115	S S S
12,13	1.460798e-06	1.542103e-06	- - A	10,11	0.03345811	0.03160928	S S S
14,15	-0.0001343539	0.231129	A A S	12,13	0.03334664	0.2669389	A A S
16	-0.006178861	0	A S A	14	0.02242452	0	A S A
17,18	-0.007785718	0.1372092	A A S	15	0.01870677	0	S A A
19	-0.01064716	0	S A A	16,17	0.01468624	0.02283698	A A S
20,21	-0.01220116	0.2774336	S S S	18,19	0.004690936	0.2030384	S A A
22,23	-0.01539667	0.2775381	S A A	20	4.942754e-06	0	- - A
24,25	-0.03451081	0.08674062	A S A	21	-1.080343e-06	0	- - A
26,27	-0.03719139	0.215319	S A A	22,23	-0.002003495	0.1889909	S S S

Table 5: Linear stability eigenvalues, $\lambda = \mu \pm \omega$, of EQ_7 $Re = 400$ (left), EQ_8 $Re = 270$ (right) in the Ω_{W03} cell.

n	$\mu^{(n)}_{EQ_7}$	$\omega^{(n)}_{EQ_7}$	$s_1 s_2 s_3$	n	$\mu^{(n)}_{EQ_8}$	$\omega^{(n)}_{EQ_8}$	$s_1 s_2 s_3$
1	0.07072197	0	S S S	1,2	0.08182257	0.2107588	S S S
2	0.006614697	0	A S A	3,4	0.07878857	0.2897708	S A A
3	0.003042685	0	S A A	5	0.06781999	0	A S A
4	2.566068e-07	0	- - A	6,7	0.06252085	0.1933004	A A S
5	-1.605637e-05	0	S A A	8,9	0.03904623	0.08595945	S S S
6,7	-0.004884597	0.02635118	S S S	10,11	0.02583322	0.17467	A A S
8	-0.006116859	0	A S A	12,13	0.01448147	0.07603244	S A A
9	-0.008564614	0	S A A	14	0.01213124	0	A A S
10,11	-0.009196708	0.05317915	A A S	15,16	0.008441611	0.1901902	S S S
12	-0.02359508	0	S S S	17,18	0.006553925	0.04829948	A S A
13	-0.02648861	0	S A A	19	0.001774789	0	A S A
14,15	-0.02870125	0.0292976	A A S	20,21	0.001724875	0.1530519	S S S
16,17	-0.0419181	0.05912365	S A A	22,23	-1.175502e-05	1.456183e-05	- - A
18,19	-0.04254532	0.03541646	S A A	24	-0.003114947	0	S A A
20,21	-0.05644539	0.01344645	A S A	25,26	-0.02461514	0.05357792	A S A

Table 6: Linear stability eigenvalues, $\lambda = \mu \pm \omega$, of EQ_9 for Ω_{W03} cell, $Re = 400$. It is only s_3 invariant, so only the symmetry of the eigenfunctions with respect to s_3 is reported.

n	$\mu^{(n)}_{EQ_9}$	$\omega^{(n)}_{EQ_9}$	s_3
1,2	0.02629556	0.04209157	S
3	0.02529704	0	A
4	0.0193355	0	S
5	0.01031307	0	A
6	3.343312e-06	0	A
7	-1.740506e-07	0	A
8,9	-0.005013714	0.0006279094	A
10,11	-0.02346829	0.005305554	S

Table 7: Linear stability eigenvalues $\lambda = \mu \pm \omega$ of EQ_{10} (left), EQ_{11} (right) for Ω_{W03} cell, $Re = 400$. They are both s_3 invariant only, so symmetry of the eigenfunctions with respect to s_1 and s_2 is omitted.

n	$\mu^{(n)}_{EQ_{10}}$	$\omega^{(n)}_{EQ_{10}}$	s_3	n	$\mu^{(n)}_{EQ_{11}}$	$\omega^{(n)}_{EQ_{11}}$	s_3
1,2	0.1234815	0.07686751	S	1,2	0.1408387	0.1042756	S
3,4	0.1150245	0.08568377	A	3,4	0.1344323	0.09650815	A
5	0.07437147	0	A	5,6	0.09663403	0.123391	S
6,7	0.05570779	0.08148947	S	7,8	0.03449947	0.2751065	A
8	0.01748564	0	S	9	0.0240235	0	A
9,10	0.005773602	0.06582484	S	10,11	0.01713752	0.07257651	S
11	-1.351223e-07	0	A	12,13	0.01690756	0.2455212	S
12	-6.34591e-05	0	A	14,15	6.738608e-05	0.1447936	S
13	-0.008562014	0	A	16,17	-3.44805e-06	4.910165e-06	A
14	-0.01381778	0	A	18	-0.007576297	0	A
15	-0.03149406	0	S	19,20	-0.008805768	0.008692477	S

Table 8: Linear stability eigenvalues $\lambda = \mu \pm \omega$ of TW_1 for Ω_{W03} cell, $Re = 400$. It is s_2 invariant only, so symmetry of the eigenfunctions with respect to s_1 and s_3 is omitted.

n	$\mu_{TW_1}^{(n)}$	$\omega_{TW_1}^{(n)}$	s_2
1	0.04336827	0	S
2	0.005431191	0	S
3	0.001328122	0	A
4	2.753674e-05	0	-
5	-2.083172e-05	0	-
6	-0.007500683	0	A
7,8	-0.01100895	0.006284678	S
9,10	-0.0273439	0.001997437	A

Table 9: Linear stability eigenvalues $\lambda = \mu \pm \omega$ of TW_2 (left) and TW_3 right for Ω_{W03} cell, $Re = 400$. They are s_1 invariant only, so symmetry of the eigenfunctions with respect to s_2 and s_3 is omitted.

n	$\mu_{TW_2}^{(n)}$	$\omega_{TW_2}^{(n)}$	s_1	n	$\mu_{TW_3}^{(n)}$	$\omega_{TW_3}^{(n)}$	s_1
1	0.04231491	0	S	1	0.04088411	0	A
2	0.01286686	0	S	2	0.01734567	0	S
3	0.007336427	0	A	3,4	0.01261405	0.06040676	S
4	5.837749e-07	0	-	5	0.002095999	0	A
5	-1.239071e-05	0	-	6	-4.555512e-05	0	-
6	-0.004881718	0	A	7	-8.051916e-05	0	S
7	-0.005742268	0	S	8	-0.01046996	0	S
8	-0.02115189	0	S	9,10	-0.01817192	0.3066818	S
9	-0.02283333	0	A				
10	-0.0316123	0	S				

A.2 HKW Cell Equilibria Stability

In this section the leading part of the eigenspectrum of stability matrix of the known equilibria and relative equilibria for Ω_{HKW} and $Re = 400$, is tabulated. The symmetry of the eigenfunctions is also noted. S indicates symmetry under the given the given operation, A indicates antisymmetry, and $-$ indicates asymmetry.

As discussed in chapter 3, eigenfunctions of symmetric symmetric equilibria with multiplicity 1 are always either S or A. If an equilibrium is not symmetric with respect to a given symmetry operation, then the symmetry of the eigenfunctions with respect to that operation is omitted.

Table 10: Linear stability eigenvalues $\lambda = \mu \pm \omega$, of the spanwise doubled EQ_1 (left) / EQ_2 (right) in Ω_{HKW} for $Re = 400$. They are not s_2 or s_3 symmetric, so the symmetry of the eigenfunctions is only reported with respect to s_1.

n	$\mu^{(n)}_{\mathrm{EQ}_1}$	$\omega^{(n)}_{\mathrm{EQ}_1}$	s_1	n	$\mu^{(n)}_{\mathrm{EQ}_2}$	$\omega^{(n)}_{\mathrm{EQ}_2}$	s_1
1	0.03655629	0	A	1	0.06823697	0	A
2	0.0201522	0	A	2,3	0.0631438	0.1378188	S
3	0.01656758	0	S	4	0.03213147	0	A
4,5	0.009534833	0.1274603	S	5	0.01851237	0	-
6,7	9.339563e-08	8.336229e-09	-	6	0.01851234	0	-
8,9	-0.003233331	0.005257516	-	7	1.141895e-07	0	S
10,11	-0.003233366	0.005257496	-	8	-1.347607e-08	0	-
12,13	-0.004768203	0.02450844	-	9,10	-0.004356487	0.04484489	-
14,15	-0.004768226	0.02450847	-				

Table 11: Linear stability eigenvalues $\lambda = \mu \pm \omega$, of EQ_4 in Ω_{HKW} for $Re = 400$.

n	$\mu^{(n)}_{\mathrm{EQ}_4}$	$\omega^{(n)}_{\mathrm{EQ}_4}$	$s_1 s_2 s_3$
1,2	0.2165696	0.1778438	A A S
3,4	0.2160562	0.1779641	A S A
5,6	0.1901177	0.08554518	S A A
7,8	0.1875303	0.08947402	S S S
9,10	0.1302726	0.2459975	A A S
11,12	0.1221051	0.1963254	S A A
13,14	0.1220343	0.1963399	S S S
15,16	0.1195627	0.2417901	A S A
17,18	0.09563543	0.2513773	S A A
19,20	0.08291868	0.1092781	A S A
21,22	0.05724855	0.2414199	S S S
23,24	0.05639893	0.3138937	S S S
25	0.05214196	0	S S S
26,27	0.03835707	0.170064	A A S
28,29	0.03830769	0.07027978	A A S

Table 12: Eigenvalues of the EQ_7 (left) / EQ_9 (right) in Ω_{HKW}. EQ_9 is not s_1 or s_2 symmetric, so the symmetry of its eigenfunctions is only reported with respect to s_3.

n	$\mu_{\text{EQ}_7}^{(n)}$	$\omega_{\text{EQ}_7}^{(n)}$	$s_1 s_2 s_3$	n	$\mu_{\text{EQ}_9}^{(n)}$	$\omega_{\text{EQ}_9}^{(n)}$	s_3
1	0.0650966	0	S S S	1,2	0.08425788	0.3010493	S
2	0.02592873	0	S A A	3,4	0.07335937	0.3052305	A
3	0.008950335	0	S A A	5	0.04367912	0	A
4	0.007630908	0	S S S	6	0.03971422	0	S
5,6	0.005973037	0.03101294	A A S	7	0.02158254	0	A
7,8	4.376062e-07	4.743148e-07	- - A	8,9	0.01792367	0.03164811	S
9	-0.00615165	0	A S A	10,11	0.01095836	0.3130142	A
10,11	-0.006726417	0.009772352	A S A	12	1.010861e-05	0	A
12	-0.007625031	0	S A A	13	-1.86392e-07	0	A
13	-0.009938023	0	A A S	14,15	-0.003841857	0.1197111	A
14	-0.01599924	0	A A S	16,17	-0.006086733	0.1268102	S
15	-0.01956464	0	S S S	18,19	-0.006294542	0.0009846709	A

A.3 Some Dynamic Measures of Equilibria and Relative equilibria

Table 13: Dynamic measures of known equilibria and relative equilibria for Ω_{W03}(left) and Ω_{HKW}(right), $Re = 400$, sorted by dissipation rate. $\|\cdot\|$ is the L^2-norm of the the difference from laminar, E is the energy density, $I = D$ is the dissipation rate, and $\mathbf{c}$ is wave speed. The rows labeled '$\mathbb{U}_S$' and 'full' indicate the time averages of long lived trajectories in the symmetric subspace and in the full state space respectively.

State	$\|\cdot\|$	E	$I = D$	$\mathbf{c}$		State	$\|\cdot\|$	E	$I = D$	$\mathbf{c}$
full	0.28	0.09	2.9	0		full	0.40	0.15	3.0	0
$\mathbb{U}_S$	0.28	0.09	2.9	0		$\mathbb{U}_S$	0.40	0.15	3.0	0
EQ_0	0	0.1667	1	0		EQ_0	0	0.1667	1	0
EQ_7	0.0936	0.1469	1.252	0		EQ_7	0.1261	0.1433	1.3630	0
EQ_3	0.1259	0.1382	1.318	0		$2\times EQ_1$	0.2458	0.1112	1.8122	0
EQ_9	0.1565	0.1290	1.405	0		EQ_9	0.3159	0.1175	2.0900	0
EQ_1	0.2091	0.1363	1.429	0		EQ_4	0.2853	0.0992	2.4625	0
EQ_4	0.1681	0.1243	1.454	0		$2\times EQ_2$	0.3202	0.0905	2.4842	0
EQ_5	0.2186	0.1073	2.020	0						
EQ_{10}	0.3285	0.1080	2.372	0						
EQ_2	0.3858	0.0780	3.044	0						
EQ_{11}	0.4049	0.0803	3.432	0						
TW_2	0.1776	0.1533	1.306	(0.3959,0)						
TW_1	0.2214	0.1341	1.510	(0,0.006549)						
TW_3	0.2515	0.1520	1.5343	(0.4646,0)						

APPENDIX B

HETEROCLINIC CONNECTION DATA

The data in this appendix is a listing of the statistics for the particular trajectories that have been identified as heteroclinic connections. The intention is for this data to be more important as a gauge of the accuracy of the approximate heteroclinic connections calculated, rather than as a gauge of the heteroclinic connections themselves. The logarithmic distance versus time to the source and sink equilibria is plotted in figure B. Data for the closest distance on the computed heteroclinic connections to the source and sink equilibria are in table B.

Source $\rightarrow$ Sink	Initial distance	T	Closest approach
Reynolds number - 400, Ω_{W03}			
$\mathbf{u}_{\mathrm{EQ4}} \rightarrow \mathbf{u}_{\mathrm{EQ1}}$	0.000317201	363	0.000517454
$\mathbf{u}_{\mathrm{EQ3}} \rightarrow \mathbf{u}_{\mathrm{EQ1}}$	0.0001	518	4.56902e-05
$\mathbf{u}_{\mathrm{EQ5}} \rightarrow \mathbf{u}_{\mathrm{EQ1}}$	0.00035336	240	0.00268707
Reynolds number -225, Ω_{W03}			
$\mathbf{u}_{\mathrm{EQ1}} \rightarrow \mathbf{u}_{\mathrm{EQ2}}$	0.0001	405	0.000359186

Table 14: Numerical data for the particular portions of heteroclinic connections computed, indicating the accuracy of the computations. Distances are given in terms of the L^2 norm.
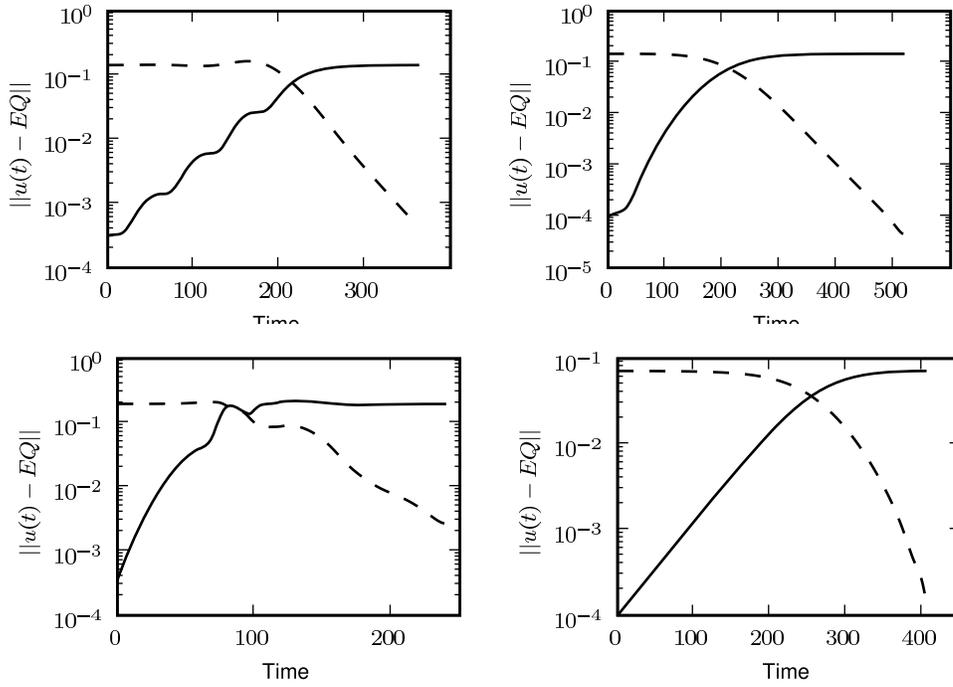
Figure 25: (Top-Left) L^2 distance to EQ_4 (solid line) and EQ_1 (dashed line) over the $Re = 400$, $\mathrm{EQ}_4 \to \mathrm{EQ}_1$ heteroclinic connection. (Top-Right) L^2 distance to EQ_3 (solid line) and EQ_1 (dashed line) over the $Re = 400$, $\mathrm{EQ}_3 \to \mathrm{EQ}_1$ heteroclinic connection. (Bottom-Left) L^2 distance to EQ_5 (solid line) and EQ_1 (dashed line) over the $Re = 400$, $\mathrm{EQ}_5 \to \mathrm{EQ}_1$ heteroclinic connection. (Bottom-Right) L^2 distance to EQ_1 (solid line) and EQ_2 (dashed line) over the $Re = 225$, $\mathrm{EQ}_1 \to \mathrm{EQ}_2$ heteroclinic connection.

APPENDIX C

SYMMETRIES AND ISOTROPIES OF SOLUTIONS

C.1 Isotropy subgroups: The 67-fold path to symmetric enlightenment

[A shorter (but more carefully proofread) version of the material covered in this appendix can be found in ref. [?].]

In long-time simulations of turbulence, symmetry considerations can be disposed off in a few lines: In absence of boundary conditions, the Navier-Stokes equations are equivariant under any $3D$ translation, $3D$ rotation, and $\mathbf{x} \to -\mathbf{x}$, $\mathbf{u} \to -\mathbf{u}$ inversion through the origin that we shall refer to as σ_{xz}. The pair of counter-moving plane Couette flow walls restricts the translation symmetry to $2D$ in-plane translations. The streamwise shearing motion restricts the $3D$ rotation symmetry to a single discrete symmetry operation, the wall interchange wall-normal-streamwise rotation by π about z-axis that we shall refer to as σ_x (symmetry referred to as "centrosymmetry" by Tuckerman and Barkley [?]). Together with inversion σ_{xz}, this symmetry generates a discrete dihedral group $D_{1,x} \times D_{1,z} = \{e, \sigma_x, \sigma_z, \sigma_{xz}\}$ of order 4,

$$
\begin{aligned}
\sigma_z \,[u,v,w](x,y,z) &= [u,v,-w](x,y,-z) \\
\sigma_x \,[u,v,w](x,y,z) &= [-u,-v,w](-x,-y,z) \\
\sigma_{xz} \,[u,v,w](x,y,z) &= [-u,-v,-w](-x,-y,-z)\,,
\end{aligned}
\tag{107}
$$

where σ_z is the spanwise reflection in z, and and $\sigma_{xz} = \sigma_x \sigma_z$. It would be more correct to refer to the subgroup of rotations generated by σ_x as $C_{2,x}$ (or $D_{1,x}$, the integers modulo 2 notation very frequently used in applied mathematics literature [?]) but we use the isomorphic group $D_{1,x}$ here to distinguish this group from the $C_{n,x}$ subgroups of $SO(2)$ in what follows. The subscripts on σ_x, σ_z, and σ_{xz} are chosen to indicate the sign changes in x, y and z under the action of each symmetry.

With periodic boundary conditions, the two translations are restricted to the compact $SO(2)_x \times SO(2)_z$ continuous two-parameter group of streamwise-spanwise translations,

$$
\tau(\ell_x, \ell_z)[u,v,w](x,y,z) = [u,v,w](x+\ell_x, y, z+\ell_z)\,.
\tag{108}
$$

$SO(2)$ is isomorphic to the *circle* group S^1, the group of rotations in plane. The equations of plane Couette flow with boundary conditions (13) are thus equivariant under the group $G_{\mathrm{PCF}} = O(2)_x \times O(2)_z = D_{1,x} \ltimes SO(2)_x \times D_{1,z} \ltimes SO(2)_z$, where subscript x indicates streamwise translations and wall-normal-streamwise inversion, z indicates spanwise translations and inversion, and $\ltimes$ stands for a semi-direct product. As far as a generic turbulent state is concerned, the symmetry discussion can stop here.

However, for compact time-invariant solutions (equilibria, relative equilibria, periodic solutions) and their instabilities the symmetries play a paramount role [?, ?], both for their classification and for understanding the dynamics connecting them, so here we shall need a much finer grained description of symmetries.

The key observation is that the G-equivariance of the equations does not imply G-invariance of their solutions. A solution of an G-equivariant equation is in general mapped

into a *group orbit* of solutions under the action of G, that is, a set of solutions that map into each other under the action of G. A solution may be invariant under an *isotropy subgroup* (or *stabilizer subgroup*) $H \subset G$; that is, $g\mathbf{u} = \mathbf{u}$ for $g \in H$. At one extreme, a generic turbulent solution has the trivial isotropy subgroup $H_{\text{turb}} = \{e\}$. The other extreme is the laminar solution whose isotropy group is the full G_{PCF}. The full classification of the lattice of intermediate isotropy subgroups is a laborious undertaking, even for a set of symmetries as plain as the ones considered here; fortunately, the set of dynamically important isotropy subgroups is relatively small. We refer the reader to the immense literature on the subject (we enjoyed reading [**?**] and [**?**] most), and give here a briefest of summaries, sufficient for the classification of the time-invariant solutions encountered so far.

Why are the equilibria for moderate Re born equipped with non-trivial isotropy groups? The physical intuition is that while the nonlinear convective terms amplify unstable fluid motions, the dissipation damps out fluid states with rapidly varying velocity fields. For moderate Re the balance of the two smooths out the long-time solutions, and equilibria with most symmetry tend to be the smoothest time-invariant solutions. A bit of history illustrates this. The laminar solution is the smoothest, least dissipative solution. Nagata discovered the EQ_1 and EQ_2 equilibria in 1990 by continuing a known solution from Taylor-Couette flow to plane Couette. Waleffe calculated the same solutions in a different way, noted that they are invariant under 'shift-rotate' and 'shift-reflect' isotropy subgroup that we refer to below as the subgroup S, and utilized this symmetry to reduce the dimensionality of his PDE discretizations. Busse and Clever [**?**] also noted this invariance. Schmiegel [**?**] undertook an investigation of several isotropy subgroups, and in what follows we shall note the subgroups that he identified. We started our exploration of plane Couette dynamics around Nagata/Waleffe equilibria, and focused our searches for new equilibria within the S-invariant subspace, since this symmetry restriction fixes the x, z phase of solutions and reduces the dimensionality of their unstable manifolds. In what follows we find primarily S-invariant equilibria because we initiated our guesses within that invariant subspace. However, as the subspace is unstable, errors accrued by long numerical simulations had sufficient deviation from the S-invariant subspace that the Newton search detected close-by equilibria whose isotropy subgroup is S_3 (discussed below). One would do well to look for solutions with other symmetries by initiating searches within other invariant subspaces.

A state with no symmetry: A turbulent state space trajectory isotropy group is $H_{\text{turb}} = \{e\}$. Such trajectory maps into a different trajectory under the action of the group, with translations generating a torus, and the inversions generating four tori of symmetry-equivalent solutions.

Relative equilibria: Let us first dispose of continuous symmetries. Equivariance of plane Couette flow equations under continuous translations allows for relative equilibria solutions, i.e., solutions that are steady in a frame moving with a constant velocity in the $[x, z]$ plane. A generic relative equilibrium solution traces out a circle or torus in state space; this set is both continuous translation and time invariant. The sign changes under reflections / rotations σ_x, σ_z imply particular centers of symmetry and thus fix the phase of a field with respect to x and z, respectively. Hence the presence of σ_x in an isotropy group rules out traveling waves in x, and likewise for z. The isotropy subgroups with relative equilibria solutions are the streamwise-spanwise traveling $SO(2)_x \times SO(2)_z$, the streamwise traveling $SO(2)_x \times D_{1,z} \ltimes C_{m,z}$, and the spanwise traveling $D_{1,x} \ltimes C_{m,x} \times SO(2)_z$ (we explain the emergence of cyclic subgroups C_m next).

Equilibria: Velocity fields invariant under the inversion σ_{xz} (i.e., under both σ_x and σ_z

flips) cannot be traveling waves, so we search for equilibria in subspaces whose isotropy group includes the inversion among its group elements.

$O(2)$ is not an abelian group, since reflections σ and translations τ along the same axis do not commute [?]: $\sigma\tau = \tau^{-1}\sigma$. Rewriting this relation as $\sigma\tau^2 = \tau^{-1}\sigma\tau$, we note that

$$
\begin{aligned}
\sigma_x\tau_x(\ell_x,0) &= \tau^{-1}(\ell_x/2,0)\,\sigma_x\,\tau(\ell_x/2,0) \\
\sigma_z\tau_z(0,\ell_z) &= \tau^{-1}(0,\ell_z/2)\,\sigma_z\,\tau(0,\ell_z/2)\,.
\end{aligned}
\tag{109}
$$

This conjugation relation implies, in terms of coordinate transformations, that a shift of ℓ_x in x followed by a flip across $x = 0$ is conjugate to a flip across $x = 0$. For $\ell_x = L_x/2$ we have $\sigma_x\tau_x = \tau_x^{-1/4}\,\sigma_x\,\tau_x^{1/4}$. Hence in classifying isotropy groups we can trade half-shift and flip $\sigma_x\tau_x$ in favor of a flip σ_x in the shifted coordinate system. However, if both σ_x and $\sigma_x\tau_x$ are elements of a subgroup, neither can be eliminated, as the conjugation simply interchanges them.

Periodic boundary conditions on equilibrium solutions identify the fields on opposing boundaries and restrict their isotropy subgroups to discrete cyclic subgroups $C_{m,x} \times C_{n,x} \subset SO(2)_x \times SO(2)_z$ along the span-, stream-wise directions [?]. For rational shifts $\ell_x/L_x = m/n$ we simplify the notation a bit by rewriting (108) as

$$
\tau_x^{\pm m/n} = \tau(\pm m L_x/n, 0)\,, \ \tau_z^{\pm m/n} = \tau(0, \pm m L_z/n)\,, \quad 0 < m < n\,,
\tag{110}
$$

and, as $m/n = 1/2$ will loom large in what follows, omit $1/2$ exponents:

$$
\tau_x = \tau_x^{1/2}\,, \ \tau_z = \tau_z^{1/2}\,, \ \tau_{xz} = \tau_x\tau_z\,.
\tag{111}
$$

If a solution is invariant under a cyclic shift

$$
\mathbf{u}(x,y,z) = \tau_x^{1/n}\mathbf{u}(x,y,z) = \mathbf{u}(x + L_x/n, y, z)\,,
\tag{112}
$$

it is the $[L_x/n, 2, L_z]$-cell solution repeated n times downstream the cell. Invariance under $\tau_x^{1/n}$ indicates that a $[L_x, 2, L_z]$ is redundant, in the sense that a cell of length L_x/n captures the same state, so it quicker and easier to compute it in the small cell. However, as we need to study bifurcations into states with wavelengths longer than the initial state, the linear stability computations need to be carried out in the full $[L_x, 2, L_z]$ cell. Suppose EQ is an equilibrium solution in the $\Omega_{1/3} = [L_x/3, 2, L_z]$ cell. Then we shall refer to the same solution repeated thrice in $\Omega = [L_x, 2, L_z]$ as $3 \times$ EQ. This solution is invariant under $C_{3,x} = \{e, \tau_x^{1/3}, \tau_x^{2/3}\}$ subgroup.

Which subgroup is realized as an equilibrium isotropy subgroup is a physical question. As the shearing is streamwise, the earliest bifurcations (as function of increasing Re) have something to do with streamwise instabilities. As the structure of Navier-Stokes solutions is a sensitive function of spanwise / streamwise / wall-normal nonlinear interactions and ratios of cell and wall-unit scales, which solutions arise first is a highly nontrivial issue [?, ?]. In addition, for small cells the existence of solutions is a sensitive function of (and an artifact of) the periodicities imposed by the cell aspect ratios $[L_x, 2, L_z]$.

A velocity field constant along the streamwise or spanwise direction is always damped by the flow to the laminar solution [?, ?, ?], so equilibrium solutions have to wiggle in both directions [?]. The more wiggles a solution has, the higher its dissipation rate. Solutions invariant under the combinations of reflections (107) and half-cell shifts (111) allow for the gentlest variation in velocity fields across the cell, so these generally have the

lowest dissipation rates, are the least unstable, and consequently are the ones to emerge first as equilibrium solutions as Re is increased. So we commence our discussion of equilibrium isotropy subgroups by $SO(2)_x \times SO(2)_z$ translations restricted to order 4 subgroup of spanwise-streamwise translations of half the cell length,

$$T = C_{2,x} \times C_{2,z} = \{e, \tau_x, \tau_z, \tau_{xz}\}. \tag{113}$$

The order-16 isotropy subgroup

$$G = D_{1,x} \times C_{2,x} \times D_{1,z} \times C_{2,z} \subset G_{\mathrm{PCF}} \tag{114}$$

of the full symmetry group contains all half-shift isotropy subgroups within it.

For spanwise full-cell $\ell_z = L_z$ and half-cell $\ell_z = L_z/2$ shifts (109) implies

$$\tau_z^{-1} \sigma_z \tau_z \ = \ \sigma_z \tag{115}$$
$$\tau_z^{-1/4} \sigma_z \tau_z^{1/4} \ = \ \sigma_z \tau_z, \tag{116}$$

and similarly for the streamwise shifts / reflections.

Let us first enumerate the subgroups $H \subset G$. From (115) we see that the half-shifts and reflections commute, so G is an *abelian* subgroup of $O(2)_x \times O(2)_z$. Subgroups can be of order $|H| = \{1, 2, 4, 8, 16\}$. A subgroup is generated by multiplication of a set of generator group elements, with the choice of generator elements unique up to a permutation of subgroup elements. A subgroup of order $|H| = 2$ has only one generator, since every group element is its own inverse. There are 15 non-identity elements to choose from, so there are 15 subgroups of order 2. Subgroups of order 4 are generated by multiplication of two group elements. There are 15 choices for the first and 14 choices for the second. Equivalent subgroup generators can be picked in $3 \cdot 2$ different ways, so there are $(15 \cdot 14)/(3 \cdot 2) = 35$ subgroups of order 4. Subgroups of order 8 have three generators. There are 15 choices for the first, 14 for the second, and 12 for the third (If the element were the product of the first two, we would get a subgroup of order 4). There are $7 \cdot 6 \cdot 4$ ways of picking equivalent generators, i.e., there are $(15 \cdot 14 \cdot 12)/(7 \cdot 6 \cdot 4) = 15$ subgroups of order 8. In summary: there is the group itself, of order 16, 15 subgroups of order 8, 35 of order 4, 15 of order 2, and 1 (the identity) of order 1, or 67 subgroups in all. This is whole lot of subgroups to juggle; fortunately, the following observations reduce this number to 5 *isotropy* subgroups that suffice –up to conjugacies– to describe all equilibria studied here.

(a) The isotropy subgroups for which we seek equilibrium solutions include σ_{xz} within its elements.

(b) The right hand side of (116) is a product of two group elements, but the left hand side is a similarity transformation that moves the coordinate frame origin by a quarter-shift. Hence we can always trade in a single spanwise (or streamwise) shift-reflect combination $\sigma\tau$ in favor of a reflect operation σ. (If both σ_j and $\sigma_j\tau_j$ are elements of a subgroup, neither can be eliminated, as the similarity transformation simply interchanges them.)

(c) By (112) any state whose isotropy subgroup includes a factor $\{e, \tau_i\}$ is a doubled state.

In what follows we label subgroups H, S, T, S_3, ..., in a somewhat arbitrary fashion, for lack of a systematic labeling scheme more compact than listing the group elements.

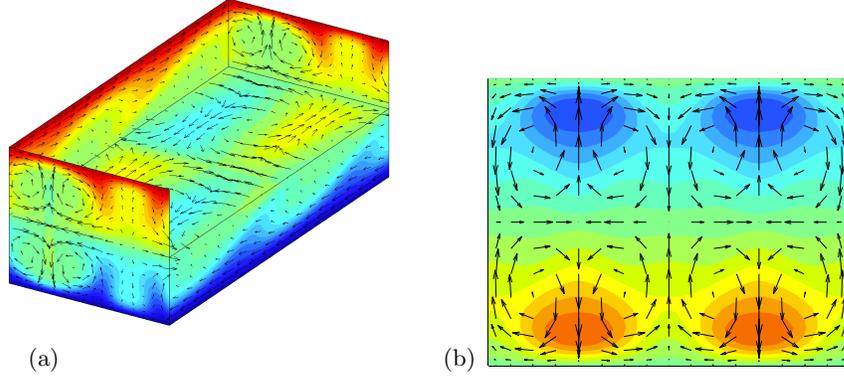(a)   (b)

Figure 26: (a) The isotropy group of equilibrium EQ$_8$ is A_{xz} given in (121). According to (112), factor $\{e, \tau_{xz}\}$ means that the state tiles the $[L_x, L_z]$ cell twice. How so? Transport the spanwise / wall-normal section distance $L_x/2$ along the x direction, and then shift it spanwise by $L_z/2$ along the z direction. The equilibrium solution in this half-cell, invariant under the R isotropy subgroup (124) tiles the cell twice. (b) x-average of EQ$_8$ velocity field $\hat{\mathbf{u}}(y, z)$ is $C_{2,z} = \{e, \tau_z\}$ (spanwise half-cell shift) invariant. The R invariance (isotropy subgroup (124)) under discrete reflections is immediate. Ω_{W03} cell, $Re = 270$.

The conjugation of $\sigma_x \tau_x$ to σ_x (and similarly for z) allows the 15 order-2 groups to be reduced to the 8 order-2 groups $\{e, g\}$ where g is one of σ_x, σ_z, σ_{xz}, $\sigma_x \tau_z$, $\sigma_z \tau_x$, τ_x, τ_z, and τ_{xz}. Of these, the latter three imply periodicity on smaller domains. Of the remaining five, σ_x and $\sigma_x \tau_z$ support traveling waves in z, σ_z and $\sigma_z \tau_x$ support traveling waves in x. Only a single subgroup of order $|H| = 2$, generated by σ_{xz}, supports equilibria:

$$S_3 = \{e, \sigma_{xz}\}. \tag{117}$$

EQ$_{11}$ is an example of an equilibrium with S_3 isotropy subgroup.

Four distinct isotropy subgroups of order 4 are generated by picking σ_{xz} as the first generator, and $\sigma_z, \sigma_z \tau_x, \sigma_z \tau_z$ or $\sigma_z \tau_{xz}$ as the second generator (R for reflect-rotate):

$$
\begin{aligned}
R &= \{e, \sigma_x, \sigma_z, \sigma_{xz}\} = S_3 \times \{e, \sigma_z\} \\
R_x &= \{e, \sigma_x \tau_x, \sigma_z \tau_x, \sigma_{xz}\} = S_3 \times \{e, \sigma_z \tau_x\} \\
R_z &= \{e, \sigma_x \tau_z, \sigma_z \tau_z, \sigma_{xz}\} = S_3 \times \{e, \sigma_z \tau_z\} = I \\
R_{xz} &= \{e, \sigma_x \tau_{xz}, \sigma_z \tau_{xz}, \sigma_{xz}\} = S_3 \times \{e, \sigma_z \tau_{xz}\} = S.
\end{aligned}
\tag{118}
$$

Each of these isotropy subgroups of G_{PCF} has three other isotropy subgroups conjugate to it under quarter-cell shifts (116). For example, the three groups $\{e, \sigma_x \tau_x, \sigma_z, \sigma_{xz} \tau_x\}$, $\{e, \sigma_x, \sigma_z \tau_z, \sigma_{xz} \tau_x\}$, and $\{e, \sigma_x \tau_x, \sigma_z \tau_z, \sigma_{xz} \tau_{xz}\}$, are conjugate to R under quarter-cell coordinate shifts in x, z, and x, z respectively. Thus the isotropy subgroups given by (118) account for 12 of the 35 order-4 subgroups of G. Note that R, R_x, R_z and R_{xz} are the only inequivalent isotropy subgroups of order 4 containing σ_{xz} and no isolated translation elements. Together with S_3 these yield the *total of 5 non-conjugate isotropy subgroups* in which we can expect to find equilibria.

The order-8 subgroups of G are generated as in our combinatorial count above, by multiplying out all distinct products of three Z_2 subgroups, $\{e, \sigma_i \tau_j\} \times \{e, \sigma_k \tau_\ell\} \times \{e, \sigma_m \tau_n\}$,

68

$i, j, k, \ell, m, n \in \{0, x, z\}$, and $\sigma_0 = \tau_0 = e$;

$$\{e, \sigma_x, \sigma_z, \sigma_{xz}, \tau_{xz}, \sigma_x\tau_{xz}, \sigma_z\tau_{xz}, \sigma_{xz}\tau_{xz}\}$$
$$\{e, \sigma_x, \sigma_z, \tau_x, \sigma_{xz}, \sigma_x\tau_x, \sigma_z\tau_x, \sigma_{xz}\tau_x\}$$
$$\{e, \sigma_x, \sigma_z, \tau_z, \sigma_{xz}, \sigma_x\tau_z, \sigma_z\tau_z, \sigma_{xz}\tau_z\}$$
$$\{e, \sigma_x, \tau_x, \sigma_x\tau_x, \sigma_z\tau_z, \sigma_z\tau_{xz}, \sigma_{xz}\tau_z, \sigma_{xz}\tau_{xz}\}$$
$$\{e, \sigma_x, \tau_x, \tau_z, \tau_{xz}, \sigma_x\tau_x, \sigma_x\tau_z, \sigma_x\tau_{xz}\}$$
$$\{e, \sigma_x, \tau_{xz}, \sigma_z\tau_x, \sigma_z\tau_z, \sigma_x\tau_{xz}, \sigma_{xz}\tau_x, \sigma_{xz}\tau_z\}$$
$$\{e, \sigma_x, \tau_z, \sigma_x\tau_z, \sigma_z\tau_x, \sigma_z\tau_{xz}, \sigma_{xz}\tau_x, \sigma_{xz}\tau_{xz}\}$$
$$\{e, \sigma_{xz}, \tau_{xz}, \sigma_x\tau_x, \sigma_x\tau_z, \sigma_z\tau_x, \sigma_z\tau_z, \sigma_{xz}\tau_{xz}\}$$
$$\{e, \sigma_z, \tau_x, \sigma_x\tau_z, \sigma_z\tau_x, \sigma_x\tau_{xz}, \sigma_{xz}\tau_z, \sigma_{xz}\tau_{xz}\}$$
$$\{e, \sigma_z, \tau_x, \tau_z, \tau_{xz}, \sigma_z\tau_x, \sigma_z\tau_z, \sigma_z\tau_{xz}\}$$
$$\{e, \sigma_z, \tau_{xz}, \sigma_x\tau_x, \sigma_x\tau_z, \sigma_z\tau_{xz}, \sigma_{xz}\tau_x, \sigma_{xz}\tau_z\}$$
$$\{e, \sigma_z, \tau_z, \sigma_x\tau_x, \sigma_z\tau_z, \sigma_x\tau_{xz}, \sigma_{xz}\tau_x, \sigma_{xz}\tau_{xz}\}$$
$$\{e, \tau_x, \sigma_{xz}, \sigma_x\tau_z, \sigma_z\tau_z, \sigma_x\tau_{xz}, \sigma_z\tau_{xz}, \sigma_{xz}\tau_x\}$$
$$\{e, \tau_x, \tau_z, \sigma_{xz}, \tau_{xz}, \sigma_{xz}\tau_x, \sigma_{xz}\tau_z, \sigma_{xz}\tau_{xz}\}$$
$$\{e, \tau_z, \sigma_{xz}, \sigma_x\tau_x, \sigma_z\tau_x, \sigma_x\tau_{xz}, \sigma_z\tau_{xz}, \sigma_{xz}\tau_z\}$$
$$\tag{119}$$

They all involve factors of $\{e, \tau_j\}$ and are thus repeats of a smaller fundamental domain half-cells. The 15 order-8 isotropy subgroups can be reduced by coordinate transformation to the following 9 subgroups: $R \times \{e, \tau_x\}$, $R \times \{e, \tau_z\}$, $R \times \{e, \tau_{xz}\}$, $R_x \times \{e, \tau_z\}$, $R_z \times \{e, \tau_x\}$, $R_x \times \{e, \tau_{xz}\} = R_z \times \{e, \tau_{xz}\}$, $T \times \{e, \sigma_x\}$, $T \times \{e, \sigma_z\}$, and $T \times \{e, \sigma_{xz}\}$. As each of these subgroups contains pure translation elements, each can be reduced to a simpler symmetry subgroup on a smaller domain. $R \times \{e, \tau_{xz}\}$ is the isotropy subgroup of EQ$_7$ and EQ$_8$.

There are 4 subgroups of order 8 which by (112) tile the cell twice: $A_?$ is generated by elements

$$A_? = \langle \sigma_x\tau_{xz}, \sigma_z\tau_{xz}, \tau_z \rangle. \tag{120}$$

$$
\begin{aligned}
A_x &= \{e, \sigma_x, \sigma_z, \sigma_{xz}, \tau_x, \sigma_x\tau_x, \sigma_z\tau_x, \sigma_{xz}\tau_x\} = R \times \{e, \tau_x\} \\
A_z &= \{e, \sigma_x, \sigma_z, \sigma_{xz}, \tau_z, \sigma_x\tau_z, \sigma_z\tau_z, \sigma_{xz}\tau_z\} = R \times \{e, \tau_z\} \\
A_{xz} &= \{e, \sigma_x, \sigma_z, \sigma_{xz}, \tau_{xz}, \sigma_x\tau_{xz}, \sigma_z\tau_{xz}, \sigma_{xz}\tau_{xz}\} \\
&= R \times \{e, \tau_{xz}\} \\
A_? &= \{e, \sigma_x, \sigma_z, \sigma_{xz}, \tau_?, \sigma_x\tau_?, \sigma_z\tau_?, \sigma_{xz}\tau_?\}.
\end{aligned}
\tag{121}
$$

As illustrated by figure 26, A_{xz} is the isotropy subgroup of equilibria EQ$_7$ and EQ$_8$ discussed below (after a spanwise quarter-shift (116) is applied to eliminate some half-shifts). There is one subgroup which appears with 4 translational copies, generated by σ_x, σ_z and τ_{xz}. It contains copies of all R subgroups (118). There are 3 subgroups of order 8 which are invariant under the translational similarity transform. These all contain T and its products with either σ_x, σ_z, or σ_{xz}.

Finally, the laminar solution EQ$_0$ isotropy group $|H| = 16$ is the full subgroup $|G| = 16$. Its multiplicity is $m = 1$, i.e., it appears only once.

What about $G = D_{1,x} \times C_{m,x} \times D_{1,z} \times C_{n,z}$ subgroups of $O(2)_x \times O(2)_z$ for $m, n > 2$?

By (112), a solution in $[L_x, 2, L_z]$ repeated n times across the cell of size $[L_x, 2, nL_z]$ is also a solution, but with a larger isotropy group, invariant under $C_{n,z}$. Already for small aspect cells studied here we encounter solutions (such as $2 \times \mathrm{EQ}_1$) with C_4 symmetry, invariant under quarter shifts $\tau^{1/4}$. They are important, as they can bifurcate into states with wavelengths longer than the initial state.

Now that we have enumerated the five distinct isotropy subgroups, it is helpful to introduce notation for the corresponding invariant subspaces of solutions of Navier-Stokes equations (by an "invariant subspace" we mean that a state of the fluid initiated within such a subspace remains in it for all times). We denote invariant subspaces of solutions of (13) as follows. Let S denote the order-4 isotropy subgroup R_{xz} (118), and $S_3 = \{1, \sigma_{xz}\}$ the order-2 isotropy subgroup (117) inversion. Let $\mathbb{U}$ be the space of velocity fields that satisfy the boundary and zero-divergence conditions of plane Couette flow, and let $\mathbb{U}_S$ and $\mathbb{U}_{S3}$ be the S and S_3-invariant subspaces of $\mathbb{U}$ respectively: $\mathbb{U}_S = \{\mathbf{u} \in \mathbb{U} \,|\, s\mathbf{u} = \mathbf{u}, \ \forall s \in S\}$, and $\mathbb{U}_{S3} = \{\mathbf{u} \in \mathbb{U} \,|\, \sigma_{xz}\mathbf{u} = \mathbf{u}\}$. As σ_{xz} changes the sign of both x and z, $\mathbb{U}_S$ and $\mathbb{U}_{S3}$ do not admit relative equilibrium solutions.

Remark: Nomenclature. It is unfortunate that the group theory nomenclature often collides with the nonlinear dynamics and fluid dynamics terminology. Here we refer to a point in the dynamical system's $d-d$ *state space* where $\dot{a} = v(a) = 0$ as an 'equilibrium' point, and the point in a $3D$ fluid flow where the Eulerian velocity vanishes as a 'stagnation point' point. The corresponding notions for symmetries of flows under continuous Lie group transformations we usually preface by a group-theoretic qualifier, such as '$G-$.' We refer to a 'group orbit' in contradistinction to 'orbit,' the set of state space points related by time evolution, and to '$G-$fixed point space' in contradistinction to dynamically stationary 'equilibrium point.'

Example: Order 8 invariant subgroups describe doubled states. The isotropy subgroup of EQ_7 and EQ_8 is

$$\{e, s_1, \cdots, s_7\} = \{e, \ \sigma_z\tau_x, \ \sigma_x\tau_{xz}, \ \sigma_{xz}\tau_z, \ \sigma_z\tau_z, \ \sigma_{xz}\tau_x, \ \tau_{xz}, \ \sigma_x\}.$$

Using spanwise quarter-shift along z we get rid of some half-shifts

$$s_1 = \sigma_z\tau_x \to \sigma_z\tau_{xz}, \quad s_3 = \sigma_{xz}\tau_z \to \sigma_{xz}, \quad s_4 = \sigma_z\tau_z \to \sigma_z, \quad s_6 = \sigma_{xz}\tau_x \to \sigma_{xz}\tau_{xz},$$

This results in the "canonical" form of this isotropy subgroup

$$R \times \{e, \tau_{xz}\} = \{e, \ \sigma_x, \ \sigma_z, \ \sigma_{xz}, \ \tau_{xz}, \ \sigma_x\tau_{xz}, \ \sigma_z\tau_{xz}, \ \sigma_{xz}\tau_{xz}\}.$$

Example: Isotropy subgroups generated multiplicatively. The abelian structure of G lends itself to a binary labeling of its $|G| = 16$ elements:

$$g_{\epsilon_1\epsilon_2\epsilon_3\epsilon_4} = \sigma_x^{\epsilon_1}\sigma_z^{\epsilon_2}\tau_x^{\epsilon_3}\tau_z^{\epsilon_4}. \tag{122}$$

In this form the group multiplication table is simply mod 2 addition of ϵ_j; for example, $g_{1011}g_{1100} = g_{0111}$.

In the C_n-invariance case the translational label ϵ_4 in (122) is n-ary, i.e., in group multiplication it is composed by addition mod n.

Associated with action of G are projection on 16 irreducible representations, symmetric/antisymmetric under action of $g_{\epsilon_1\epsilon_2\epsilon_3\epsilon_4}$:

$$P_{\pm\pm\pm\pm} = \frac{1}{2^4}(1 \pm \sigma_x)(1 \pm \sigma_z)(1 \pm \tau_x)(1 \pm \tau_z)\,. \tag{123}$$

We shall find these projection operators handy for visualization of state space flows.

There is only one isotropy group of order 2: $S_3 = \{g_{0000}, g_{1010}\}$. Multiplication with 7 group elements of form $g_{0\epsilon_2\epsilon_3\epsilon_4}$ yields 7 isotropy subgroups of order 4

$$
\begin{aligned}
S_3 \times g_{0010} &= \{g_{0000}, g_{0010}, g_{1000}, g_{1010}\} = R \\
S_3 \times g_{0110} &= \{g_{0000}, g_{0110}, g_{1010}, g_{1100}\} = R_x \\
S_3 \times g_{0011} &= \{g_{0000}, g_{0011}, g_{1001}, g_{1010}\} = R_z \\
S_3 \times g_{0111} &= \{g_{0000}, g_{0111}, g_{1010}, g_{1101}\} = R_{xz}\,,
\end{aligned} \tag{124}
$$

and half-cell doubled states

$$
\begin{aligned}
S_3 \times g_{0100} &= \{g_{0000}, g_{0100}, g_{1010}, g_{1110}\} = D_x \\
S_3 \times g_{0001} &= \{g_{0000}, g_{0001}, g_{1010}, g_{1011}\} = D_z \\
S_3 \times g_{0101} &= \{g_{0000}, g_{0101}, g_{1010}, g_{1111}\} = D_{xz}\,.
\end{aligned} \tag{125}
$$

Group elements of form $g_{1\epsilon_2\epsilon_3\epsilon_4}$ all appear in the above subgroups and contribute no further order 4 subgroups.

Multiplication of R's with group elements not already within them generates 6 isotropy subgroups of order 8 (all names temporary, for now)

$$
\begin{aligned}
A &= \{g_{0000}, g_{0110}, g_{1010}, g_{1100}, g_{0001}, g_{0111}, g_{1011}, g_{1101}\} \\
B &= \{g_{0000}, g_{0110}, g_{1010}, g_{1100}, g_{0011}, g_{0101}, g_{1001}, g_{1111}\} \\
C &= \{g_{0000}, g_{0011}, g_{1001}, g_{1010}, g_{0100}, g_{0111}, g_{1101}, g_{1110}\}
\end{aligned} \tag{126}
$$

$$
\begin{aligned}
U_x &= \{g_{0000}, g_{0010}, g_{0100}, g_{0110}, g_{1000}, g_{1010}, g_{1100}, g_{1110}\} \\
U_z &= \{g_{0000}, g_{0010}, g_{1000}, g_{1010}, g_{0001}, g_{0011}, g_{1001}, g_{1011}\} \\
U_{xz} &= \{g_{0000}, g_{0010}, g_{1000}, g_{1010}, g_{0101}, g_{0111}, g_{1101}, g_{1111}\}
\end{aligned} \tag{127}
$$

and a multiplication table

$$
\begin{aligned}
R \times g_{0100} &= U_x\,, & R \times g_{0001} &= U_z\,, & R \times g_{0101} &= U_{xz} \\
R_x \times g_{0001} &= A\,, & R_x \times g_{0010} &= U_x\,, & R_x \times g_{0011} &= B \\
R_z \times g_{0001} &= U_z\,, & R_z \times g_{0100} &= C\,, & R_z \times g_{0101} &= B \\
R_{xz} \times g_{0001} &= A\,, & R_{xz} \times g_{0010} &= U_{xz}\,, & R_{xz} \times g_{0011} &= C
\end{aligned} \tag{128}
$$

Multiplication of D's with group elements not already within them generates further subgroups.

Example: $\{e, \sigma_{xz}\}$ invariant equilibrium: EQ_{11}

S_3 isotropy subgroup $\{1, \sigma_{xz}\}$ is order 2. The smaller group means a bigger quotiented state space. There are *eight* copies of any S_3-invariant field, generated by the four half-cell translations and by reflection about the $z = 0$ plane.

Let u be s_3-invariant: $u = s_3 u$. s_3 commutes with *all four* elements of $T = \{e, \tau_x, \tau_z, \tau_{xz}\}$. Thus $s_3(\tau u) = \tau s_3 u = \tau u$, and so τu is s_3 symmetric for all four choices of τ.

Moreover, $s_1 u$ is S_3-invariant for S_3-invariant u (and generally $s_1 u \neq \tau u$ for $\tau \in \{\tau_x, \tau_z, \tau_{xz}\}$. We have $u = s_3 u$, so $s_1 u = s_1 s_3 u = s_3(s_1 u)$. That then gives us eight copies: $s\tau u$ for $s \in \{e, s_1\}$ and $\tau \in T$. Trying to expand by s_2 multiplication doesn't produce any new fields, since $s_2 u = s_1 s_3 u = s_1 u$. So in general, each S_3-invariant field has eight copies in the s_3 invariant subspace, unless these copies coincide due to further symmetries (e.g. fields with additional s_1 symmetry total only four copies). Figure 27 shows the eight S_3-invariant copies of EQ$_{11}$.

Translations of half the cell length in the spanwise and/or streamwise directions commute with S. These operators generate T, a discrete subgroup (113) of the continuous translational symmetry group $SO(2) \times SO(2)$: Take EQ$_2$ as an example of an S_3-invariant field. It has four distinct copies within $\mathbb{U}_S$, and $\mathbb{U}_S$ is a subset of the S_3-invariant subspace. So we have an example of an S_3-invariant field with at least four copies in the S_3-invariant subspace.

EQ$_7$ and EQ$_8$ have multiplicity 2, as their isotropy subgroup is (121).

C.2 Action of the s_1, s_2 elements on the Gibson basis

The basis elements of Gibson basis which are in the s_1 and s_2 subspaces are given by:

$$\alpha j \Phi^u_{\sigma jkl}(y) + \Phi^{v'}_{\sigma jkl}(y) + \gamma k \Phi^w_{\sigma jkl}(y) = 0, \tag{129}$$

where

$$g_j(x) = \begin{cases} \sin jx & j < 0 \\ 1 & j = 0 \\ \cos jx & j > 0 \end{cases} \tag{130}$$

and where $\Phi^{u,v,w}_{\sigma jkl}(y)$ is given by $R_l(y)$ or a multiple of $Q_l(y)$ defined as

$$R_l(y) = \begin{cases} \frac{1+y}{2} & l = 0 \\ \frac{1-y}{2} & l = 1 \\ \frac{1}{\sqrt{2(2l+1)}}(P_{l-2}(y) - P_l(y)) & l \geq 2 \end{cases}, \tag{131}$$

$$Q_l(y) = \int_{-1}^{y} R_l(y')dy'.$$

To start consider the effect of s_1 and s_2 on $g_j(\alpha x)$ and $g_k(\gamma z)$. Substituting $z = -z$ or $x = -x$ gives:

$$g_j(-x) = \begin{cases} -g_j(x) & j < 0 \\ g_j(x) & j \geq 0 \end{cases} \tag{132}$$

Translation by a half period is given by

$$g_j(x + \pi) = \begin{cases} g_j(x) & j = 0 \\ -g_j(x) & \text{otherwise} \end{cases} \tag{133}$$
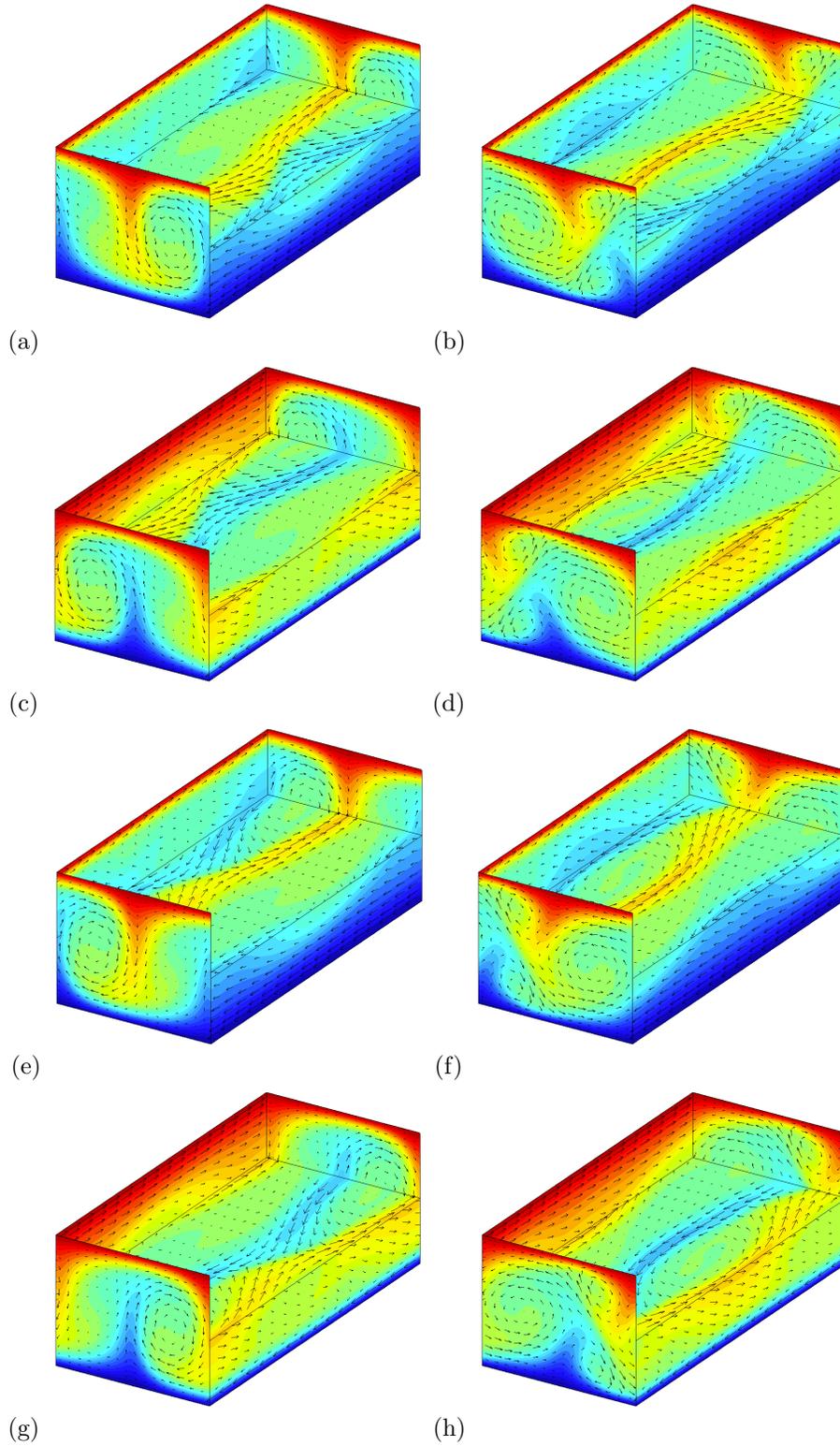
Figure 27: The eight copies of EQ_{11} within the S_3-invariant subspace: (a) $\mathbf{u}_{EQ11}$ (b) $\tau_x\mathbf{u}_{EQ11}$ (c) $\tau_z\mathbf{u}_{EQ11}$ (d) $\tau_{xz}\mathbf{u}_{EQ11}$ (e) $\sigma_z\mathbf{u}_{EQ11}$ (f) $\tau_x\sigma_z\mathbf{u}_{EQ11}$ (g) $\sigma_z\tau_z\mathbf{u}_{EQ11}$ and (h) $\sigma_z\tau_{xz}\mathbf{u}_{EQ11}$. The S_3 invariance of each solution has been verified numerically. Ω_{W03} cell, $Re = 400$.

73

Then for the y-dependent parts of the basis:

$$R_l(-y) \quad = \begin{cases} R_1(y) & l = 0 \\ R_0(y) & l = 1 \\ R_l(y) & l > 1 \quad \text{and l is even} \\ -R_l(y) & l > 1 \quad \text{and l is odd} \end{cases} \tag{134}$$

$$Q_l(-y) \quad = \begin{cases} Q_0(1) - Q_1(y) & l = 0 \\ Q_1(1) - Q_0(y) & l = 1 \\ Q_2(1) - Q_2(y) & l = 2 \\ Q_l(y) & l \geq 3 \quad \text{and l is odd} \\ -Q_l(y) & l \geq 3 \quad \text{and l is even} \end{cases}, \tag{135}$$

With the action of the symmetries given as

$$s_1 \begin{pmatrix} u \\ v \\ w \end{pmatrix}(x,y,z) \quad = \quad \begin{pmatrix} u \\ v \\ -w \end{pmatrix}(x + L_x/2, y, -z) \tag{136}$$

$$s_2 \begin{pmatrix} u \\ v \\ w \end{pmatrix}(x,y,z) \quad = \quad \begin{pmatrix} -u \\ -v \\ w \end{pmatrix}(-x + L_x/2, -y, z + L_z/2) \tag{137}$$

$$s_3 \begin{pmatrix} u \\ v \\ w \end{pmatrix}(x,y,z) \quad = \quad \begin{pmatrix} -u \\ -v \\ -w \end{pmatrix}(-x, -y, -z + L_z/2), \tag{138}$$

each element of the basis set is either symmetric or antisymmetric with respect to each symmetry, see table 15.

C.2.1 Structure of the ODE representation

Note the following identity for Legendre polynomials:

$$\int P_l(y) = \frac{P_{l+1}(y) - P_{l-1}(y)}{2l + 1} \tag{139}$$

This means we can alternatively define $Q_l(y)$ as:

$$Q_l(y) = \int_{-1}^{y} R_l(y') \quad = \quad \int_{-1}^{y} P_{l-2}(y') - P_l(y') \tag{140}$$

$$= \quad \frac{P_{l-1}(y) - P_{l-3}(y)}{2l - 3} - \frac{P_{l+1}(y) - P_{l-1}(y)}{2l + 1} \tag{141}$$

$$= \quad \frac{R_{l+1}(y)}{2l + 1} - \frac{R_{l-1}(y)}{2l - 3} \tag{142}$$

Since $(P_m, P_n) = \delta_{mn}/(2n+1)$, $(R_m, R_n) = \delta_{mn}(1/(2m+1) + 1/(2m-3)) + \delta_{m,n+2}/(2m+1) + \delta_{m,n-2}/(2m+1)$.

σ	j	k	l	$\Phi^u_{\sigma jkl}(y)$	$\Phi^v_{\sigma jkl}(y)$	$\Phi^w_{\sigma jkl}(y)$	s_1	s_2	s_3
0	0	0	$\{2,\ldots,L\}$e	$R_l(y)$	0	0	S	A	A
0	0	0	$\{2,\ldots,L\}$o	$R_l(y)$	0	0	S	S	S
1	0	0	$\{2,\ldots,L\}$e	0	0	$R_l(y)$	A	S	A
1	0	0	$\{2,\ldots,L\}$o	0	0	$R_l(y)$	A	A	S
0	j	0	$\{3,\ldots,L{-}1\}$e	$R_l(y)$	$-\alpha jQ_l(y)$	0	A	S	A
0	j	0	$\{3,\ldots,L{-}1\}$o	$R_l(y)$	$-\alpha jQ_l(y)$	0	A	A	S
0	$-j$	0	$\{3,\ldots,L{-}1\}$e	$R_l(y)$	$-\alpha jQ_l(y)$	0	A	A	S
0	$-j$	0	$\{3,\ldots,L{-}1\}$o	$R_l(y)$	$-\alpha jQ_l(y)$	0	A	S	A
1	j	0	$\{2,\ldots,L\}$e	0	0	$R_l(y)$	S	S	S
1	j	0	$\{2,\ldots,L\}$o	0	0	$R_l(y)$	S	A	A
1	$-j$	0	$\{2,\ldots,L\}$e	0	0	$R_l(y)$	S	A	A
1	$-j$	0	$\{2,\ldots,L\}$o	0	0	$R_l(y)$	S	S	S
0	0	k	$\{2,\ldots,L\}$e	$R_l(y)$	0	0	A	A	S
0	0	k	$\{2,\ldots,L\}$o	$R_l(y)$	0	0	A	S	A
0	0	$-k$	$\{2,\ldots,L\}$e	$R_l(y)$	0	0	S	A	A
0	0	$-k$	$\{2,\ldots,L\}$o	$R_l(y)$	0	0	S	S	S
1	0	k	$\{3,\ldots,L{-}1\}$e	0	$-\gamma kQ_l(y)$	$R_l(y)$	A	A	S
1	0	k	$\{3,\ldots,L{-}1\}$o	0	$-\gamma kQ_l(y)$	$R_l(y)$	A	S	A
1	0	$-k$	$\{3,\ldots,L{-}1\}$e	0	$-\gamma kQ_l(y)$	$R_l(y)$	S	A	A
1	0	$-k$	$\{3,\ldots,L{-}1\}$o	0	$-\gamma kQ_l(y)$	$R_l(y)$	S	S	S
0	j	k	$\{2,\ldots,L\}$e	$\gamma kR_l(y)$	0	$-\alpha jR_l(y)$	S	A	A
0	j	k	$\{2,\ldots,L\}$o	$\gamma kR_l(y)$	0	$-\alpha jR_l(y)$	S	S	S
0	j	$-k$	$\{2,\ldots,L\}$e	$\gamma kR_l(y)$	0	$-\alpha jR_l(y)$	A	A	S
0	j	$-k$	$\{2,\ldots,L\}$o	$\gamma kR_l(y)$	0	$-\alpha jR_l(y)$	A	S	A
0	$-j$	k	$\{2,\ldots,L\}$e	$\gamma kR_l(y)$	0	$-\alpha jR_l(y)$	S	S	S
0	$-j$	k	$\{2,\ldots,L\}$o	$\gamma kR_l(y)$	0	$-\alpha jR_l(y)$	S	A	A
0	$-j$	$-k$	$\{2,\ldots,L\}$e	$\gamma kR_l(y)$	0	$-\alpha jR_l(y)$	A	S	A
0	$-j$	$-k$	$\{2,\ldots,L\}$o	$\gamma kR_l(y)$	0	$-\alpha jR_l(y)$	A	A	S
1	j	k	$\{3,\ldots,L{-}1\}$e	$\gamma kR_l(y)$	$-\alpha\gamma jkQ_l(y)$	$\alpha jR_l(y)$	S	A	A
1	j	k	$\{3,\ldots,L{-}1\}$o	$\gamma kR_l(y)$	$-\alpha\gamma jkQ_l(y)$	$\alpha jR_l(y)$	S	S	S
1	j	$-k$	$\{3,\ldots,L{-}1\}$e	$\gamma kR_l(y)$	$-\alpha\gamma jkQ_l(y)$	$\alpha jR_l(y)$	A	A	S
1	j	$-k$	$\{3,\ldots,L{-}1\}$o	$\gamma kR_l(y)$	$-\alpha\gamma jkQ_l(y)$	$\alpha jR_l(y)$	A	S	A
1	$-j$	k	$\{3,\ldots,L{-}1\}$e	$\gamma kR_l(y)$	$-\alpha\gamma jkQ_l(y)$	$\alpha jR_l(y)$	S	S	S
1	$-j$	k	$\{3,\ldots,L{-}1\}$o	$\gamma kR_l(y)$	$-\alpha\gamma jkQ_l(y)$	$\alpha jR_l(y)$	S	A	A
1	$-j$	$-k$	$\{3,\ldots,L{-}1\}$e	$\gamma kR_l(y)$	$-\alpha\gamma jkQ_l(y)$	$\alpha jR_l(y)$	A	S	A
1	$-j$	$-k$	$\{3,\ldots,L{-}1\}$o	$\gamma kR_l(y)$	$-\alpha\gamma jkQ_l(y)$	$\alpha jR_l(y)$	A	A	S

Table 15: The polynomial triplets for a complete set of linearly independent basis functions $\mathbf{\Phi}_{\sigma jkl}$ up to a given Fourier discretization $|j| \leq J$, $|k| \leq K$ and polynomial degree $l \leq L$. 'A' indicates that a member of the basis is anti-symmetric with respect to the symmetry operator s_i and 'S' indicates symmetric. Indices are j and k are strictly positive unless explicitly stated otherwise. e and o indicate the even and odd members of a set, respectively. Note we could drop one of the columns since $s_1 s_2 = s_3$, so if one is S the other two are either S,S or A,A and if one is A then the others are S, A or A,S.

VITA

Jonathan Halcrow was born in 1981 in Port Jefferson, NY, and started roaming the countryside between New York and Virginia for 14 years. Eventually he settled in Georgia and attended North Gwinnett High School. After graduation in 1999, it was off to Georgia Tech to get a B.S. in Math and another in Physics in 2003. Realizing that there's no place like home, he stayed there for graduate school.

In 2008 he got a haircut, cleaned his desk and the access corridor to it, started eating fruits and vegetables, started bicycling to 'work,' stopped smoking, lost weight, all in preparation to accession to yuppiedom and long AARP years that are to follow. At some point in all this he managed to find the time to write a thesis.